IOWA STATE UNIVERSITY
Digital Repository

Graduate Theses and Dissertations

Iowa State University Capstones, Theses and Dissertations

2018

Biodetection and biointerface based on Nanostructured Aluminum Oxide (NAO): From fluorescence enhancement to MS effect on single neural cells

Xiangchen Che
Iowa State University

Follow this and additional works at: https://lib.dr.iastate.edu/etd

 Part of the Electrical and Electronics Commons, and the Optics Commons

Recommended Citation
Che, Xiangchen, "Biodetection and biointerface based on Nanostructured Aluminum Oxide (NAO): From fluorescence enhancement to MS effect on single neural cells" (2018). *Graduate Theses and Dissertations*. 16767.
https://lib.dr.iastate.edu/etd/16767

This Dissertation is brought to you for free and open access by the Iowa State University Capstones, Theses and Dissertations at Iowa State University Digital Repository. It has been accepted for inclusion in Graduate Theses and Dissertations by an authorized administrator of Iowa State University Digital Repository. For more information, please contact digirep@iastate.edu.

www.manaraa.com

Biodetection and biointerface based on Nanostructured Aluminum Oxide (NAO): From fluorescence enhancement to MS effect on single neural cells

by

Xiangchen Che

A dissertation submitted to the graduate faculty

in partial fulfillment of the requirements for the degree of

DOCTOR OF PHILOSOPHY

Major: Electrical and Computer Engineering

Program of Study Committee:
Long Que, Major Professor
Jiming Song
Jaeyoun Kim
Pandey Santosh
Ian C Schneider

The student author, whose presentation of the scholarship herein was approved by the program of study committee, is solely responsible for the content of this dissertation. The Graduate College will ensure this dissertation is globally accessible and will not permit alterations after a degree is conferred.

Iowa State University

Ames, Iowa

2018

Copyright © Xiangchen Che, 2018. All rights reserved.

www.manaraa.com

TABLE OF CONTENTS

Page

www.manaraa.com

www.manaraa.com

LIST OF FIGURES

www.manaraa.com

www.manaraa.com

www.manaraa.com

www.manaraa.com

LIST OF TABLES

Page

www.manaraa.com

NOMENCLATURE

AAO	Anodic Aluminum Oxide
PDMS	Polydimethylsiloxane
FEA	Finite Element Analysis
DI	Deionized
SEM	Scanning Electron Microscopy
AFM	Atomic Force Microscopy
FSS	Fluorescein Sodium Salt
PI	Propidium Iodide
FBA	Fluorescent Brightening Agents
MS	Transcranial Magnetic Stimulation
NPs	Nano-Particles
LOD	Limit of Detection

www.manaraa.com

ACKNOWLEDGMENTS

This dissertation summarizes the research work during my Ph.D program at Iowa State University. I would like to thank all the people who guided and supported me during this period.

Foremost, I want to express my sincere gratitude to my advisor, Dr. Long Que, for his generous and continuous support in my Ph.D. study and research, for his patience, motivation, enthusiasm, and immense knowledge. It is my great honor to be his doctoral student. This dissertation could not have been completed without his encouragement and constant guidance.

Second, I would like to thank my advisory committee: Dr. Jiming Song, Dr. Jaeyoun Kim, Dr. Pandey Santosh, and Dr. Ian C Schneider, for their guidance and support throughout this research.

In addition, I would also like to thank my fellow labmates: Jacob Nuhn, Juan Wang, Unnikandam-Veettil Shalin, Joseph Boldrey, Xiaojing Zhong, Pan Deng, Shenming Gong, Chao Song, Silu Feng, Yuan He, Xiang Li, and Haochen Yin for their valuable research experience and great support.

I also would like to thank MRC staff Dr.Wai Y.Leung, Noack Max for the technical and experimental support.

Finally, I would like to thank my family: my father, Chuanzhi Che, my mother, Kunli Pu, my girlfriend, Mo Chen for their love, understanding and endless encouragement throughout my life.

Acknowledgments

www.manaraa.com

ABSTRACT

Anodic aluminum oxide (AAO) has been investigated and utilized in numerous products for almost a century. But the rapidly increasing interest in nanoscale materials and their outstanding properties has propelled nanoporous AAO to be used as a substrate for sensors and biosensors. Fluorescence-based biosensors are one type of optical biosensors which are very popular for detecting a variety of targets (DNA, RNA, glucose, enzyme, bacteria, etc.). The recent discovery of AAO fluorescence enhancement effect makes AAO more attractive since it has the great potential to be used in biosensing field to improve the sensor sensitivity. However, the mechanism of the AAO fluorescence enhancement effect has not be understood thoroughly. Based on the experimental and modeling results, it has been found that the main contributing factor to the fluorescence enhancement is probably the plasmonic Al nanoparticles (NPs) embedded in the film, while the nanopore dimensions have a limited contribution. Based on its fluorescence enhancement effect, a new class of molecular beacon biosensors is developed to detect specific hairpin DNA sequence. The sensor demonstrates excellent specificity and selectivity, indicating the great promise of this type of sensor for diagnostic applications. Furthermore, another optical biosensor has been developed based on AAO. TGF-β1 which is one type of growth factor secreted by pancreatic stellate cell (ITAF) has successfully detected by this sensor. It has been found that 10 ng/ml of purified transforming growth factor β1 (TGF-β1) can be readily detected in buffer with high specificity. TGF-β1 in a conditioned cell medium has also been detected successfully. By comparing with the reference data of purified TGF-β1, concentration of TGF-β1 secreted in the conditioned cell medium has been reasonable estimated. Finally, Transcranial magnetic stimulation

www.manaraa.com

(MS) effects on single neuron cell (N27) have been studied on both glass and AAO substrate. It has been found that MS not only has a negligible cytotoxic effect on N27 cells but also can speed up the N27 cell proliferation and regeneration.

www.manaraa.com

CHAPTER 1. INTRODUCTION OF ANODIC ALUMINUM OXIDE

1.1 Overview of Anodic Aluminum Oxide

Anodic Aluminum Oxide which is short for AAO is a self-organized material. High density of arrayed nanopores form its honeycomb structure. The parallel nanopore dimension such as, inner and outer nanopore diameter, nanopore length, thickness of the barrier layer, etc. can be controlled by adjusting the parameters during the electrochemical anodization process.

The porous nature of anodic alumina films was discovered by S. Setch, A. Miyatain in 1932 [1]. It was further characterized by F. Keller's group in 1953 [2] and J. P. O'Sullivan's group in 1970 [3]. Porous AAO is formed in acid electrolytes, oxide aluminum growth and localized dissolution are balanced in order to form arrayed nanopores. Various acids can be used in the anodization process, such as chromic acid, oxalic acid, phosphoric acid and sulfuric acid, etc. Detailed information was elaborated in a patent by Alan W. Smith of Boeing Company in 1974 [4]. Due to the self-ordered nanoporous structure, AAO gained attention in the nanotechnology field. Especially, it was used as a template to deposit uniform arrayed nanowires [5,6,7]. In 1990s, AAO became more popular since several research efforts had been made which focused on using AAO for bottom-up templated nanofabrication [8,9,10,11].

Nanomaterials which based on AAO have a wide range of applications, such as drug delivery, implants, biosensing, energy storage, photonics, etc. The reason of AAO fast emerged in nanotechnology is because its structure and chemistry can be controlled at nanoscale level over very large areas. This advantage enables development of new materials and products with desired structures and dimensions which are suitable for more specific researches.

www.manaraa.com

1.2 History of AAO development

Aluminum is the third abundant element in nature, and it is the most abundant metal in the Earth's crust (~8 %). Generally, aluminum reacts with oxide rapidly in ambient atmospheres and an oxide layer with a thickness of 2-3 nm formed on its surface. Further oxidation cannot be formed due to this native oxide layer which makes this type of aluminum a good corrosion resistance. However, local corrosion can happen in some aggressive environments which contain corrosive chemicals.

Electrochemically oxidized aluminum was first found by Buff in 1857, an aqueous solution was used to oxidize aluminum and a thicker oxide layer was formed compare to native oxide in nature [12]. It was called "anodization" since aluminum also served as the anode during the reaction in the aqueous solution. Normally, there are two types of anodic aluminum oxide (AAO), nonporous barrier-type oxide AAO and porous-type oxide AAO. The types of AAO films mainly depended on the electrolyte used in the anodization process [13]. As anodization of aluminum was first developed to protect corrosion on metals, aluminum and aluminum alloys attracted strong attention for its extensive practical applications in industry.

In the early 1920s, "anodized oxide" was utilized to protect seaplane parts from corrosion in seawater [14]. In addition, anodized aluminum oxide has many outstanding properties such as corrosion resistance, strong hardness, abrasion resistance, etc [15]. Moreover, porous oxide films can serve as good adhesion base or interface for electroplating and painting due to its porosity structure. All these good properties made anodized aluminum popular in industrial products, such as electronic gadgets, electrolytic capacitors, plasma equipment, architectural materials, machine parts, vehicles, aircrafts, aerospace, etc.

Recently, this last century developed scientific and technical product has attracted great noticeable interests in the nanotechnology field. It began with the discovery works of self-ordered

www.manaraa.com

porous AAO reported by Masuda in 1995 [16]. Follow-up works about the development of two-step anodization process was also reported by Masuda's group in 1996 [17]. Start from that, the novel nanoporous AAO has been intensively utilized for synthesizing various types of nanostructured materials, such as nanorods, nanowires, nanotubes, and some functional nanodevices. After 2000s, AAO had drawn more researchers' attention to biofield such as biosensing, bio-detection, drug delivery, biocompatibility for cell growth, etc [18-24]. More applications in the biological field will be discussed in section 1.5.

1.3 AAO fabrication based on electrochemistry

AAO structure is similar as a honeycomb structure which is a close-packed hexagonal array of parallel cylindrical nanopores as shown in **Figure 1.1**. The important parameters of AAO are pore density, pore diameter, interpore distance, pore depth (thickness) and barrier layer thickness. All those parameters can be controlled by adjusting the anodization conditions. For instance, AAO pore diameter can be tuned from 10 to 400 nm; interpore distance can be tuned from 50 to 600 nm; pore aspect ratio from 10 to 5000; AAO porous layer thickness from 10 nm to 150 um, etc. [25,26,27].

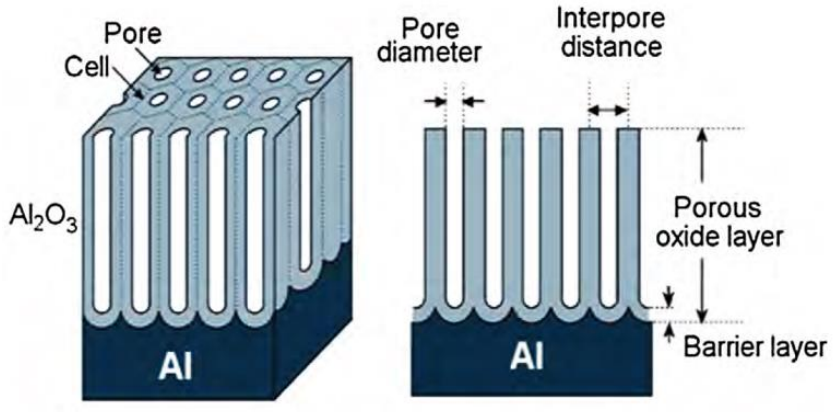

Figure 1.1 *Schematic drawing of AAO structure prepared by electrochemical anodization of Al* [28].

www.manaraa.com

The fabrication of nanopore structure AAO can be done by using general laboratory equipment as shown in **Figure 1.2**. First, a reaction tank with 'dual walls' is prepared as the container for the whole anodization process. A cooling system is connected which is powered by an RF machine. Cooling water with a temperature of 2°C to 8°C is flowing in an inner loop to maintain the reaction temperature inside the tank. Next, the acid solution is poured into the tank working as the electrolyte. The commonly used acids are chromic acid, oxalic acid, phosphoric acid, sulfuric acid, etc. Then, two working electrodes are prepared: aluminum (Al) as the anode and platinum as the cathode. A rectifier is used to apply DC voltage across two electrodes, and Al is going to be gradually anodized to form a nanoporous structure. That is the reason anodic aluminum oxide (AAO) is named. During the anodization process, a stirring bar and magnetic stirrer are used to ensure the uniformity of the acid concentration to make a smooth and stable anodization process.

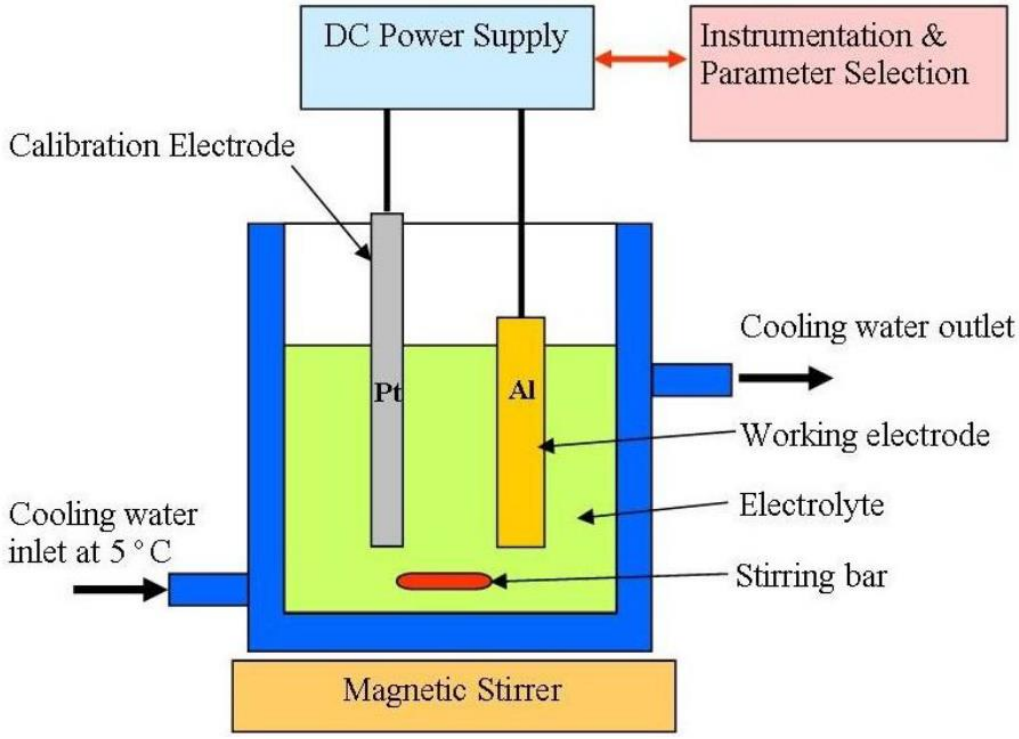

Figure 1.2 *Experimental equipment used to produce anodized aluminum oxide [29].*

www.manaraa.com

As discussed above, the equation to get nanopore structure is a simple one: Al + acid + voltage = nanopores. However, there are several parameters need to be controlled in order to achieve a good quality of highly self-ordered nanopore structure. For instance, the quality of Al substrate, surface structure, and surface pre-treatments play an important role on the final nanostructures. A pre-oxide layer always exists on the Al film surface as Al can be easily oxidized in an ambient oxygen atmosphere. Additionally, any mechanical, thermal, chemical process could introduce different surface structure on Al film. All these things can significantly affect the quality of nanopore formation during the anodization process. The is due to the effects of surface defects, such as surface scratches, pits, impurities and grain boundaries which have a great impact on the local electrochemical reaction mechanism. Moreover, the exist of other elements in Al film will significantly reduce the nanopore formation rate and damage the final pore structure [30]. Therefore, a high purity of 99.99% or even 99.999% Al is commonly used as the substrate for anodization. Typically, Al film is degreased by soaking it into acetone or similar solvent followed by an electrochemical polishing (3M NaOH) for five minutes and then DI washer rinse for the final step. Next, an annealing process is conducted for reducing mechanical stresses in Al film. During the annealing process, Al grain size increases and Al film becomes rougher, grain boundaries become larger. The optimized properties to improve the nanopore formation in the anodization process.

Different types of acids can be used as electrolyte to fabricate nanopore structure AAO. The choice of acids normally depends on the specific applications. The commonly used acids are listed in **Table 1.1** [28]. The achieved nanopore structure highly depends on the acid used. For example, pore size can be controlled from 20 nm to 80 nm by using oxalic acid. It can also reach up to ~200 nm by using phosphoric acid.

www.manaraa.com

Table 1.1 *Commonly used acids as an electrolyte in the fabrication of nanoporous aluminum oxide layer on the aluminum substrate [28].*

Main Acid used in Electrolyte	Molecular Formula	Concentration (M)	Pore Size Range (nm)
Acetic	CH_3CO_2H	1	Not specified
Citric	$HO_2CCH_2(OH)(CO_2H)CH_2CO_2H$	0.1 to 2	90 to 250
Chromic	H_2CrO_4	0.3, 0.44	17 to 100
Glycolic	$CH_2(OH)CO_2H$	1.3	35
Malic	$HO_2CH_2CH(OH)CO_2H$	0.15 to 0.3	Not specified
Malonic	$CH_2(CO_2H)_2$	0.1 to 5	Not specified
Oxalic	$C_2H_2O_4$	0.2 to 0.5	20 to 80
Phosphoric	H_3PO_4	0.04 to 1.1	30 to 235
Sulfuric	H_2SO_4	0.18 to 2.5	12 to 100
Tartaric	$HO_2CCH(OH)CH(OH)CO_2H$	0.1 to 3	Not specified

As mentioned before, the dimension of nanoporous AAO can be tuned by adjusting the types of acid used, the voltage applied and anodization time. There most common acid and their parameters are listed below in **Table 1.2** [28]**.** For example, 80 nm pore size can be made by using oxalic acid with a concentration of 0.3 M under 40 V voltage for 8 hours. A pore size of 20 nm can be achieved by using the same concentration of 0.3 M sulfuric acid under 25 V voltage for 12 hours.

1.4 Self-ordered nanoporous structure formation mechanism

Although thick nanoporous AAO film has been extensively used in industry to develop many practical products start from the last century, it was not well understood for the mechanism behind the formation of those highly self-ordered nanostructure. As mentioned before, Keller and his group members conducted the first detailed research study on the actual mechanism underlying anodization for porous oxide layer formation [2]. During the anodization process, there are two types of oxide will be formed: barrier oxide layer and the nanoporous oxide layer. Both of the two

www.manaraa.com

layers formations are highly related to the electrolyte's PH value, chemical compositions, and operating conditions. Each stage of oxide will be discussed in the following content.

Table 1.2 *Voltage, time and acid concentration controlled AAO nanopore size of three commonly used electrolytes [28].*

Acid	Concentration. (M)	Voltage (volts)	Pore Size (nm)	Time (hours)
Oxalic	0.25	60	75	8,8
	0.3	40	Not specified	variable
	0.3	40	80	8, variable
	0.3	40	50	10,5 min
	0.3	60	80	3,8
	0.3	40	40–50	40 min, 2
	0.3	40, 50	20,35	variable
	0.3	30	40	8,10
	0.4	40	50	8,10
	0.5	50	80	8,10
	0.3	40	22	12,4,8,12& 16
Phosphoric	Not specified	195	200	variable
	0.4	5 to 40	20 to 75	1 step/variable
	0.4	80	80	1 step
	0.42	87 to 117	64 to 79	1 step/variable
Sulfuric	0.5	18	70	4, variable
	2.4	15 to 25	13 to 27	2 step/variable
	Not specified	12, 25, 40	25,50, 100	Not specified
	0.3	25	20	12, 4,8,12&16

Barrier oxide layer is insoluble or dissolves slowly in the electrolyte. Generally, it is a very thin layer of tens to hundreds nanometer and formed rapidly under an applied voltage. The mechanism of barrier formation is simple, only two stages. In the first stage, the applied voltage is linearly increased with time. Meanwhile, the current density is kept at a constant value. In order to fix the constant current density, constant electric field strength across the barrier layer needs to be ensured. Therefore, voltage increases with the barrier layer growth until it reaches the formation

www.manaraa.com

voltage. Next, during the second stage, the formation voltage is kept as constant, but the barrier layer keeps growing. In this period, Al^{3+} ions move out from Al film into the electrolyte while O^{2-} and OH^- ions migrate from the electrolyte into Al film [31] as demonstrated in **Figure 1.3**. Oxide forms at the oxide/electrolyte interface, also at the metal/oxide interface. At the metal/oxide interface, O^{2-} and OH^- ions migrate from electrolyte to Al film which initials oxide growth here. There is about 60% oxide grow at the metal/oxide interface. Al^{3+} ions react with water molecules in electrolyte and porous oxide which drives the porous oxide growth at the oxide/electrolyte interface. The electrical resistance increases with the barrier layer thickness increase. Next, the metal/oxide and oxide/electrolyte interfaces stay planar and current flow decreases with time. In the end, the barrier layer has fully formed and stayed in balance. In this stage, the growth rate of the oxide layer decreased to a point which equals to its dissolution rate in electrolyte. During the barrier formation process, the resulting thickness of oxide layer is directly proportional to the voltage applied on the electrodes. Any initial surface defects have been filled by the forming oxide which leads to a generally uniform oxide surface.

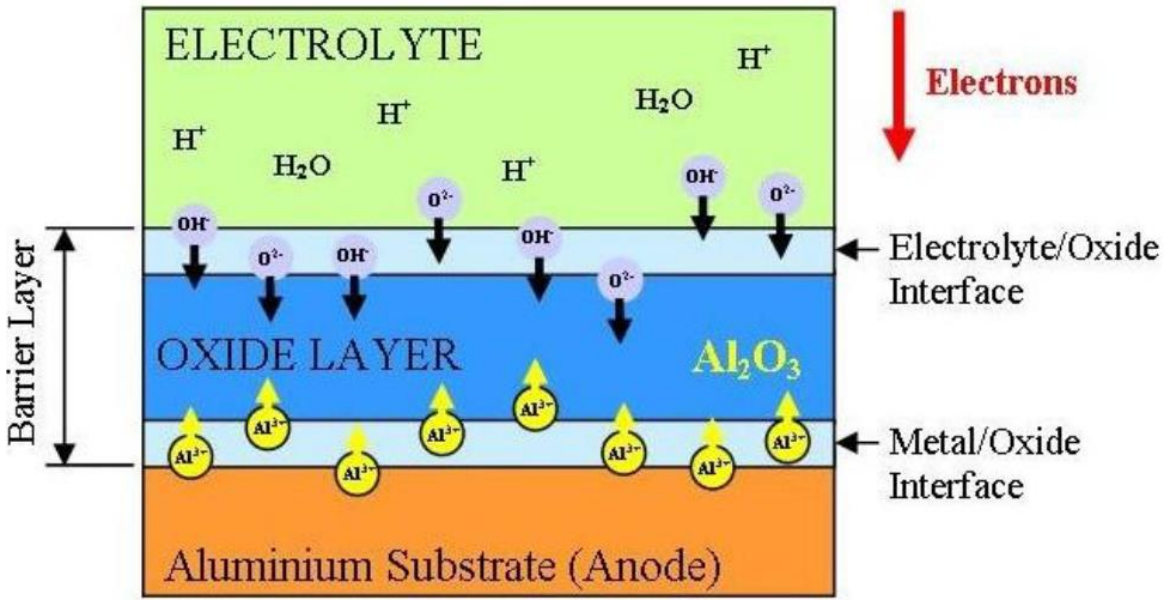

Figure 1.3 *Schematic of the major features involved in the formation of the barrier layer [29].*

www.manaraa.com

Different as the barrier layer formation, the porous structure grows from a thin nonporous oxide layer which is performed on the Al metal film. When the anodization starts, the nonporous oxide first formed at the metal/electrolyte interface. After some time, the nonporous oxide layer becomes stable with a constant thickness, the porous structure starts to grow on it. Once the pore wall is formed, the wall thickness keeps increasing with the time until the anodization process finish. Al metal substrate is consumed to support the nonporous and porous oxide formation. The resulting pore size, pore density, and thickness can be controlled by the select electrolyte, change the applied voltage, control temperature, etc. which already discussed in section 1.3.

There are two mechanisms to consume Al^{3+} ions form the Al metal substrate. First, Al^{3+} is expulsed directly by the applied electrical field as tons of positive charges are introduced on the anode electrode. Second, Al^{3+} is lost by dissolution in the electrolyte to supply the forming oxide layer. At the beginning of the anodization process, Al^{3+} ions move from Al metal substrate towards to electrolyte and metal/oxide interface is formed [32]. At the same time, O^{2-} ions are attracted from electrolyte to Al film, more precisely to the oxide/electrolyte which leads to oxide growth. During this period about 70% Al^{3+} and O^{2-} ions contribute to barrier oxide layer formation [33]. It is the pre-request condition for forming a porous oxide that Al^{3+} ions released from the Al-O bonds in the oxide lattice from the barrier oxide layer [34]. During the porous oxide formation, the barrier oxide layer keeps regenerating and transforming into a semi-spherical oxide layer with a constant thickness that forms the nanopore bottom. All these processes are schematically described in **Figure 1.4** [29].

www.manaraa.com

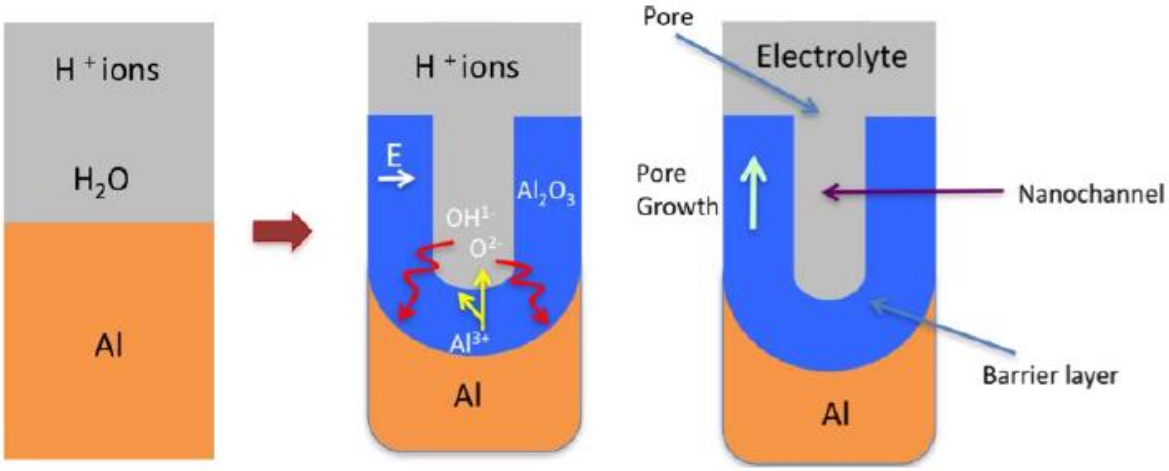

Figure 1.4 *Schematic of the nanopore formation mechanism [29].*

The detailed reaction of porous oxide layer formation is showing below [29]:

(1) Al^{3+} generated when voltage applied

$2Al \rightarrow 2Al^{3+} + 6e^{-}$

(2) The resulting reaction at the cathode produces hydrogen gas:

$6H^{+} + 6e^{-} \rightarrow 3H_2$

(3) Anode reactions occurring at the boundary of metal/oxide (Oxygen anions react with Al)

$2Al + 3O^{2-} \rightarrow Al_2O_3 + 6e^{-}$

(4) At the oxide/electrolyte boundary (Al cations react with the water molecules)

$2Al^{3+} + 3H_2O \rightarrow Al_2O_3 + 6H^{+}$

Finally, sum of the separate reactions at electrode (Overall anodization of Al equation)

$2Al + 3H_2O \rightarrow Al_2O_3 + 3H_2$

As shown in **Figure 1.5**, oxide layer steady-state growth is based on the balance between the oxide dissolution enhanced by the electrical field at oxide/electrolyte interface and the oxide growth by O^{2-} and OH^{-} ions accumulation at the metal/oxide interface. Al^{3+} ions are pushed through the barrier layer from metal/oxide interface towards to the oxide/electrolyte interface when local electric field

www.manaraa.com

reaches high enough, and higher local field introduces a higher Al^{3+} flow rate so that faster rate of nanopore structure formation. This also explains how oxide nanopore structure can be modified by changing anodization voltage.

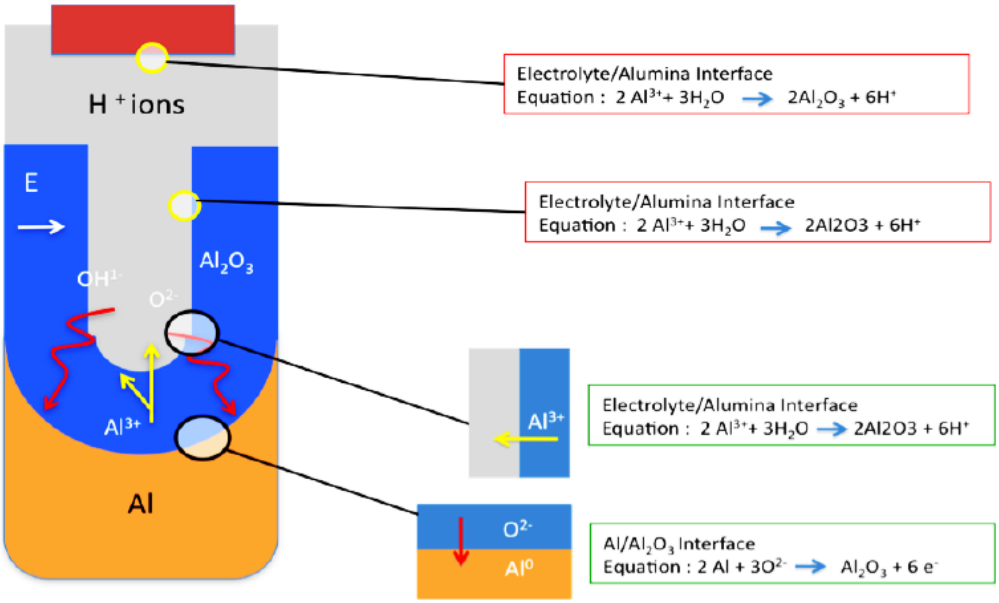

Figure 1.5 *Schematic of ion movement during pore formation [29].*

The generated mechanical stress at the metal/oxide interface during the barrier oxide layer formation also have effects on the self-ordered nanopore structure on oxide/electrolyte interface. At the early state, nanopore nucleate and develop randomly on the Al substrate surface. Gradually, with the barrier oxide layer growth, the nanopore structure start to immerge. As the anodization time increases, nanopore patterns continuously develop and become more ordered structure. During the nanopore formation, some pore can develop into different sizes and arrangements pores. However, at the final stage, all different pore arrangements decrease to a single, long-range ordered pore structure. Ideally, the NAO structure is an ordered hexagonal nanopore array with high density and uniformity [35] as shown in **Figure 1.6** [29].

www.manaraa.com

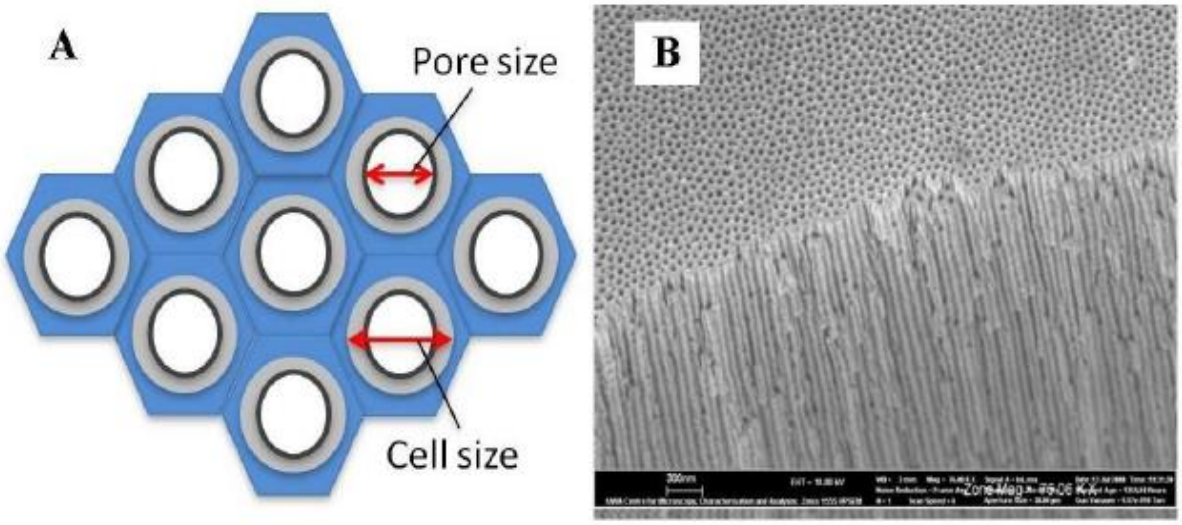

Figure 1.6 (A) *Schematic of the ideal densely packed hexagonal array of pores; (B) Actual cross-sectional view of a typical synthesized AAO membrane [29].*

1.5 AAO emerging applications

Due to the unique properties such as self-ordered nanopore structures, uniform pore size, high surface area, adjusted nanopore dimensions, interesting surface chemistry, etc. AAO become a very attractive material as a platform for numerous applications in a wide range of fields.

In the beginning, after AAO have been discovered and developed, the ordered AAO nanopore arrays have been extensively used as a template to fabricate different kinds of nanostructured materials due to its cost-effective characteristics. It has been widely used in industry to make some real products because the much simpler method to get the expected nano-arrayed structure rather than sue the traditional photolithography techniques which need more completed and sophisticated process like wet etching, dry etching, mask fabrication, etc. The fabricated nanowires by AAO templates have a further practical use, such as ion batteries, energy storage material, solar cells, and some electrical components like resistors, transistors, switches, and nanogenerators. There are some other applications by using AAO as a template, such as

www.manaraa.com

templated nanostructured conducting polymers, carbon nanotubes with designed electrical/optical properties, etc.

Recently, AAO has attracted more and more attention in the bio-nanotechnology field due to its unique and easy to modify surface chemistry. Especially, AAO has been used as a substrate or key component in chemical and biosensors, molecular separation sensors, biocompatible interface for cell growth. Recent research suggests that the material holds considerable potential as a drug or gene delivery carrier, enabling controlled release of therapeutic molecules. In the following discussion, we will focus on to introduce some interesting applications of AAO in sensing and biocompatibility.

1.5.1 Biosensing applications

Nanoporous AAO based biosensors are very promising in recent decades due to its advantages of the large surface area, chemical inertness, and easily modified surface chemistry [36]. There are two main types of biosensors based on AAO: optical biosensors and electrochemical biosensors. For an optical biosensor, AAO demonstrates appropriate transparency under UV and IR which allows direct detection by measuring the corresponding spectrum. Such as absorbance [37], reflection [38–41], fluorescence [42], chemiluminescence [43], surface plasmon resonance [38] and Raman scattering [44]. For electrochemical biosensors, they are based on the covalently or non-covalently bond if biomolecules on metal-coated AAO nanostructure surface. The most popular ones are enzymes biosensors, and glucose oxidase (GOx) and horseradish peroxidise (HRP) enzymes are the predominant model systems selected to convert a redox reaction into an electrical signal using an electrode transducer [45,46]. This is due to specific binding and catalytic activities of both enzymes. Various biomolecules can be detected by using either AAO based optical biosensors or electrochemical biosensors including proteins, enzymes, antibodies, DNA

www.manaraa.com

and even whole cells. In the following paragraphs, we will list some interesting applications by using AAO as cost-effective biosensors.

1.5.1.1 AAO based optical biosensors

For optical biosensors, photoluminescence (PL) biosensors are one of the most popular ones. Several unique biosensors have been developed. Jia et al. showed AAO could dramatically enhance PL intensity morin dye which embedded inside the AAO nanopores by introducing proteins such as trypsin or human serum albumen [47,48]. Feng et al. demonstrated detection of DNA hybridization could be greatly enhanced by the graded-band-gap dot modified AAO surface [43]. By using silane-glutaraldehyde functionalized and sulfhydryl-reactive AAO, Tanvir et al. had successfully immobilized glucose-6phosphate dehydrogenase (G6PD) and cytochrome from liver (CYP2E1) under retention of enzymes' activity [49]. Another popular type of AAO based optical biosensors is optical interference-based biosensors.

Interferences occur when the light incident and reflect back from AAO films, this is mainly due to the refractive index change. Pan and Rothberg developed ~6 um thick AAO membranes which functionalized with biotin and streptavidin to detect the complementary target DNA when it hybridized to the surface [40]. An AAO based interferometric immunosensor with immunoglobulin G (IgG) antibodies bounded on protein A was demonstrated by Sailor's group [39]. In another method, as shown in **Figure 1.7**, Kim et al. developed an optical sensor based on Au nanoparticles enabled localized surface plasmon resonance (LSPR) effects produced on the AAO surface. They have successfully detected thiolated probe DNA and hybridization of complementary target DNA. The lowest detection of hybridization of target DNA and aptamer-protein interactions is 10 pM and 1nM [38,50].

www.manaraa.com

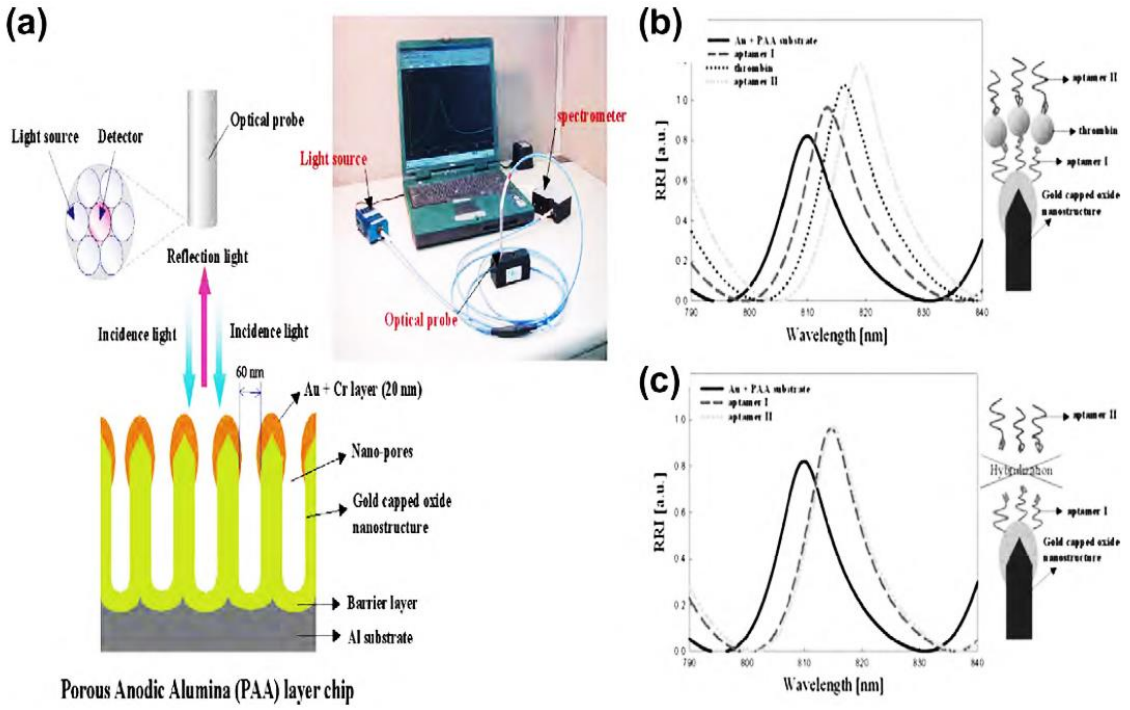

Figure 1.7 *Sandwich-type binding assay for thrombin using aptamer-functionalized Au-capped AAO pores. (a) Schematic of experimental setup and construction of LSPR and interferometry-based label-free optical biosensor with AAO chip. (b) Interferometric and LSPR characteristics of bare AAO layer chip (solid line), 10 lM aptamer I immobilized on Au-capped AAO surface (dashed line), binding reaction between 10 lM aptamer I and 1 lM thrombin on the chip surface (dotted line), and binding reaction between the aptamer I–thrombin complex and aptamer II (dashed double-dotted line). (c) Interferometric and LSPR characteristics of bare AAO layer chip (solid line), 10 lM aptamer I immobilized on chip surface (dashed line), and binding reaction between 10 lM aptamer I and 10 lM aptamer II (dashed double-dotted line) [38,50].*

1.5.1.2 AAO based electrochemical biosensors

For electrochemical biosensors by using nanoporous AAO membrane, as mentioned before glucose oxidase (GOx) and horseradish peroxidise (HRP) are two popular enzymes researchers interested in detecting. Xian et al. [51] fabricated nanoelectrode arrays of Prussian Blue (PB) via electrochemical deposition inside AAO pores to improve the analytical performance of glucose biosensors by electrocatalytic reduction of enzymatically liberated H_2O_2. The leaching of adsorbed enzyme introduced enzyme activity lose is a common problem for enzyme biosensors. Sometimes, coating layers can be used as stabilizing agents to solve this problem. Drader et al. have developed

www.manaraa.com

an AAO based GOx biosensor with improved sensitivity and enzymatic stability by depositing a protective chitosan layer. The biosensor demonstrated a good linear response for detecting glucose in the range up to 20 mM [52].

Besides GOx and HRP, antigen and DNA/RNA detection have also attracted researchers' attentions. Takmakov et al. [53] immobilized single-stranded DNA recognition elements on APTES-glutaraldehyde functionalized AAO surfaces. Compared to the DNA biosensor developed by Want et al. [54] which used a dynamic polymerase-extending (PE) method, Takmakov's biosensor demonstrated a significant resistance decrease based on DNA immobilization inside AAO pores (**Figure 1.8**). The limit of detection of this sensor was reported to be 0.5 nM.

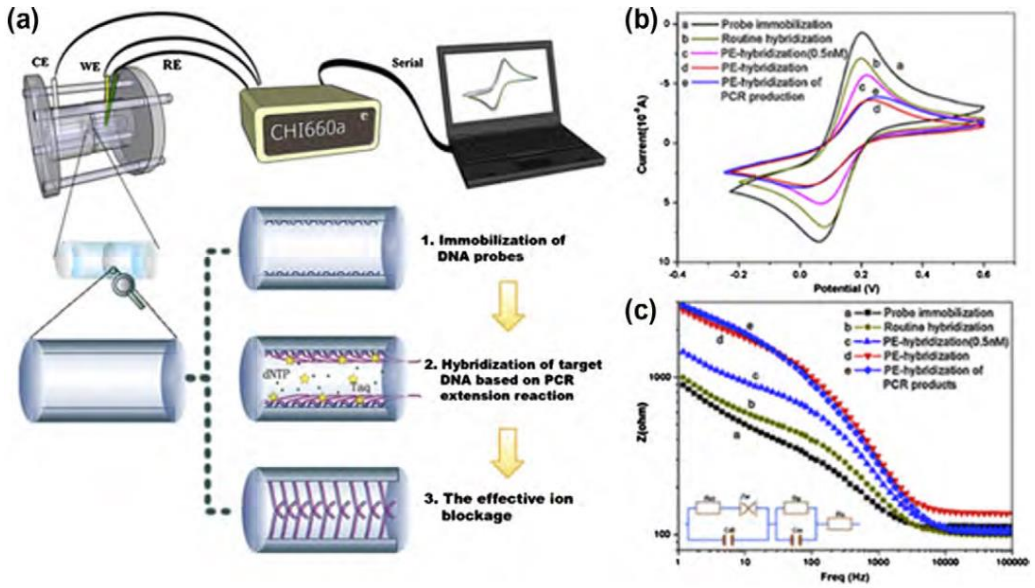

Figure 1.8 *(a) Schematic of an electrochemical DNA biosensor system and the mechanism of the dynamic polymerase-extending hybridization method (WE: working electrode; RE: reference electrode; CE: counter electrode). (b) CV in the region for [Fe(CN)6]3/4oxidation/reduction for the target DNA hybridization with different methods. (c) Impedance Bode plots after different reactions steps [54].*

1.5.2 Biocompatibility applications

Biocompatibility is related to the behavior of biomaterials in various contexts. The term refers to the ability of a material to perform with an appropriate host response in a specific situation

www.manaraa.com

[55]. Most of the medical devices and equipment are made of various types of materials, so the biocompatibility of each specific material used on those medical devices or equipment is very crucial. The main biocompatibility studies that have been performed on nanoporous AAO relate to in vitro cell culture studies and applications as orthopedic implants [56–65].

AAO with pore diameters range from 30 to 80 nm was reported to improve osteoblast adhesion and growth. Cells were physisorbed or covalently immobilized on the AAO surface via amino-silane-maleimide grafting chemistry (**Figure 1.9**) [57]. Modified AAO surface showed a clear preference of osteoblast adhesion after 1 day in culture, and cell-matrix production was visible after 2 days. Flamme et al. demonstrated that AAO has negligible toxic effects on b-cells in a vitro biocompatibility study. However, the cell viability reduced 94% when treat cell with latex particles [56]. Moreover, moderate inflammation has been found after a one-week in vivo implantation of PEF-coated AAO capsules into the intra-peritoneal cavity of rat. However, the inflammation response decreased after 4 weeks (**Figure 1.10**).

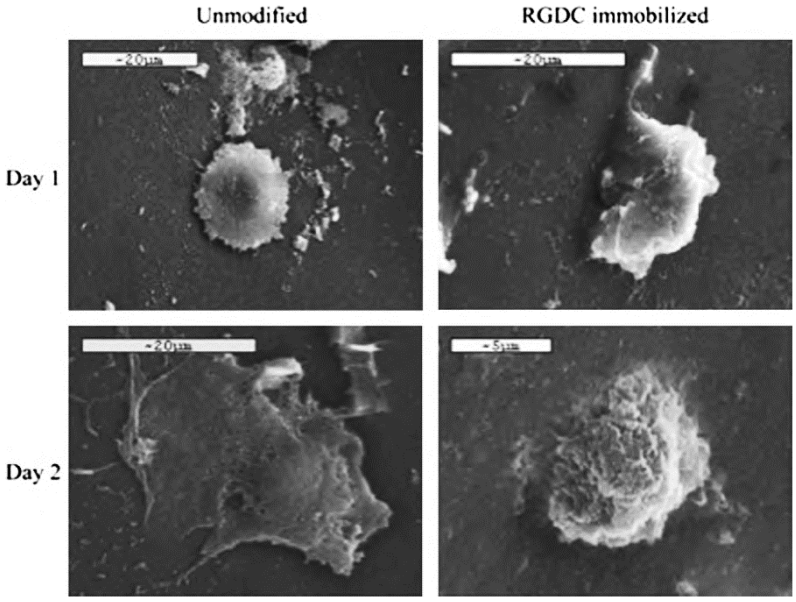

Figure 1.9 *SEM images showing osteoblast morphology after 1 and 2 days in culture on unmodified and arginine–glycine–aspartic acid–cysteine (RGDC)-immobilized AAO membranes [57].*

www.manaraa.com

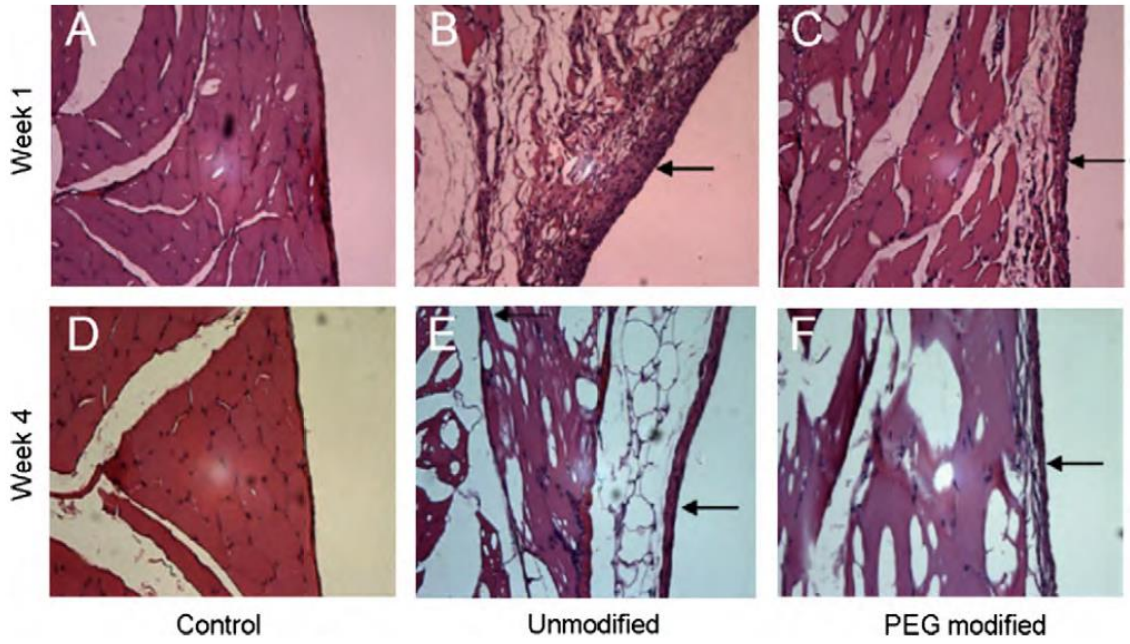

Figure 1.10 *Histological examination of tissue exposed to no material (A) and (D), unmodified AAO capsules (B) and (E), and PEG-modified AAO capsules (C) and (F) after 1 and 4 weeks. Arrows indicate the portion of the tissue that was exposed to the capsule [56].*

There are also some studies demonstrate the biocompatibility on uncoated AAO surfaces. For example, Karlsson et al. investigated cell interactions of primary human osteoblast-like cells on untreated AAO substrates (**Figure 1.11**) [61]. The results showed a normal osteoblastic cell growth during 2-weeks culture followed by an alkaline phosphate (ALP) increase which indicates the osteoblastic phenotype was retained on AAO substrates. Hoess et al. showed good biocompatibility of bare AAO surface by using two different pore diameters of 70 nm and 260 nm and a hepatoma cell line (HepG2). The results showed that cells were more easily adhere on the 260 nm AAO surface, they grew filopodia to penetrate into the underlying AAO pores which could not be observed on 60 nm AAO [63]. Moreover, Kant et al. observed the effect of different AAO pore structures on the growth of human neuroblastoma with SK-N-SH cells as the neuronal mode cell [66]. The result showed that the pore organization could have a direct impact on the neuronal cells growth orientation and phenotype. The most extensive cell response of the cells was on the

www.manaraa.com

substrates with mixed pore brush structures (**Figure 1.12 a-c**). Th highest cells attachment and frequent neuron-like phenotype with cytoplasmic processes and extensive cell to cell interactions were achieved on this type of substrates.

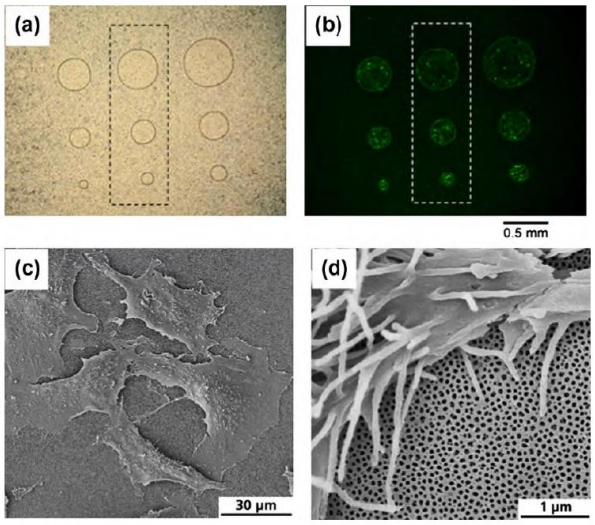

Figure 1.11 *(a) Brightfield and (b) fluorescence micrographs of HeLa cells on an AAO culture substrate with a 3 array of holes with diameters of 0.1–0.6 mm beneath. Adapted with permission from Ref. [67]. (c) SEM image of HepG2 cells on self-supporting AAO membrane (pore diameter 76 ± 10 nm) and (d) magnification of a cell border of (c) [61,63,68,69].*

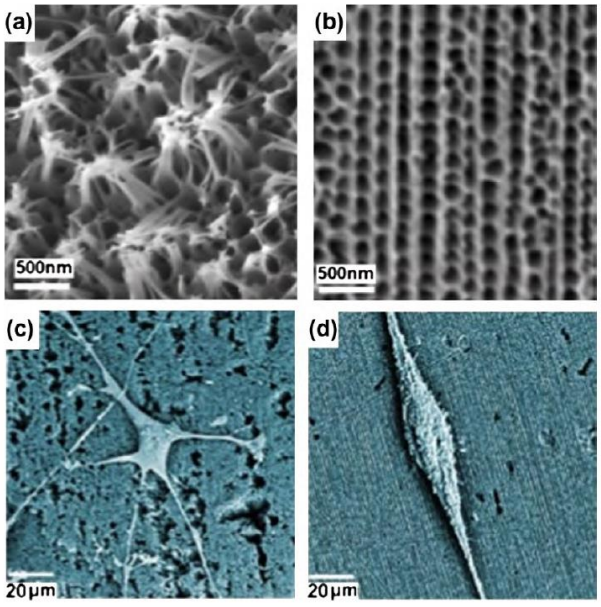

Figure 1.12 *SEM images of single neuroblastoma cells grown on different types of AAO showing the influence of pore structures on cell morphology. (a and b) AAO with nanobrushes show an extensive branching and interconnection of cells. (c and d) Aligned pores show a linear morphology of neuroblastoma cell directed by aligned pore structures [66].*

www.manaraa.com

1.6 Dissertation organization

In this dissertation, the mechanism of AAO fluorescence enhancement will be studied and presented. Then, based the fluorescence enhancement effect on AAO, two unique fluorescence base optical biosensors have been developed to test a specific DNA sequence and growth factor (TGF-β1) secreted from pancreatic stellate cells, respectively.

Chapter 1 will introduce background knowledge of anodic aluminum oxide (AAO). It includes a basic introduction of AAO, the history of AAO development, AAO fabrication method, self-ordered nanopore formation mechanism, the emerging applications in biosensing/bio-detection and biocompatible interface. This is to give a good understanding of AAO material and review some interesting applications of AAO in the biological field.

Chapter 2 will focus on the previous discovery work of AAO fluorescence enhancement. The enhancement effect has been demonstrated and evaluated by using different fluorescence dyes coated on the AAO surface. Image analysis and spectrum comparisons have been done to quantify the fluorescence enhancement factor on the NAO substrate compared to a glass substrate. Fluorescence enhancement has also been evaluated on micropatterned AAO.

Chapter 3 will explore the mechanism of fluorescence enhancement on AAO substrate and micropatterned AAO. Analytical studies will be conducted by collecting both experimental and simulation modeling results which help to further understand the enhancement mechanism. The effect of AAO nanopore properties such as pore size, porosity, and thin film thickness will also be discussed.

Chapter 4 will build a molecular beacon optical biosensor based on micropatterned AAO to detect a specific hairpin DNA sequence. The limit of detection (LOD) will be tested and finalized, the specificity and stability will also be checked.

www.manaraa.com

Chapter 5 will develop another fluorescence based optical biosensor on AAO substrate to detect and measure a specific type of transforming growth factor (TGF-β1) which secrets from pancreatic stellate cells (ITAF). Purified TGF-β1 will be used to demonstrate the sensor sensitivity and collect the reference data. Co-cultured medium of ITAF and Capan-1 will also be tested for checking if Capan-1 can stimulate TGF- β1 secretion from ITAF. The limit of detection will be tested and the specificity due to the sandwich assay structure will also be checked.

Chapter 6 will demonstrate the transcranial magnetic stimulation (MS) effect on single neuron cell (N27) growth on both glass and nanostructured AAO surface. Especially the cell proliferation, cell viability, and cell morphology. Different timepoints to apply MS will also be studied for checking its effect. Statistically analysis will be conducted to study the overall effect of MS on neuron cell growth. Cell growth on glass substrate and AAO substrate will be compared either with MS applied or without MS applied.

Chapter 7 will give the conclusion of this dissertation, and the future work will be recommended.

References

[1] S. Setch, A. Miyata, Sci. Pap. Inst. Phys. Chem. Res. (Tokyo) 19, 237 (1932)

[2] F. Keller, M.S. Hunter, D. L. Robinson, J. Electrochem. Soc., 100, 411 (1953)

[3] J. P. O'Sullivan, G.C. Wood, Proc. Roy. Soc. Lond. A. 317, 511-543 (1970)

[4] Smith, A. (Nov 26, 1974), Process for producing an anodic aluminum oxide membrane, retrieved 2016-10-11

[5] C. K. Preston, M. Moskovits, J. Phys. Chem. 92, 2957 (1988)

[6] M. Saito, M. Kirihara, T. Taniguchi, M. Miyagi, Appl. Phys. Lett. 55, 607 (1989)

[7] D. AlMawlawi, N. Coombs, M. Moskovits, J. Appl. Phys. 70, 4421 (1991)

www.manaraa.com

[8] C. K. Preston, M. Moskovits, J. Phys. Chem., 97, 8495 (1993)

[9] D. Routkevitch, T. Bigioni, M. Moskovits, J. M. Xu, Electrochemical Fabrication of CdS Nano-Wire Arrays in Porous Anodic Aluminum Oxide Templates, J. Phys. Chem., 100(33), 14037-14047 (1996)

[10] D. Routkevich, A. Tager, J. Haruyama, D. Al-Mawlawi, M. Moskovits and J. M. Xu, Nonlithographic Nanowire Arrays: Fabrication, Physics and Device Applications, IEEE Trans. Electron Dev., 43(10), 1646-1658 (1996)

[11] J. C. Hulteen, C. R. Martin, A general template-based method for the preparation of nanomaterials, J. Mat. Chem, v. 7(7) 1075 (1997)

[12] Buff, H. Liebigs Ann. Chem. 1857, 3, 265.

[13] Bengough, G. D.; Stuart, J. M. Improved process of protecting surfaces of aluminium of aluminium alloys. U.K. Patent 223,994, August 2, 1923.

[14] Diggle, J. W.; Downie, T. C.; Goulding, C. W. Chem. Rev. 1969, 69, 365.

[15] Sheasby, P. G.; Pinner, R. The Surface Treatment and Finishing of Aluminum and Its Alloys, 6th ed.; Finishing Publications Ltd. & ASM International: Materials Park, OH, and Stevenage, UK, 2001.

[16] Masuda, H.; Fukuda, K. Science 1995, 268, 1466.

[17] Masuda, H.; Satoh, M. Jpn. J. Appl. Phys. 1996, 35, L126.

[18] La Flamme KE et al. Biocompatibility of nanoporous alumina membranes for immunoisolation. Biomaterials 2007;28(16):2638–45.

[19] Vlassiouk I et al. ‘‘Direct’’ detection and separation of DNA using nanoporous alumina filters. Langmuir 2004;20(23):9913–5.

[20] Takmakov P, Vlassiouk I, Smirnov S. Application of anodized aluminum in fluorescence detection of biological species. Anal Bioanal Chem 2006;385(5):954–8.

[21] Yang Z et al. Piezoelectric urea biosensor based on immobilization of urease onto nanoporous alumina membranes. Biosens Bioelectron 2007;22(12):3283–7.

[22] Alvarez SD et al. A label-free porous alumina interferometric immunosensor. ACS Nano 2009;3(10):3301–7.

[23] Pan S, Rothberg LJ. Interferometric sensing of biomolecular binding using nanoporous aluminum oxide templates. Nano Lett 2003;3(6):811–4.

www.manaraa.com

[24] Wang M et al. Fluorescence detection of trace PCB101 based on PITC immobilized on porous AAO membrane. Analyst 2011;136(2):278–81.

[25] Li AP et al. Hexagonal pore arrays with a 50–420 nm interpore distance formed by self-organization in anodic alumina. J Appl Phys 1998;84(11):6023–6.

[26] Nielsch K et al. Self-ordering regimes of porous alumina: the 10 porosity rule. Nano Lett 2002;2(7):677–80.

[27] Furneaux RC, Rigby WR, Davidson AP. The formation of controlled-porosity membranes from anodically oxidized aluminium. Nature 1989;337(6203):147–9.

[28] Md Jani, A., Losic, D. and Voelcker, N. (2013). Nanoporous anodic aluminium oxide: Advances in surface engineering and emerging applications. Progress in Materials Science, 58(5), pp.636-704.

[29] Poinern, G., Ali, N. and Fawcett, D. (2011). Progress in Nano-Engineered Anodic Aluminum Oxide Membrane Development. Materials, 4(3), pp.487-526.

[30] Zaraska, L.; Sulka, G.D.; Szeremeta, J.; Jaskula, M. Porous anodic alumina formed by anodisation of aluminium alloy (AA1050) and high purity aluminium. Electrochim. Acta 2010, 55, 4377-4386.

[31] Thompson, G.E. Porous anodic alumina: Fabrication, characterisation and application. Thin Solid Films 1997, 297, 192-201.

[32] Patermarakis, G. Development of a theory for the determination of the composition of the anodising solution inside the pores during the growth of porous anodic Al2O3 films on aluminium by a transport phenomenon analysis. J. Electroanal. Chem. 1998, 447, 25-41.

[33] Palbroda, E. Aluminium porous growth—II on the rate determining step. Electrochim. Acta 1995, 40, 1051-1055.

[34] Shawaqfeh, A.T.; Baltus, R.E. Fabrication and characterization of single layer and muti-layer anodic alumina membrane. J. Membrane Sci. 1999, 157, 147-158.

[35] Jessensky, O.; Muller, F.; Gosele, U. Self-organised formation of hexagonal pore structures in anodic alumina. J. Electrochem. Soc. 1998, 145, 3735-3740.

[36] Fan X et al. Sensitive optical biosensors for unlabeled targets: a review. Anal Chim Acta 2008;620(1–2):8–26.

[37] Vlassiouk I et al. ‘‘Direct’’ detection and separation of DNA using nanoporous alumina filters. Langmuir 2004;20(23):9913–5.

www.manaraa.com

[38] Kim D-K et al. Label-free optical detection of aptamer-protein interactions using gold-capped oxide nanostructures. Anal Biochem 2008;379(1):1–7.

[39] Alvarez SD et al. A label-free porous alumina interferometric immunosensor. ACS Nano 2009;3(10):3301–7.

[40] Pan S, Rothberg LJ. Interferometric sensing of biomolecular binding using nanoporous aluminum oxide templates. Nano Lett 2003;3(6):811–4.

[41] Dronov R et al. Nanoporous alumina-based interferometric transducers ennobled. Nanoscale 2011.

[42] Takmakov P, Vlassiouk I, Smirnov S. Application of anodized aluminum in fluorescence detection of biological species. Anal Bioanal Chem 2006;385(5):954–8.

[43] Feng C-L et al. Graded-bandgap quantum- dot-modified nanotubes: a sensitive biosensor for enhanced detection of DNA hybridization. Adv Mater 2007;19(15):1933–6.

[44] Chang S et al. Nanoporous membranes with mixed nanoclusters for raman-based label-free monitoring of peroxide compounds. Anal Chem 2009;81(14):5740–8.

[45] Ansari SG et al. Glucose sensor based on nano-baskets of tin oxide templated in porous alumina by plasma enhanced CVD. Biosens Bioelectron 2008;23(12):1838–42.

[46] Grieshaber D et al. Electrochemical biosensors – sensor principles and architectures. Sensors 2008;8(3):1400–58.

[47] Jia RP et al. Enhanced photoluminescence properties of morin and trypsin absorbed on porous alumina films with ordered pores array. Solid State Commun 2004;130(6):367–72.

[48] Run-Ping J et al. Photoluminescence spectra of human serum albumen and morin embedded in porous alumina membranes with ordered pore arrays. J Phys: Condens Matter 2003;15(49):8271.

[49] Tanvir S et al. Covalent immobilization of recombinant human cytochrome CYP2E1 and glucose-6-phosphate dehydrogenase in alumina membrane for drug screening applications. J Membr Sci 2009;329(1–2):85–90.

[50] Kim D-K et al. Label-free DNA biosensor based on localized surface plasmon resonance coupled with interferometry. Anal Chem 2007;79(5):1855–64.

[51] Xian Y et al. Template synthesis of highly ordered Prussian blue array and its application to the glucose biosensing. Biosens Bioelectron 2007;22(12):2827–33.

[52] Darder M et al. Encapsulation of enzymes in alumina membranes of controlled pore size. Thin Solid Films 2006;495(1–2):321–6.

www.manaraa.com

[53] Takmakov P, Vlassiouk I, Smirnov S. Hydrothermally shrunk alumina nanopores and their application to DNA sensing. The Analyst 2006;131(11):1248–53.

[54] Wang L et al. A novel electrochemical biosensor based on dynamic polymerase-extending hybridization for E. coli O157:H7 DNA detection. Talanta 2009;78(3):647–52.

[55] Williams DF. On the mechanisms of biocompatibility. Biomaterials 2008;29(20):2941–53.

[56] La Flamme KE et al. Biocompatibility of nanoporous alumina membranes for immunoisolation. Biomaterials 2007;28(16):2638–45.

[57] Leary Swan EE, Popat KC, Desai TA. Peptide-immobilized nanoporous alumina membranes for enhanced osteoblast adhesion. Biomaterials 2005;26(14):1969–76.

[58] Popat KC et al. Influence of nanoporous alumina membranes on long-term osteoblast response. Biomaterials 2005;26(22):4516–22.

[59] Swan EEL et al. Fabrication and evaluation of nanoporous alumina membranes for osteoblast culture. J Biomed Mater Res Part A 2005;72 A (3):288–95.

[60] Popat KC et al. Osteogenic differentiation of marrow stromal cells cultured on nanoporous alumina surfaces. J Biomed Mater Res Part A 2007;80A(4):955–64.

[61] Karlsson M et al. Initial in vitro interaction of osteoblasts with nano-porous alumina. Biomaterials 2003;24(18):3039–46.

[62] Karlsson M et al. Nanoporous aluminum oxide affects neutrophil behaviour. Microsc Res Techn 2004;63(5):259–65.

[63] Karlsson M, Tang L. Surface morphology and adsorbed proteins affect phagocyte responses to nano-porous alumina. J Mater Sci: Mater Med 2006;17(11):1101–11.

[64] Ferraz N et al. Influence of nanoporesize on platelet adhesion and activation. J Mater Sci: Mater Med 2008;19(9):3115–21.

[65] Popat KC et al. Poly (ethylene glycol) grafted nanoporous alumina membranes. J Membr Sci 2004;243(1–2):97–106.

[66] Kant K et al. Nanopore gradients on porous aluminum oxide generated by nonuniform anodization of aluminum. ACS Appl Mater Interface 2010;2(12):3447–54.

[67] Prasad S, Quijano J. Development of nanostructured biomedical micro-drug testing device based on in situ cellular activity monitoring. Biosens Bioelectron 2006;21(7):1219–29.

[68] Hoess A et al. Cultivation of hepatoma cell line HepG2 on nanoporous aluminum oxide membranes. Acta Biomater 2007;3(1):43–50.

www.manaraa.com

[69] Ishibashi T et al. A porous membrane-based culture substrate for localized in situ electroporation of adherent mammalian cells. Sensor Actuat B: Chem 2007;128(1):5–11.

www.manaraa.com

CHAPTER 2. ANODIC ALUMINUM OXIDE BASED FLUORESCENCE ENHANCEMENT

2.1 Overview of fluorescence technology

Fluorescence technology has been widely used for sensing and detection in many different areas, such as microscopy imaging, a variety of biology detections (e.g., DNA arrays and gene sequencing), clinic diagnosis and environmental monitoring [1, 2]. It is the most common labeling technique in biosensing and bioimaging because of the diversity, simplicity, and good-biocompatibility of the organic dyes. However, the low fluorescence intensity of the organic dyes reduces the sensitivity and response of the applications. In addition, the poor photostability also restricts the organic dyes' sensitivity and reliability for long-term tracking and imaging. How to increase the sensitivity of fluorescence detection via methods that amplify the fluorescence intensity and improve the photostability of the organic dyes has been an active research topic of significant importance.

2.2 Fluorescence enhanced by nanomaterials

Nanomaterials have received much attention in recent years due to their unique chemical and physical properties resulting from their extremely small size, reduced surface, quantum confinement and macro quantum tunnel effects [3-6]. The advancement of nanotechnology has successfully made various nanostructures, such as nanoparticles, nanotubes, nanowires, and nanospheres [7-14]. Integrating these nanomaterials with fluorescence technology provides a great opportunity to enhance the performance of fluorescence-based applications.

The nanomaterials provide two approaches for fluorescence enhancement. One is through using the nanoparticles with/without organic dyes as the new probes to replace the traditional organic dyes in labelings, such as quantum dots (QDs), metal-core nanoparticles, silica

www.manaraa.com

nanoparticles and polymer nanoparticles [15-22]. Compared to traditional organic dyes, these new nanoparticles, with/without organic dyes, provide superior optical properties involving brighter fluorescence, higher photostability, and a wider selection of excitation and emission wavelength. The other approach is through surface enhanced fluorescence (SEF) by presenting a nanostructured surface in the vicinity of traditional organic dyes, such as a silver or gold island surface, aluminum nanostructured surface, grating metal surface and, ZnO/SiO_2 core/shell nanorod arrayed surface [23-29]. The strong electromagnetic field caused by surface plasmons and scattering by the nanostructured surface could dramatically enhance the fluorescence through the modifying of the relative molecular detection efficiency (*MDE*) by increasing the excitation rate, fluorescence quantum yield of the fluorophore and light collection efficiency.

2.3 Anodic Aluminum Oxide based fluorescence enhancement

Beyond the traditional nanomaterials used for fluorescence enhancement discussed above, anodic aluminum oxide which is a century-old material also was first discovered as a strong fluorescence signal enhance material in our group by X.Li et al. [30] in 2012. In this research, several fluorophores have been used to examine the enhanced effects on the nanostructured aluminum oxide surface, such as Rhodamine 6G (R6G), fluorescein sodium salt (FSS), Calcein AM and fluorescent brightening agents (FBA). As shown in **Figure 2.1** For all those fluorophores, they were uniformly applied on the NAO substrates which shows much stronger fluorescence signal compared to the ones with the same concentration and amount on ITO glass substrates. A series of experiments were conducted to examine the enhancement factor of AAO. It had been found that AAO surface demonstrated up to two orders of magnitude than the glass surface. This promoted AAO to be used in ultrasensitive fluorescence detection.

www.manaraa.com

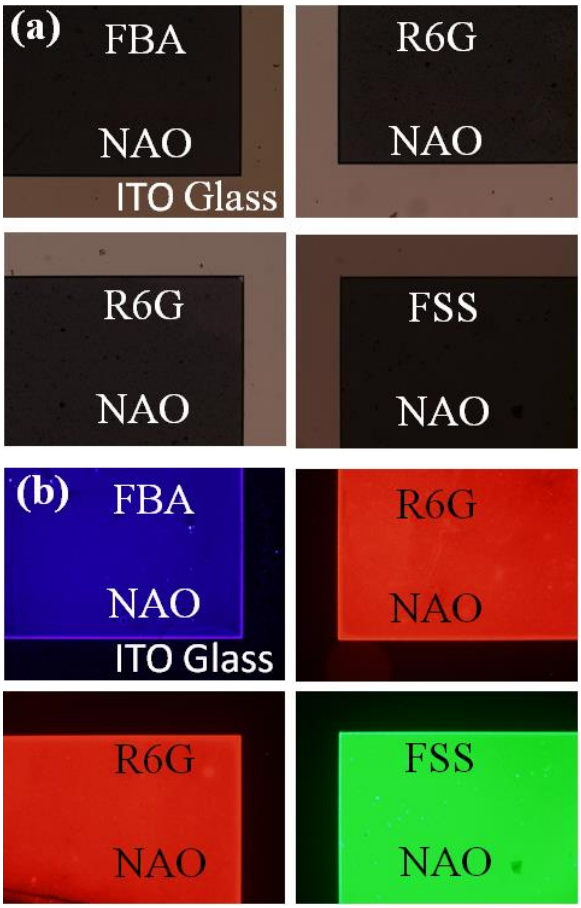

Figure 2.1 *(a) Bright field images of four partial ITO glass and partial NAO substrates; (b) corresponding fluorescence images of three different fluorescence dyes: FBA, R6G, and FSS on ITO glass and NAO substrates in (a) [30].*

In his research, surface area effect of AAO nanostructure has also been evaluating as shown in **Figure 2.2**. Same amount of R6G and FSS is spin-coated on AAO substrates and glass substrates of same size, respectively. The surface fluorophore amount on AAO and glass substrates were quantified by measuring fluorescence spectra after ultrasonically rinse both samples in DI water. Fluorescence images were taken after samples dry before and after rinse. The amount of fluorophores attached to the surface of AAO nanostructure is lower than that on the glass substrate based on systematic experiments, indicating the intrinsic property of AAO nanostructures plays a critical role in this enhancement.

www.manaraa.com

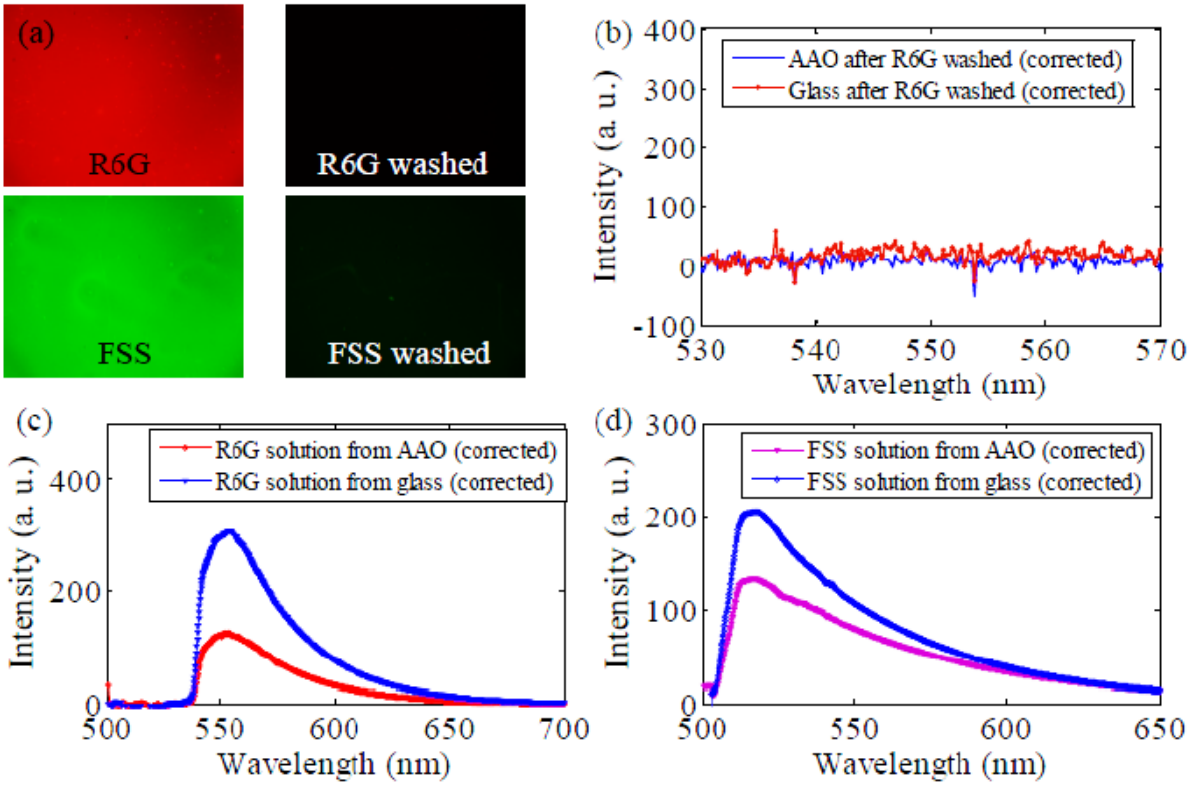

Figure 2.2 *(a) Fluorescence images of R6G and FSS on AAO nanostructure substrate before and after ultrasonic solution wash; (b) Fluorescence spectra of R6G on an AAO nanostructure substrate and a glass substrate after ultrasonic washing; (c) Fluorescence spectra of R6G solution ultrasonically washed from a AAO nanostructure substrate and a glass substrate with the same size; (d) Fluorescence spectra of FSS solution ultrasonically washed from an AAO nanostructure substrate and a glass substrate with the same size [30].*

2.4 Fluorescence enhancement on micropatterned AAO

In order to be integrated with microdevices or microfluidic devices for fluorescence-based biosensing applications, the size of the AAO is required to be in the micro scale. Therefore, the fabrication of the micropatterned AAO is necessary. In the following work of X.Li et al. [30], the ability of micropatterned NAO's fluoresce enhancement had also been evaluated. As shown in **Figure 2.3**, R6G and FSS showing strong fluorescence enhancement on micropatterned AAO than

www.manaraa.com

glass region. To be noticed that it had been found that the fluorescence enhancement factor is not affected by the size of the AAO pattern.

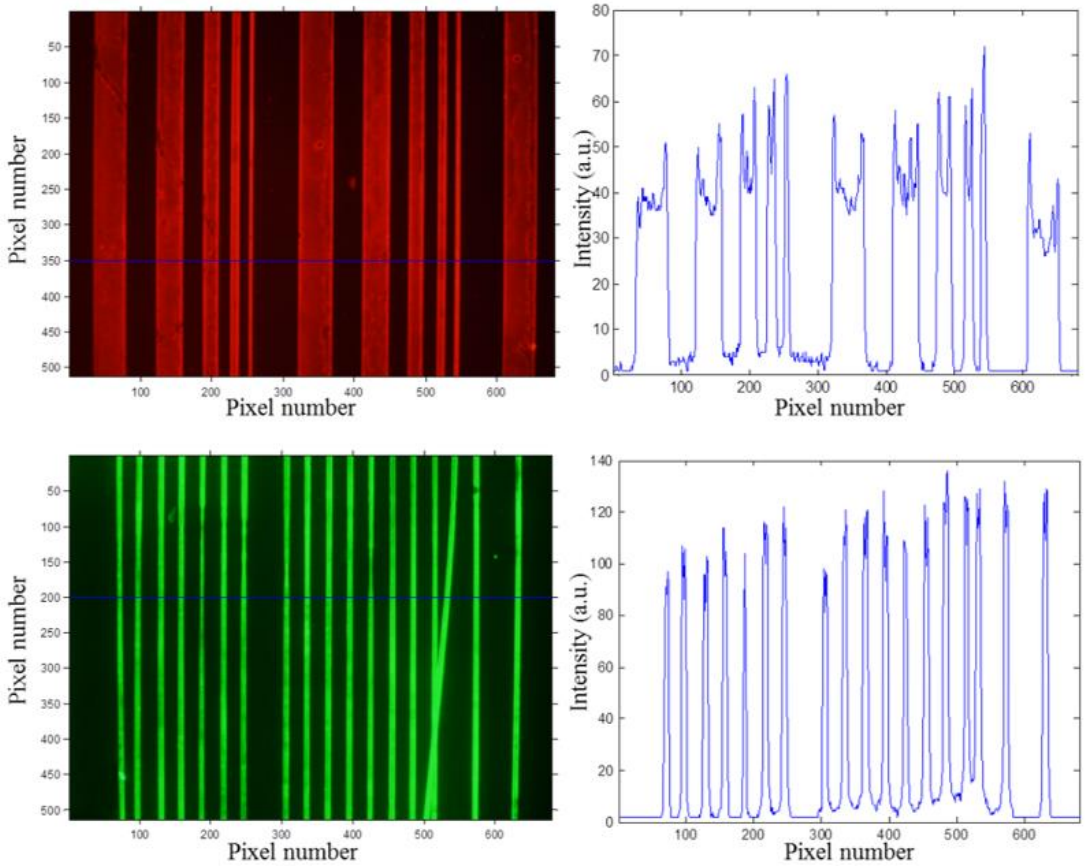

Figure 2.3 *Top-left: Fluorescence image of R6G on a micropatterned NAO substrate, showing the cutline for obtaining the image intensity; top-right: the corresponding image intensity along the cutline; bottom-left: fluorescence image of FSS on a micropatterned NAO substrate, showing the cutline for obtaining the image intensity; bottom-right: the corresponding image intensity along the cutline [30].*

References

[1] A. Q. Emili and G. Cagney, "Large-scale functional analysis using peptide or protein arrays," Nat Biotechnol, vol. 18, pp. 393-7, 2000.

[2] Y. Li, Y. T. Cu, and D. Luo, "Multiplexed detection of pathogen DNA with DNA-based fluorescence nanobarcodes," Nat Biotechnol, vol. 23, pp. 885-9, 2005.

www.manaraa.com

[3] E. Roduner, "Size matters: why nanomaterials are different," Chemical Society Reviews, vol. 35, pp. 583-592, 2006.

[4] S. Cuenot, C. Frétigny, S. Demoustier-Champagne, and B. Nysten, "Surface tension effect on the mechanical properties of nanomaterials measured by atomic force microscopy," Physical Review B, vol. 69, p. 165410, 2004.

[5] H. Yu, J. Li, R. A. Loomis, L.-W. Wang, and W. E. Buhro, "Two- versus three-dimensional quantum confinement in indium phosphide wires and dots," Nat Mater, vol. 2, pp. 517-520, 2003.

[6] J. A. Scholl, A. García-Etxarri, A. L. Koh, and J. A. Dionne, "Observation of quantum tunneling between two plasmonic nanoparticles," Nano Letters, vol. 13, pp. 564-569, 2012.

[7] D. V. McAllister, P. M. Wang, S. P. Davis, J.-H. Park, P. J. Canatella, M. G. Allen, et al., "Microfabricated needles for transdermal delivery of macromolecules and nanoparticles: Fabrication methods and transport studies," Proceedings of the National Academy of Sciences, vol. 100, pp. 13755-13760, 2003.

[8] S. Yang, X. Feng, S. Ivanovici, and K. Müllen, "Fabrication of graphene-encapsulated oxide nanoparticles: towards high-performance anode materials for lithium storage," Angewandte Chemie International Edition, vol. 49, pp. 8408-8411, 2010.

[9] G. K. Mor, O. K. Varghese, M. Paulose, K. Shankar, and C. A. Grimes, "A review on highly ordered, vertically oriented TiO2 nanotube arrays: Fabrication, material properties, and solar energy applications," Solar Energy Materials and Solar Cells, vol. 90, pp. 2011-2075, 2006.

[10] Q. Cai, M. Paulose, O. K. Varghese, and C. A. Grimes, "The effect of electrolyte composition on the fabrication of self-organized titanium oxide nanotube arrays by anodic oxidation," Journal of Materials Research, vol. 20, pp. 230-236, 2005.

[11] Q. Wan, Q. H. Li, Y. J. Chen, T. H. Wang, X. L. He, J. P. Li, et al., "Fabrication and ethanol sensing characteristics of ZnO nanowire gas sensors," Applied Physics Letters, vol. 84, pp. 3654-3656, 2004.

[12] M. J. Zheng, L. D. Zhang, G. H. Li, and W. Z. Shen, "Fabrication and optical properties of large-scale uniform zinc oxide nanowire arrays by one-step electrochemical deposition technique," Chemical Physics Letters, vol. 363, pp. 123-128, 2002.

[13] J. Jang and H. Ha, "Fabrication of hollow polystyrene nanospheres in microemulsion polymerization using triblock copolymers," Langmuir, vol. 18, pp. 5613-5618, 2002.

[14] J. Jang and J. H. Oh, "Fabrication of a highly transparent conductive thin film from polypyrrole/poly(methyl methacrylate) core/shell nanospheres," Advanced Functional Materials, vol. 15, pp. 494-502, 2005.

www.manaraa.com

[15] D. R. Larson, W. R. Zipfel, R. M. Williams, S. W. Clark, M. P. Bruchez, F. W. Wise, et al., "Water-soluble quantum dots for multiphoton fluorescence imaging in vivo," Science, vol. 300, pp. 1434-1436, 2003.

[16] W. C. W. Chan, D. J. Maxwell, X. Gao, R. E. Bailey, M. Han, and S. Nie, "Luminescent quantum dots for multiplexed biological detection and imaging," Current Opinion in Biotechnology, vol. 13, pp. 40-46, 2002.

[17] O. G. Tovmachenko, C. Graf, D. J. van den Heuvel, A. van Blaaderen, and H. C. Gerritsen, "Fluorescence enhancement by metal-core/silica-shell nanoparticles," Advanced Materials, vol. 18, pp. 91-95, 2006.

[18] K. Aslan, M. Wu, J. R. Lakowicz, and C. D. Geddes, "Fluorescent core-shell Ag@SiO2 nanocomposites for metal-enhanced fluorescence and single nanoparticle sensing platforms," J Am Chem Soc, vol. 129, pp. 1524-1525, 2007.

[19] H. Ow, D. R. Larson, M. Srivastava, B. A. Baird, W. W. Webb, and U. Wiesner, "Bright and stable core-shell fluorescent silica nanoparticles," Nano Letters, vol. 5, pp. 113-117, 2004.

[20] A. Burns, H. Ow, and U. Wiesner, "Fluorescent core-shell silica nanoparticles: towards "Lab on a Particle" architectures for nanobiotechnology," Chemical Society Reviews, vol. 35, pp. 1028-1042, 2006.

[21] M.-Q. Zhu, L. Zhu, J. J. Han, W. Wu, J. K. Hurst, and A. D. Q. Li, "Spiropyran-based photochromic polymer nanoparticles with optically switchable luminescence," J Am Chem Soc, vol. 128, pp. 4303-4309, 2006.

[22] C. Wu, C. Szymanski, and J. McNeill, "Preparation and encapsulation of highly fluorescent conjugated polymer nanoparticles," Langmuir, vol. 22, pp. 2956-2960, 2006.

[23] K. Aslan, Z. Leonenko, J. Lakowicz, and C. Geddes, "Annealed silver-island films for applications in metal-enhanced fluorescence: interpretation in terms of radiating plasmons," Journal of Fluorescence, vol. 15, pp. 643-654, 2005.

[24] J. R. Lakowicz, Y. Shen, S. D'Auria, J. Malicka, J. Fang, Z. Gryczynski, et al., "Radiative decay engineering: 2. effects of silver island films on fluorescence intensity, lifetimes, and resonance energy transfer," Analytical Biochemistry, vol. 301, pp. 261-277, 2002.

[25] J. Zhang and J. R. Lakowicz, "Metal-enhanced fluorescence of an organic fluorophore using gold particles," Opt Express, vol. 15, pp. 2598-2606, 2007.

[26] H. Zhang, D. Xu, Y. Huang, and X. Duan, "Highly spectral dependent enhancement of upconversion emission with sputtered gold island films," Chemical Communications, vol. 47, pp. 979-981, 2011.

www.manaraa.com

[27] K. Ray, M. H. Chowdhury, and J. R. Lakowicz, "Aluminum nanostructured films as substrates for enhanced fluorescence in the ultraviolet-blue spectral region," Analytical Chemistry, vol. 79, pp. 6480-6487, 2007.

[28] Y.-J. Hung, I. I. Smolyaninov, C. C. Davis, and H.-C. Wu, "Fluorescence enhancement by surface gratings," Opt Express, vol. 14, pp. 10825-10830, 2006.

[29] J. Zhao, L. Wu, and J. Zhi, "Fabrication of micropatterned ZnO/SiO2 core/shell nanorod arrays on a nanocrystalline diamond film and their application to DNA hybridization detection," Journal of Materials Chemistry, vol. 18, pp. 2459-2465, 2008.

[30] X. Li, et al, Optics Express, vol. 20, no. 19, 21272-21277 (2012).

www.manaraa.com

CHAPTER 3. STUDIES OF MECHANISMS AND CHARACTERISTICS OF THE FLUORESCENCE ENHANCEMENT ON ANODIC ALUMINUM OXIDE THIN FILM

Modified from a journal paper published in *Applied Nanoscience*

Xiangchen Che, Pan Deng, Jiming Song and Long Que

Abstract

Anodic aluminum oxide (AAO) thin film recently has been found as a new type of fluorescence enhancement nanomaterial. However, the mechanisms of the AAO thin film for the fluorescence enhancement have not been completely understood. Herein, the studies of its mechanisms are reported. Based on the experimental and modeling results, it has been found that the main contributing factor to the fluorescence enhancement is probably the plasmonic Al nanoparticles (NPs) embedded in the film, while the nanopore size and porosity of AAO thin film have a limited contribution. The characteristics of the enhancement have also been studied. It has been found that the enhancement is highly related to the gap between the fluorophore and the surface of the AAO thin film. Different excitation wavelength also results in different fluorescence enhancement. Using a simple model with a layer of Al NPs uniformly distributed in the thin film, the calculated enhancement factor of the electrical field and characteristics of the fluorescence enhancement match the experimental results.

3.1 Introduction

As one of the dominant technologies, fluorescence sensing and detection have been widely used for different applications such as medical imaging, biological detection and sensing due to its high sensitivity and multiplexing capability [1-2]. In order to further improve its sensitivity, a variety of advanced fluorescence substrates, including metallic (Au, Ag, Al) nanostructure

www.manaraa.com

substrates [3-6] and some semiconducting or metallic oxide nanostructure substrates [7-9], have been developed in the past decades. The physical mechanism for the metal-enhanced fluorescence (MEF) is due to the interactions of the excited fluorophores with surface Plasmon resonances in metals [3-6]. However, the metals in the metallic nanostructure substrates are usually expensive noble metals such as Au or Ag [3-6]. In addition, the fluorophores have to be separated from the surface of the metallic nanostructures by a thin layer (i.e., tens of nanometers) of dielectric material in order to avoid the fluorescence quenching effect, resulting in some complicated experimental procedures [3-6]. In contrast, for the non-metallic nanomaterials and nanostructures for fluorescence enhancement [7-10], a layer of the dielectric material is not required. In fact, the largest fluorescence enhancement can be achieved when the fluorophores are directly coated on their surfaces [11].

One of the non-metallic nanostructures for fluorescence enhancement is the recently reported anodic aluminum oxide (AAO) thin film [10-12]. AAO thin film-based fluorescence enhancement platform has many advantages over other nanostructures [4-5]. It is simple and inexpensive to fabricate both AAO thin film and AAO micropatterns. Furthermore, it is easy to integrate the AAO micropatterns within microdevices and microfluidic devices [13-14], thereby offering a cost-effective and even disposable platform for a variety of fluorescence-based applications such as microarray technology (both DNA microarray and protein microarray) and single cell imaging.

However, the mechanism of the fluorescence enhancement by the AAO thin film has not been completely understood. In this paper, first, the effect of the nanopore size and porosity of the AAO thin film on its fluorescence enhancement capability is examined. Second, the existence of Al nanoparticles (NPs) in AAO thin film has been found by using X-ray diffraction (XRD) measurement, and the fluorescence enhancement due to the embedded aluminum nanoparticles

www.manaraa.com

(Al NPs) is simulated using finite element analysis (FEA) and reported. Finally, the characteristics of AAO thin film-based fluorescence enhancement are reported.

3.2 Materials and methods

Fabrication of AAO thin film and micropatterns of AAO thin film: The fabrication process flow of the AAO thin film and AAO micropatterns on glass is the same as that described in [15]. In order to change the nanopore size and porosity of the AAO samples, the samples are immersed in an aqueous solution of 6% H_3PO_4 at room temperature with different etching time. Note that AAO is a self-organized material with the honeycomb-like structure formed by high-density arrays of uniform and parallel nanopores. Hence it is essentially impossible to control nanopore size and porosity in the thin film separately during the fabrication process [16].

Fluorescence dyes and experimental procedures: Two different fluorescent dyes propidium iodide (PI, Sigma-Aldrich) and fluorescein sodium salt (FSS, Sigma-Aldrich) are used in the experiments. The AAO samples are coated with the dyes with a concentration of 10 μg/ml by dip coating. The unbound dyes are washed away gently using deionized water (DI water). The fluorescent images are taken after the solutions on the substrates become dried, more accurately the images are taken immediately after no liquids can be observed on the substrates.

Fluorescence detection, imaging and analysis: All the fluorescent images have been taken using an inverted fluorescence microscope equipped with a mercury arc lamp source (Olympus, Inc.) and a high-resolution camera (DP74-Olympus, Inc.), which has the following filter sets: FITC (excitation filter: 460-495 nm; barrier filter: 500-540 nm); and TRITC (excitation filter: 545-565 nm; barrier filter: 580-620 nm). Specifically, For FSS, the FITC filter set is used for fluorescence

www.manaraa.com

measurement. The optical excitation spectrum is from 460 nm to 495 nm. While for PI, the TRITC filter set is used and the excitation optical spectrum is from 545 nm to 565 nm.

The fluorescence enhancement is calculated by analyzing the fluorescence images using the Imaging Processing toolbox in MatLab [9]. A MatLab program has been written to read the files of fluorescence images, which are then converted to grayscale images from the color images. A horizontal cutline is obtained through the fluorescence image, and the corresponding intensity is then plotted. In order to obtain accurate results, the fluorescence images of bare glass and bare AAO have been measured and used as references. All results have been corrected by subtracting the fluorescence images of the bare glass/AAO substrates.

Fluorescence enhancement modeling: Finite element analysis (FEA) is used to model the fluorescence enhancement of the AAO thin film using software ComSol^{TM} [17]. In one case, only the nanopore size and porosity effect on the fluorescence enhancement is considered. In another case, the fluorescence enhancement due to the Al NPs embedded in the AAO thin film is considered. For both cases, 3-dimensional (3D) model of the thin film is used. More details can be found in the following sections.

3.3 Results and discussion

AAO thin film vs. glass substrate:

In **Figure 3.1**, AAO thin film samples and glass substrate have been used to compare the fluorescence intensity when the same amount of fluorophore, fluorescein sodium salt (FSS, Sigma Aldrich) with a concentration of 10 μg/ml, is uniformly applied on their surfaces. Their SEM images and the corresponding fluorescence images are shown in **Figure 3.1a-c** and F**igure 3.1d-**

www.manaraa.com

f, respectively. The exposure energy and exposure time are fixed at 20% and 80ms for each sample during the imaging. As shown, both AAO thin film samples with clear nanopores (**Figure 3.1e**) and without clear nanopores (**Figure 3.1d**) have significantly enhanced fluorescence images in comparison with that of the glass substrate (**Figure 3.1f**), which can be up to 1,000 × [9-12]. Additionally, the AAO thin film sample with clear nanopores (**Figure 3.1b**) has increased fluorescence intensity (**Figure 3.1e**) over that (**Figure 3.1d**) of the AAO thin film sample without clear nanopores (**Figure 3.1a)**. Hence, the nanopore size and porosity of the AAO thin film do have effects on its fluorescence enhancement. The rearrangement of localized electric field (E-field) due to the light scattering effect by the AAO nanoporous structure is suggested as one possible mechanism [18], but it is far from sufficient to explain such a large amplification of the fluorescence signals compared to the glass substrate.

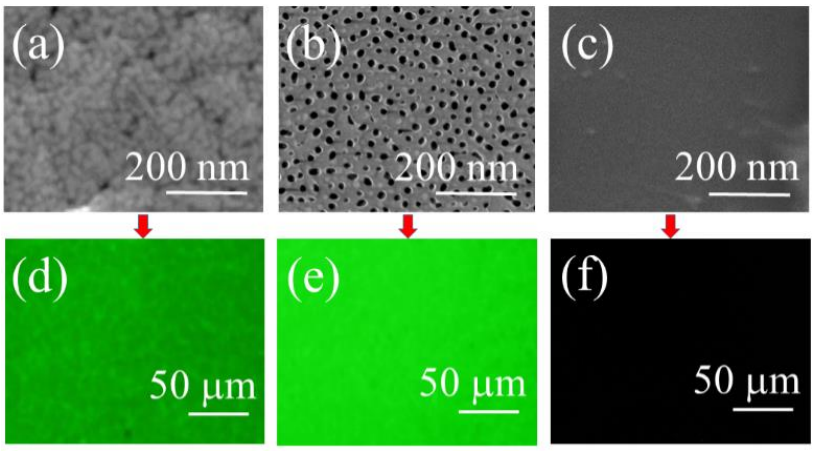

Figure 3.1 *(a) SEM image of AAO thin film sample without clear nanopores; (b) SEM image of AAO thin film with clear nanopores; (c) SEM image of the glass substrate; (d-f) the corresponding fluorescence images of (a-c), respectively*

Nanopore size and porosity effect:

In order to understand the effect of nanopore size and porosity of the AAO thin film on the fluorescence enhancement, several AAO thin film samples with different nanopore size and

www.manaraa.com

porosity have been prepared. SEM images of AAO thin film samples with increasing nanopore size and porosity are shown in **Figure 3.2a**. Their corresponding fluorescent images after being applied with the fluorescent dye FSS are shown in **Figure 3.2b**. The cutline-plots of the fluorescence intensity are shown in **Figure 3.2c**. While the fluorescence intensity on the AAO thin film samples increases up to 140× in comparison with the glass sample, the intensity increases only ~1.8× for the four AAO samples with the increased nanopore size and porosity, and essentially becomes saturated.

If only the nanopores are considered as the contributor for the enhancement, the calculated enhancement factor $(E/E_0)^2$ on the surface of AAO thin film, which is proportional to the fluorescence intensity [19], using finite-element analysis is given in **Figure 3.2d**. As shown, the enhancement factor is only 12× (for the AAO sample with D=35nm for nanopore size, P=6.2% for porosity) to 18× (for the AAO sample with D=90nm, P=47.3%) compared to the glass sample, indicating that the nanopore size and porosity is not the main contributor to the 140× enhancement of the fluorescence images compared to the glass sample.

Al nanoparticles (NPs) embedded in AAO thin film:

In order to identify the main contributor to the enhancement, the following samples are prepared: (a) **Sample 1**: standard coverslip glass; (b) **Sample 2**: 2 μm Al coated on coverslip glass; (c) **Sample 3**: 3.4 μm transparent AAO thin film (**Figure 3.3a**) on coverslip glass. (c) **Sample 4**: 3.4 μm half-transparent AAO thin film (**Figure 3.3b**) on coverslip glass. Fluorophore FSS with a concentration of 10 μg/ml is uniformly applied on these samples, and their fluorescence images are shown in **Figure 3.3c-f**. The cutline-plots of their fluorescence intensity is shown in

www.manaraa.com

Figure 3.3g. The fluorescence intensities on glass (Sample1) and Al surface (Sample2) are very low compared to those of transparent AAO sample (Sample3) and half-transparent AAO sample (Sample4). Note that the reflectance of the excitation light from **Sample 3** and **Sample 4** also contributes the fluorescence enhancement, but its contribution alone for the enhancement factor should be <= 4 × compared to the glass substrate [20-21].

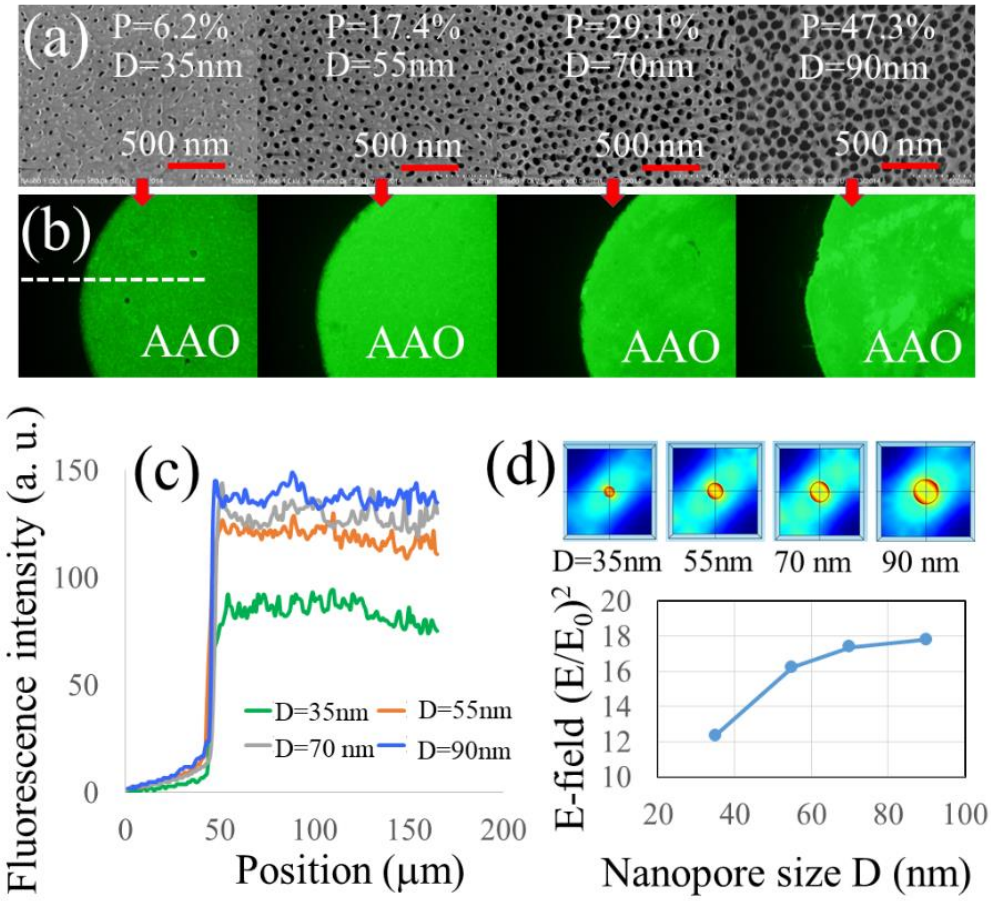

Figure 3.2 *(a) SEM images of AAO thin film samples with varied pore size (D=35nm, 55nm, 70nm, 90nm from left to right) and porosity (P=6.2%, 17.4%, 29.1%, 47.3% from left to right); (b) corresponding fluorescence images for the samples in (a) coated with the same concentration of FSS; (c) the corresponding fluorescence intensity along the horizontal cutline through the AAO surface; (d) the calculated E-field distribution and corresponding enhancement factor on the surface of the AAO thin film*

X-ray diffraction (XRD) measurements have been performed on **Sample 3** and **Sample 4**. A diffraction peak around 38° of Al (111) in **Figure 3.3h** is observed in **Sample 4**, indicating the

www.manaraa.com

existence of Al NPs inside **Sample 4**. No obvious diffraction peak of Al in **Sample 3** is observed. But it does not mean no Al NPs exist in **Sample 3** since if the percentage of amorphous Al or crystalline Al in the sample is 5% or lower, their peaks cannot be clearly visible in the XRD diagram due to the detection limit of the XRD equipment. It should be noted that for **Sample 3**, it requires 150-minute anodization to obtain a transparent AAO thin film. In contrast, **Sample 4** is fabricated by reducing the anodization time to 140 minutes, resulting in a half-transparent AAO sample. Specifically, for **Sample 4**, there is still a ~10 mA current flow with a 40 V applied voltage before it is taken out of the fabrication tank, indicating some Al NPs should still remain inside the AAO film.

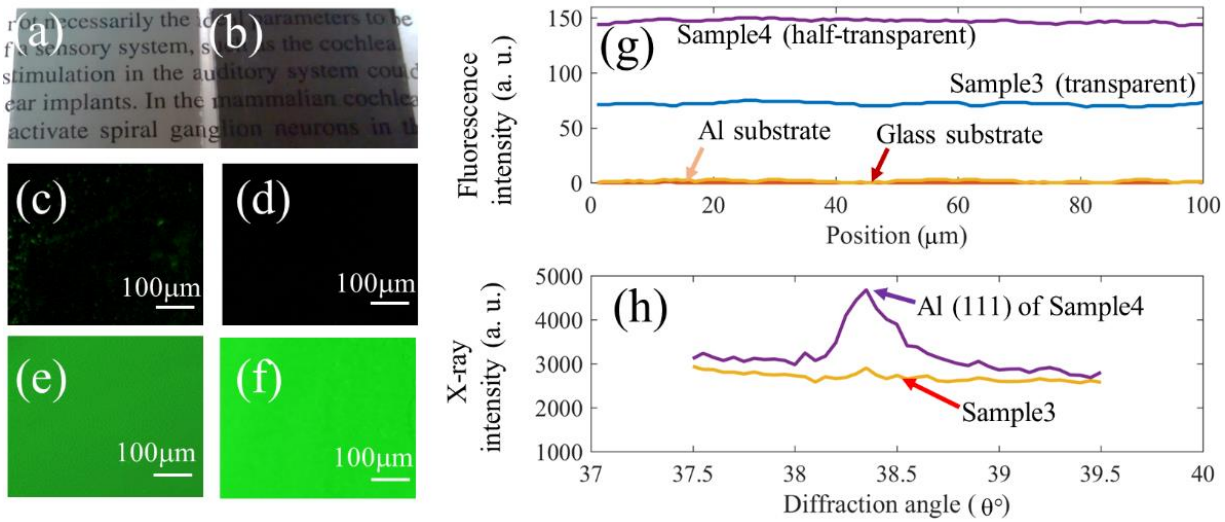

Figure 3.3 *(a) photo of a transparent AAO thin film sample (Sample3); (b) photo of a half-transparent AAO thin film sample (Sample4); Measured fluorescence images of (c) Sample1: glass, (d) Sample2: Al coated glass, (e) Sample3: transparent AAO sample, and (f) Sample4: half-transparent AAO sample; (g) the corresponding cutline plots of the fluorescence intensity for the four samples; (h) Diffraction peak of Al (111) clearly shown in Sample4 by X-ray diffraction (XRD) measurements*

Based on the plasmon-enhanced fluorescence mechanism [19, 22], the Al NPs might be the main contributor to the fluorescence enhancement of AAO thin film [23]. However, the sizes, locations, and distributions of Al NPs in the thin film cannot be determined by currently available

www.manaraa.com

equipment. In order to simulate the effect of Al NPs on the fluorescence enhancement, their sizes, locations, and distributions have to be assumed.

SEM image of 2 μm Al deposited on glass substrate before anodization is shown in **Figure 3.4a**. The nanoscale Al domains (i.e. Al NPs) is clearly visible with a typical size in the range from ~100 nm to ~200 nm. SEM image of the sample after anodization is shown in **Figure 3.4b**. The nanopores are clearly visible in each nanoscale AAO domains. Given the typical size of the nanoscale domains of Al thin films and AAO thin films, it is reasonable to assume that the diameter of the remaining Al NPs embedded in the AAO thin film is 0 nm to ~150 nm after anodization. Since the locations and distributions of the Al NPs inside the thin film are not known, in order to examine the contribution of the Al NPs to the enhancement *qualitatively*, a simple model, assuming layers of Al NPs embedded and distributed uniformly in the AAO thin film, is proposed in **Figure 3.4c**. In the model, D_{NP} is the diameter of Al NPs. g_0 is defined as the gap between two adjacent Al NPs. g_1 is defined as the gap from the center of two adjacent NPs to the surface of the AAO thin film. The relative permittivity of AAO and Al NPs is set to be 3.13 and 0.55493+i5.0513 respectively [24-26]. The AAO sample is illuminated by a light with a wavelength of 475 nm, the central wavelength used to get the fluorescence images in **Figure 3.3**. For the wavelength of 550 nm, the relative permittivity of AAO and Al NPs is set to 3.13 and 0.78941+i5.8919, respectively [24-26].

The representative 3D mesh of the model showing two Al NPs embedded in AAO thin film with a periodic boundary condition in both X-Y plane is given in **Figure 3.4d**. One calculated local E-field distribution around the two Al NPs is shown in **Figure 3.4e**. It is known that Plasmon-enhanced fluorescence is a two-step process [19,22,23,28]: (1) local E-field enhancement occurs around the plasmonic NPs at the incident frequency. In this step, the intensity of a fluorophore's

www.manaraa.com

emission is proportional to the electric field intensity (which is proportional to the square of the electric field) of the light exciting the molecule, so an enhanced electric field will enhance the excitation of fluorophores close to the AAO surface. (2) Another enhancement effect occurs when the fluorophore emission wavelengths overlap with the resonant wavelengths of the NPs inside AAO thin film. Enhanced extraction occurs when light emitted by fluorophores couples into leaky eigenmodes and is re-radiated such that it can be easily detected by the measurement instrumentation. The combination of these two effects is the main contribution to enhance the fluorescence signal on NPs embedded AAO thin film. Overall, the fluorescence enhancement factor may be proportional to the fourth power of the enhancement of the local E-field which is $(E/E_0)^4$ [23,28]. In addition, some proportion of light is reflected due to the transparency of AAO thin film which also introduces some enhancement (up to 4x) compared to the glass surface.

Several modeling-based calculations have been conducted based on the Al NPs embedded model. First, the effect of different numbers of Al NPs layers embedded in the AAO thin film on the fluorescence enhancement has been evaluated assuming the excitation light wavelength is 475 nm. As shown in **Figure 3.4f**, it has been found that the enhancement factors have small changes (<8%) with one layer of Al NPs compared to those with two or three layers of Al NPs if g_1=30 nm, g_0=10 nm and D_{NP}=50 nm. Similar small changes have been found by changing the values of g_1, g_0 and D_{NP}. Hence, in the following modeling, only one layer of Al NPs in the AAO thin film is assumed.

Second, as aforementioned, it is reasonable to assume that the diameter D_{NP} of the remaining Al NPs embedded in the AAO thin film is ~20 nm to ~150 nm after anodization. In **Figure 3.5**, two representative modeling results of the E-field enhancement with varying g_0 and g_1 are given, assuming D_{NP} = 50 nm and 100 nm, respectively and the excitation light wavelength is 475 nm. If

www.manaraa.com

the size of Al NPs is 50 nm, the calculated enhancement factor at the surface with the different g_0 and g_1 is plotted in **Figure 3.5a**. The simulated results (enhancement factor) with 5 nm < g_0 <20 nm and 5 nm < g_1 <35 nm match the experimental results (~140 × in **Figure 3.2**). In contrast, if the size of Al NPs is 100 nm, the calculated enhancement factor at the surface with the different g_0 and g_1 is plotted in **Figure 3.5b**. The simulated results (enhancement factor) with g_0 > 20 nm and g_1 <15 nm match the experimental results (~140 × in **Figure 3.2**).

Basically, the enhancement factor is highly related to the sizes, locations and distributions of the Al NPs inside the AAO thin film. The experimental results, combined with the simulated results using this simple model, verify that the main contribution to the enhancement might be probably due to the plasmonic Al NPs.

Characteristics of the AAO substrate for fluorescence enhancement:

(1) Gap-dependent fluorescence enhancement

The fluorescence enhancement vs. the gap between fluorophores and AAO surface has been examined. It has been found experimentally that when the fluorophores are directly deposited on AAO surface, the largest fluorescence is achieved. When a layer of ~100 nm PMMA is sandwiched between AAO surface and fluorophores, which means the gap between the fluorophore (FSS) and AAO surface is ~100 nm, the enhancement of the fluorescence intensity reduces a lot or becomes negligible. As shown in **Figure 3.6a**, when the gap is ~100 nm, essentially the fluorescence intensity becomes similar to that when the fluorophore is deposited on a glass substrate. Calculated results using FEA in **Figure 3.6b** shows that the E-field enhancement decay significantly away from the AAO surface (assume g_0 =10 nm, g_1 =30 nm and D_{NP} = 50 nm, the excitation light wavelength is 475 nm), and negligible enhancement is observed when the distance away from the

www.manaraa.com

AAO surface is 100 nm, similar to the experimental results in **Figure 3.6a**, confirming that the fluorescence enhancement of AAO substrate is gap-dependent.

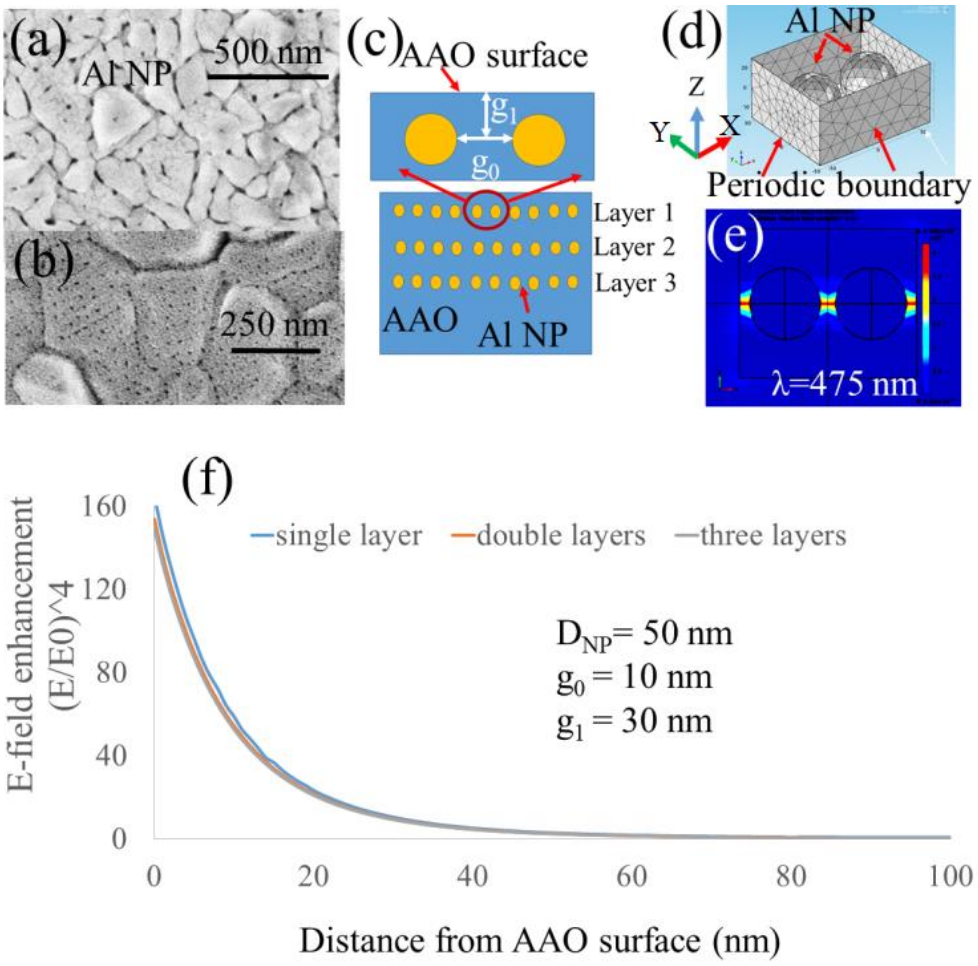

Figure 3.4 *(a) SEM image of Al NPs in the Al layer deposited on glass substrate by e-beam evaporation before anodization; (b) SEM image of AAO thin film after anodizing the Al thin film; (c) sketch of a simple model assuming three layers of Al NPs uniformly distributed in AAO thin film. g0 is the gap between two adjacent Al NPs, g1 is the gap from the center of two adjacent NPs in the top layer to the surface of the AAO thin film; (d) a mesh model of the Al NPs embedded in the AAO thin film with periodic boundary in X-Y plane; (e) a representative calculated E-field distribution of the model; (f) representative plots showing the calculated enhancement factors with one-layer Al NPs, two-layer NPs and three-layer NPs embedded in the AAO thin film, assuming DNP=50nm, g0=10nm, and g1=30nm*

(1) Excitation wavelength effect on fluorescence enhancement

Two different fluorophores (FSS and PI) of the same concentration have been applied on the samples with AAO micropatterns, different enhancements for these two fluorophores have been

www.manaraa.com

observed (**Figure 3.7a-b**). Specifically, the fluorescence intensity of FSS is larger than that of PI. In order to understand the difference, the bare AAO micropatterns under the same excitation light (475 nm and 550 nm) for FSS and PI have been examined, respectively. It shows that the scattering light intensity of the bare AAO micropatterns under blue light (475 nm) excitation for FSS (**Figure 3.7c**) is larger than that of green light (550 nm) excitation for PI (**Figure 3.7d**). The measured fluorescence intensities for FSS and PI coated AAO micropatterns, and bare AAO micropatterns are plotted in **Figure 3.7e**. Clearly, the fluorescence intensity of FSS is higher than that of PI. It should be noted that these experiments can also be carried out on AAO thin film.

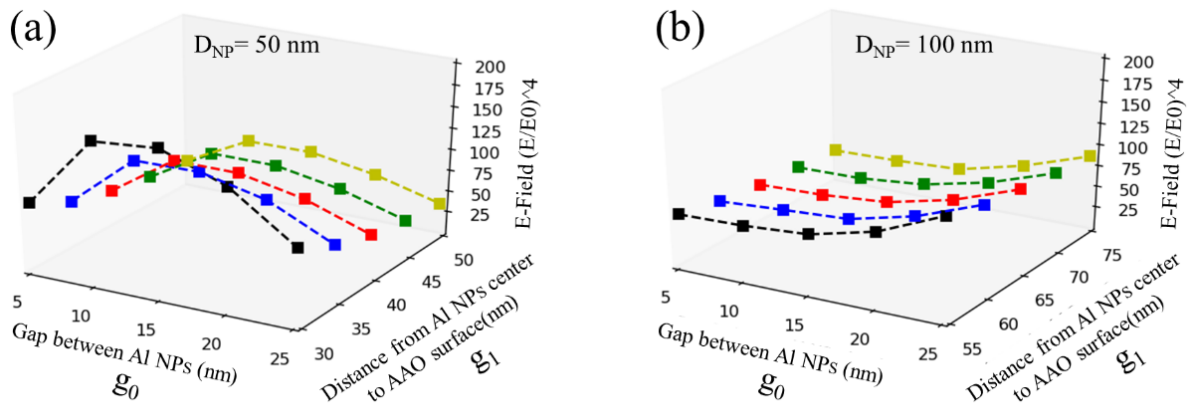

Figure 3.5 *Representative plots showing the relationship between the calculated enhancement factors and g0 and g1: (a) DNP=50nm, (b) DNP=100nm*

This difference has been qualitatively verified by calculating the E-field on the AAO surface using FEA. The modeling results are shown in **Figure 3.7f-g**. In **Figure 3.7f**, g_1 is fixed as 30 nm, D_{NP} is fixed as 50 nm, and g_0 is varied from 5 nm to 25 nm, the enhancement factors on the surface of AAO thin film have been calculated for both 475 nm and 550 nm light excitation. In **Figure 3.7g**, g_0, g_1 and D_{NP} are fixed as10 nm, 30 nm and 50 nm, respectively, the E-fields on and away from the AAO surface have been calculated for both 475 nm and 550 nm light excitation. For both

www.manaraa.com

cases, the calculated E-field enhancement at the AAO thin film surface under 475 nm light excitation is clearly larger than that under 550 nm light excitation, verifying the fluorescence intensity of FSS coated AAO thin film is larger than that of PI coated AAO thin film.

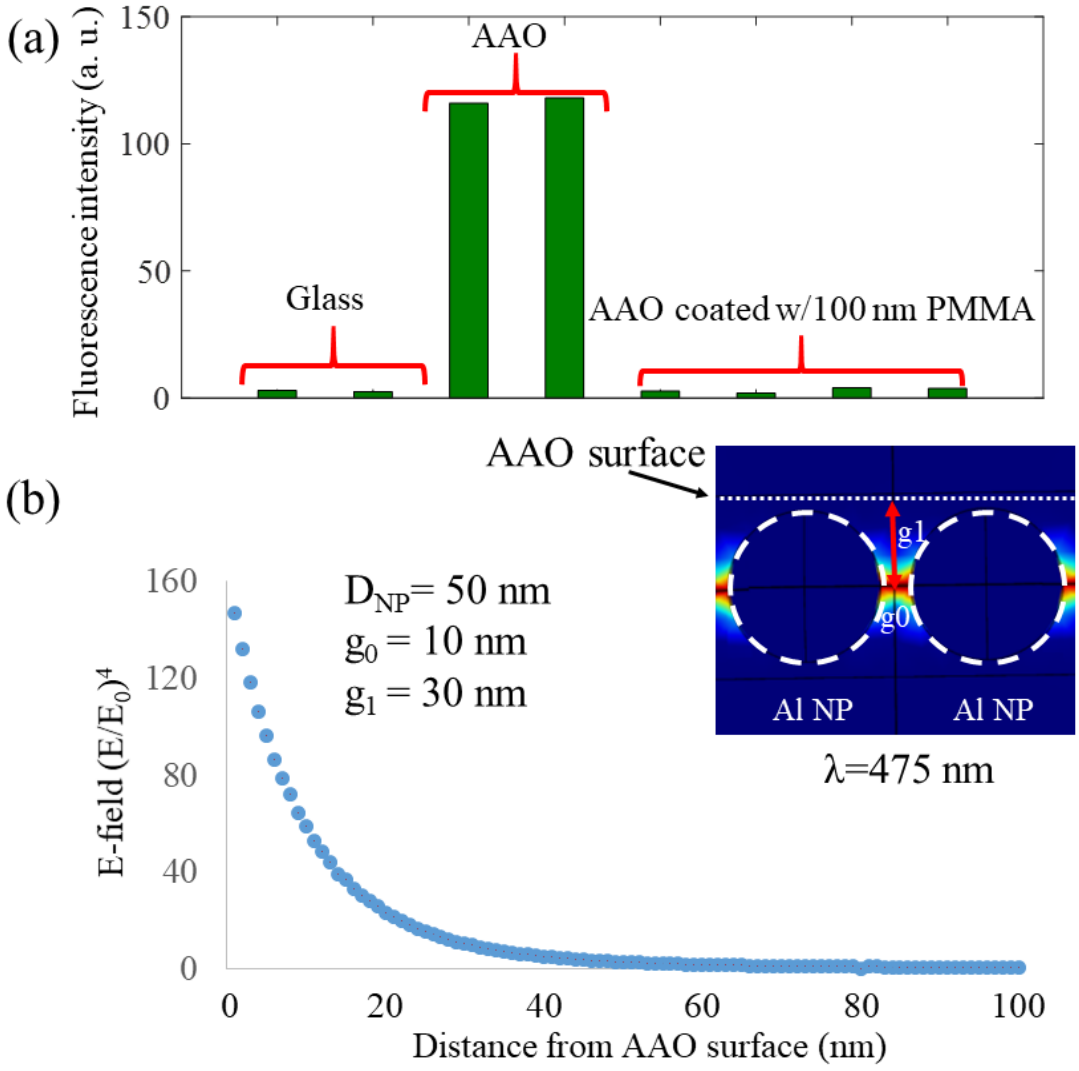

Figure 3.6 *(a) Measured fluorescence intensity on different substrates; (b) modeling results: plots showing the relationship between the calculated enhancement factor and the distance from the surface of AAO thin film, assuming DNP = 50nm, g1 = 30 nm, and g0 = 10 nm.*

It has been reported that Al NP shows strong Plasmon resonance in the visible and ultraviolet (UV) spectral region, and most importantly its Plasmon resonant wavelength shifts with its size and shape [23]. For the AAO samples in the experiments, 475 nm light *might* be closer to or have

www.manaraa.com

larger overlap with the excitation light to achieve the Plasmon resonant wavelength of Al NPs embedded in the AAO thin film than 550 nm light [23], thus resulting in larger E-field on the AAO thin film surface and leading to larger fluorescence enhancement as shown in **Figure 3.7a-d**.

In order to verify this assumption, the measured light transmission of AAO samples (Sample3 and Sample4) and glass sample is shown in **Figure 3.7h**. The sketch of the light transmission and reflection from the AAO sample is given in the inset of **Figure 3.7h**. The absorption coefficient of the AAO samples can be obtained from the following formula [27]:

$$\alpha = \frac{-1}{d} ln(\frac{R''+T'}{1-R'}) \qquad (3.1)$$

Where $R'=(r_{01})^2= [(n_0-n_1)/(n_0+n_1)]^2$, representing the reflection from surface 1 (the interface between air and AAO top surface layer). $R''= (r_{12})^2 = [(n_1-n_2)/(n_1+n_2)]^2$, representing the reflection from surface 2 (the interface between AAO bottom layer and glass top surface). $n_0=1$ is the refractive index of air. n_1 and n_2 are AAO refractive index and glass refractive index, respectively. $n_1=1.7766$ and $n_1=1.7704$ for AAO thin film at 475nm and 550nm, respectively [25]. $n_2=1.5$ for glass at both 475nm and 550nm. $T'= [n_2/n_0] \times [(n_0+n_2)/(2n_2)]^2 \times T$, where T is the measured transmittance through the samples. d is the thickness of the AAO film, which is 3.4 μm for both Sample3 and Sample4. Based on the measurements and Formula (1), the absorption coefficients at 475 nm is found to be 876/cm, and at 550 nm to be 673/cm for Smaple3, respectively [27]. Similarly, the absorption coefficients are 4996/cm at 475 nm and 4996/cm at 475 nm and 3120/cm at 550 nm for Smaple4, respectively. Basically, the absorption coefficients at 475 nm for both Sample 3 and Sample 4 are larger than those at 550 nm, indicating the samples absorb the light more at wavelength of 475 nm than that at 550 nm. Hence, Larger E-field on the AAO thin film surface is achieved, thereby resulting in larger fluorescence enhancement.

www.manaraa.com

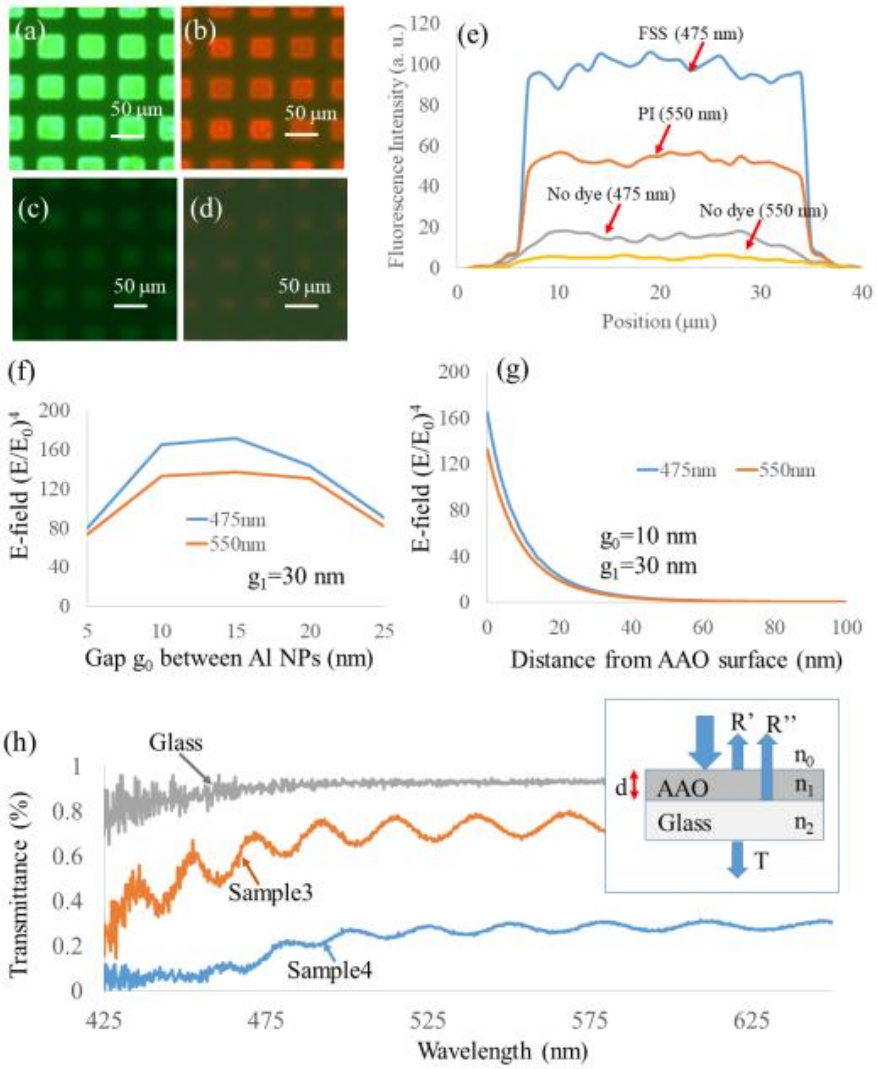

Figure 3.7 *Fluorescence images of (a) FSS coated AAO thin film sample under excitation light of 475 nm; (b) PI coated AAO thin film sample under excitation light of 550 nm; (c) a bare AAO thin film sample under excitation light of 475 nm; (d) a bare AAO thin film sample under excitation light of 550 nm; (e) the cutline-plots of the fluorescence intensity for the four samples; (f) the calculated enhancement factors at the surface of AAO thin film under excitation lights of 475 nm and 550 nm assuming DNP=50 nm and g1=30 nm, respectively; (g) the calculated relationship between enhancement factors and the distance from the surface of the AAO thin film under excitation lights of 475 nm and 550 nm assuming DNP=50 nm, g0=10nm and g1=30nm, respectively; (h) the measured transmission of the glass, Samlple3 and Sample4; Inset is the sketch of the light transmission and reflection from the AAO samples*

www.manaraa.com

3.4 Summary

The mechanisms and characteristics of the AAO thin film-enabled fluorescence enhancement have been studied. While the nanopore size and porosity have effects on the fluorescence enhancement, it has been found that fluorescence enhancement is probably mainly attributed by the Al NPs embedded in the AAO thin film. This has been verified qualitatively by calculating the E-field distribution based on a simple AAO thin film model. The characteristics of fluorescence enhancement enabled by AAO thin film have also been studied. First, the fluorescence enhancement is gap-dependent. When the gap between the fluorophores and AAO thin film surface increases, the enhancement drops significantly. The largest enhancement occurs when the fluorophores are directly deposited on AAO surface. Second, the excitation wavelength is another impact factor on the enhancement. For these AAO samples, scattering light intensity of the bare AAO micropatterns under blue light excitation (475 nm) for FSS is larger than that of green light excitation (550 nm) for PI. As a result, the fluorescence intensity of FSS is larger than that of PI when they are coated on AAO thin film.

References

[1] A. Emili, et al, Nat. Biotechnol. vol. 18, no. 4, 393- 397 (2000).

[2] D. Giljohann, et al, Nature, vol. 462, no. 7272, 461-464 (2009).

[3] C. Geddes, et al, J. Fluoresc. vol.12, 121-129 (2002).

[4] G. Lu, et al, ACS Nano, vol. 6, no. 2, 1438-1448 (2012).

[5] L. Zhou, et al, Anal. Chem. vol. 84, no.10, 4489-4495 (2012).

[6] E. Goldys, et al, J. Am. Chem. Soc. vol.129, no. 40, 12117-12122 (2007).

[7] Y. Hung, et al, Opt. Express vol.14, no. 22, 10825-10830 (2006).

www.manaraa.com

[8] V. Adalsteinsson, et al, Anal. Chem. vol. 80, 6594-6601 (2008).

[9] X. Li, et al, Optics Express, vol. 20, no. 19, 21272-21277 (2012).

[10] X. Li, et al, Reviews in Nanoscience and Nanotechnology 3, no. 3 161-176 (2014).

[11] X. Che, et al, Biosensors and Bioelectronics, vol.72, 255-260 (2015).

[12] X. Li, et al, Langmuir, vol. 29, no. 7, 2439-2445 (2013).

[13] X. Che, et al, In Nanotechnology (IEEE-NANO), 2017 IEEE 17th International Conference on, pp. 1039-1042, 2017.

[14] X. Li, et al, *Biomedical microdevices* 16, no. 5, 771-777 (2014).

[15] Y. He, *Journal of biomedical nanotechnology* 10, no. 5, 767-774 (2014).

[16] H. Masuda and K. Fukuda, Science 268, 1466–1468 (1995).

[17] ComSol: https://www.comsol.com/

[18] N. Ganesh, et al, Nature Nanotechnology 2, no. 8, 515-520 (2007).

[19] M. Bauch, et al, Plasmonics 9, no. 4, 781-799 (2014).

[20] M. Born, and E. Wolf, *Principal of Optics* (John Wiley & Sons, Inc., 2000)

[21] E. Le Moal, et al, Biophysical journal 92, no. 6 (2007): 2150-2161.

[22] S. Ding, et al, Nature Reviews Materials 1, 16021(2016).

[23] M. Knight, et al, ACS nano 8, no. 1, 834-840 (2013).

[24] I. H. Malitson, et al, J. Opt. Soc. Am. 62, 1405 (1972)

[25] M. J. Dodge, "Refractive Index" in Handbook of Laser Science and Technology, Volume IV, Optical Materials: Part 2, CRC Press, Boca Raton, 1986, p. 30

[26] K. M. McPeak, et al, ACS Photonics 2, 326-333 (2015)

[27] E. Koushki, et al, Thin Solid Films, 592, 81-87 (2015)

[28] P. Mathias, et al, Analytical Chemistry, no. 23, 9013-9020 (2008)

www.manaraa.com

CHAPTER 4. A MOLECULAR BEACON BIOSENSOR BASED ON THE NANOSTRUCTURED ALUMINUM OXIDE SURFACE

Modified from a journal paper published in *Biosensors and Bioelectronics*

Xiangchen Che, Yuan He, Haocheng Yin, and Long Que

Abstract

A new class of molecular beacon biosensors based on the nanostructured aluminum oxide or anodic aluminum oxide (AAO) surface is reported. In this type of sensor, the AAO surface is used to enhance the fluorescent signals of the fluorophore-labelled hairpin DNA. When a target DNA with a complementary sequence to that of the hairpin DNA is applied on the sensor, the fluorophores are forced to move away from the AAO surface due to the hybridization between the hairpin DNA and the target DNA, resulting in the significant decrease of the fluorescent signals. The observed signal reduction is sufficient to achieve a demonstrated detection limit of 10 nM, which could be further improved by optimizing the AAO surface. The control experiments have also demonstrated that the bioassay used in the experiments has excellent specificity and selectivity, indicating the great promise of this type of sensor for diagnostic applications. Since the arrayed AAO micropatterns can be fabricated on a single chip in a cost-effective manner, the arrayed sensors could provide an ideal technical-platform for studying fundamental biological process and monitoring disease biomarkers.

4.1 Background

Deoxyribonucleic acid (DNA) is a molecule that contains the genetic information for all known living organisms and many viruses (Jones and Baylin, 2002; Lockhart et al., 2000). Hence, DNA sensor is a critical platform for understanding the fundamental biological process and unrevealing

www.manaraa.com

the causes of diseases. DNA sensors based on different operational principles have been developed over the past decades. Examples include optical, electrochemical, magnetic, and quartz crystal microbalance (QCM) based DNA sensors (Nelson et al., 2001; Drummond et al., 2003; Kouassi and Irudayaraj, 2006; Wang et al., 2012). For optical DNA sensors, a variety of optical methods such as the evanescent optical field, resonant rings and optical grating coupler have been used for detecting DNA (Nelson et al., 2001; Sun and Fan, 2011; Liu and Tan, 1999). For instance, surface Plasmon resonance (SPR) technique has been proved to be a viable technical platform for DNA detection (Nelson et al., 2001). Electrochemical method offers another approach for DNA sensing. Electrochemical DNA sensors provide a cost-effective technical platform for the detection of DNA sequences or genes associated with the human disease with high sensitivity and selectivity. There are a variety of approaches for electrochemical detection such as direct electrochemistry of DNA, electrochemistry at polymer-modified electrodes, just to name a few (Drummond et al., 2003). Some efforts have also been devoted to using magnetic nanoparticles for DNA detection. Single strands of oligonucleotides can be effectively immobilized onto amino- and carboxylate-functionalized magnetic nanoparticles or gold-coated magnetic nanoparticles using the streptavidin-biotin interaction. Experiments have demonstrated that the gold-coated magnetic nanoparticles are ideal DNA sensors (Kouassi and Irudayaraj, 2006; Fan et al., 2005). For the QCM-based DNA sensor, when the target DNA binds to the probe DNA on the QCM, the mass of the biomolecules changes, resulting in a shift of the resonant frequency of the QCM (Wang et al., 2012).

One of the promising optical DNA sensors is to use molecular beacons (MBs) for sensing due to their high sensitivity, specificity and reliability (Du et al., 2003; Xiao et al., 2006; Sun and Fan, 2012; Fang et al., 1999; Peng et al., 2009). Usually, the MB is a hairpin DNA functionalized at

www.manaraa.com

one end with a fluorophore and at the other end with a quenching agent or using a metal-coated substrate to quench the fluorescent signals. Without the target DNA, the quencher is in close proximity to the fluorophore, no fluorescent signal is generated. By adding a complementary target DNA, the loop of hairpin DNA is unfolded, the fluorophore moves away from the quencher, resulting in fluorescent signal generation. To our knowledge, most of the reported MB sensors employ a quenching agent or the metal-coated substrate as fluorescent quencher. Herein, we investigate if a nanostructured aluminum oxide or anodic aluminum oxide (AAO) surface itself could be used as a fluorescent enhancer, thereby developing a new type of MB biosensor.

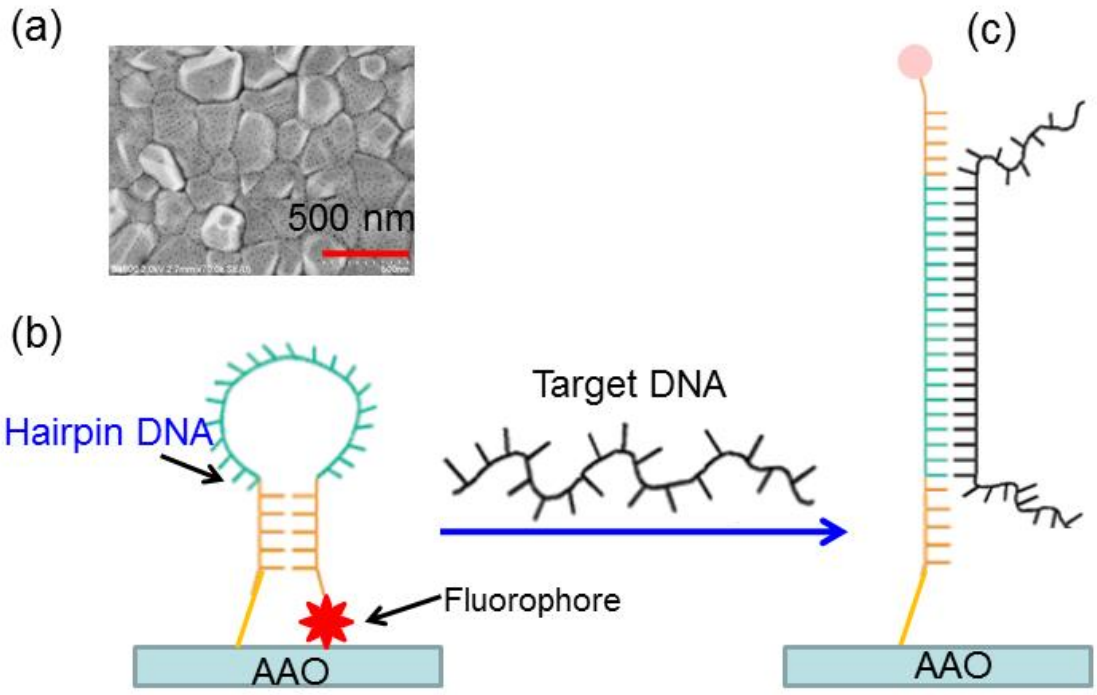

Figure 4.1 *(a) SEM image of an AAO surface showing nanoscale domains; (b-c) Operational principle of the AAO surface-based molecular beacon biosensor*

For the past, using the unique optical inference fringes of the AAO thin film, AAO thin film-based interferometry sensors have been developed and mainly used for label-free biodetection (Zhang et al., 2010; Zhang et al., 2011; Zhang et al., 2012; He et al., 2014). Recently it has been found that the AAO surface can also significantly enhance the fluorescent signals when the

www.manaraa.com

fluorophores are in close proximity to its surface (Li et al., 2012; Li et al., 2013; Li and Que, 2014). It has been found that the enhancement factor is in the range of two to three orders of magnitude compared to the glass surface when the fluorophores are directly attached to the AAO surface (Li et al., 2012; Li et al., 2013; Li and Que, 2014; Yin et al., 2014). Different from metal-enhanced fluorescence (MEF), which requires a spacer between the metal surface and fluorophores to avoid quenching effect, the AAO surface offers the maximum fluorescence enhancement when the fluorophores directly contact with its surface, but the enhancement reduces dramatically when the gap between the AAO surface and the fluorophores increases. The enhancement mechanism of the AAO surface is not totally understood and thus requires further studies. However, based on the previous research, this enhancement probably results from the following main reasons. First, optical scattering of the AAO surface may play a very important role in the fluorescence enhancement. The surface scattering effects of the AAO surface cause the redistribution of the electromagnetic fields with high surface intensities, resulting in the enhanced fluorescence (Fujii et al., 2004; Zhang et al., 2012; Ganesh et al., 2007). Second, the fluorescence enhancement might also result from the evanescent electrical field from the surface of the nanoscale AAO grains (**Figure 4.1a**), similar to other reported metal oxide nanoscale materials (Dorfman et al., 2006; Zhao et al., 2008; Gu et al., 2008). This assumption has been validated by evaluating the effect on the fluorescent signals from the gap between the AAO surface and the fluorophores by coating a layer of poly (methyl methacrylate) (PMMA) between the AAO surface and the fluorophores (Li, 2014). It has been found that the significant enhancement of the fluorescence occurs only in the range of one hundred nanometers from the AAO surface. At and beyond 100 nm from the AAO surface, the fluorescence enhancement becomes significantly weak. This property can be exploited for a new type of MB biosensor.

www.manaraa.com

The principle of the new MB biosensor is illustrated in **Figure 4.1b-c**. In this case, a hairpin DNA with one end attached with a fluorophore emits a strong fluorescent signal when it is immobilized on the AAO surface and its loop is closed (**Figure 4.1b**). The fluorescent signal reduces dramatically when the loop is open if it is hybridized with a complementary target DNA (**Figure 4.1c**). The sequence of "on" and "off" of fluorescent signals of this type of MB biosensor is just opposite from that of other previously reported MB sensors (Du et al., 2003; Xiao et al., 2006; Sun and Fan, 2012; Fang et al., 1999; Peng et al., 2009), which might open a new avenue for fluorescent-based bioassay. Compared to the noble metal (i.e., Au or Ag) nanoparticles or nanostructures based MB biosensors (Du et al., 2003; Xiao et al., 2006; Sun and Fan, 2012; Fang et al., 1999; Peng et al., 2009), the AAO based MB biosensor offers at least the following advantages: (1) It is simple and inexpensive to prepare AAO surface using the anodization process with high uniformity and repeatability; (2) the material (aluminium) for fabricating the MB sensors is much cheaper than Au or Ag-based MB sensors; and (3) using the lithography-based fabrication process, hundreds or thousands of AAO based microscale MB biosensors can be fabricated in an efficient manner for high throughput application.

Table 4.1 *DNA sequences for the experiments*

DNA	**Sequence**
Hairpin DNA (H1 DNA)	5'-/5AmMC6/ACA CGC TCA TCA TAA CCT TCA GCA AGC TTT AAC TCA TAG TGA GCG TGT/3TYE563/-3'
Target DNA (T1 DNA)	5'-ACG CTC ACT AGT TAA AGC TTG CTG AAG GTT ATG A -3'
Control DNA (T2 DNA)	5'- TAT GGA GGT GTA GAA GGT GTT ATC ATC ATC ATT-3'

www.manaraa.com

4.2 Methods and materials

Fabrication of the anodic aluminum oxide micropatterns on glass substrate:

An ITO glass substrate is first cleaned by DI water, acetone, ethanol, and then DI water for 20 minutes with each solution. Then 2μm aluminum is deposited on the substrate with 10 nm Ti as an adhesion layer by E-beam evaporation. The measured surface roughness of the Al thin film is in the range of 6-12nm, which is smooth enough for carrying out the anodization process. Then, one-step anodization process (in 0.3 M oxalic acid) is performed to form anodic aluminum oxide. After this step, the AAO micropatterns are fabricated using the process developed in (Li et al., 2014) using standard optical lithography and wet etching process.

Chemicals and materials:

The reagents (DNA samples) are custom-synthesized at Integrated DNA Technologies, Inc. Their sequences are summarized in **Table 4.1**. The reagents include three types of DNA powers with different sequences. Hairpin DNA (H1 DNA) (with 5' amino-terminated) has a fluorophore at its 3’ end. Target DNA (T1 DNA) has some fragments, which have a complementary sequence to H1 DNA. And control DNA (T2 DNA) is not complementary to H1 DNA. The solution used to dissolve the DNA powder is Buffer PE (Qiagen: Sample & Assay Technologies, Inc). The H1 DNA is diluted using Buffer PE into 1 μM. T1 DNA are diluted using Buffer PE into different concentrations including 1 μM, 0.5 μM, 0.1 μM, 0.05 μM, 0.02 μM, and 0.01 μM. Similarly, T2 DNA is diluted into 1 μM and 0.5 μM. Chemicals for surface treatment of AAO include hydrogen peroxide (Sigma-Aldrich, Inc) and 3-(Triethoxysilyl) propyl isocyanate solution(assay 95%, Sigma-Aldrich, Inc).

www.manaraa.com

Experiment procedure:

The surface treatment of the AAO nanostructures is carried out to make sure the H1 DNA can be tightly bound to their surface. The procedure is illustrated in **Figure 4.2**. First, the AAO surface is dipped into H_2O_2 solution (70%) for 20 minutes and then dipped into 3-(Triethoxysilyl)propylisocyanate solution for 20-30 minutes. After the surface treatment, a drop of H1 DNA solution of a concentration of 1 μM is applied on the AAO surface, allowing the DNA hairpin's 5'-end to be bound to AAO's surface for 20 minutes. After that, the AAO sample is rinsed by hot water (90 °C or higher) to remove the unbound H1 DNA, followed by adding Buffer PE to keep the AAO surface in wet condition. In the following 15 minutes, the fluorescent intensity and images of the AAO sample are taken every 5 minutes to ensure the H1 DNA to be immobilized on AAO surface completely, resulting in a maximized fluorescent intensity. Then T1 DNA solution of a concentration of 1 μM is added, followed by 20-minute incubation to allow the hairpin to open. During this period of time, the fluorescent images are taken every 5 minutes. In the whole experimental procedure, the AAO sample is kept in wet condition by adding buffer PE on the sample in a darkroom. The same procedure is repeated for T1 DNA with different concentrations of 0.5 μM, 0.1 μM, 0.05 μM, 0.02 μM, and 0.01 μM. And for the control experiments, the concentrations of T2 DNA are 1 μM and 0.5 μM.

Fluorescence detection, imaging, and analysis:

All the fluorescent images have been taken using a fluorescence microscope (Olympus, Inc), which has three filter sets: DAPI (excitation filter: 330 nm - 385 nm; barrier filter: 420 nm - 460 nm); FITC (excitation filter: 475-490 nm; barrier filter: 500-540 nm); and TRITC (excitation filter: 545-565 nm; barrier filter: 580-620 nm). Unless otherwise mentioned, the fluorescent images have

www.manaraa.com

been obtained using a TRITC filter set. In this paper, the fluorescence intensity is determined by analyzing the fluorescence images by using imaging process toolbox in MatLab. A MatLab program has been written to read the files of fluorescence images and to find the fluorescent intensity (Li et al., 2012). All the images have been taken under fixed exposure time and energy.

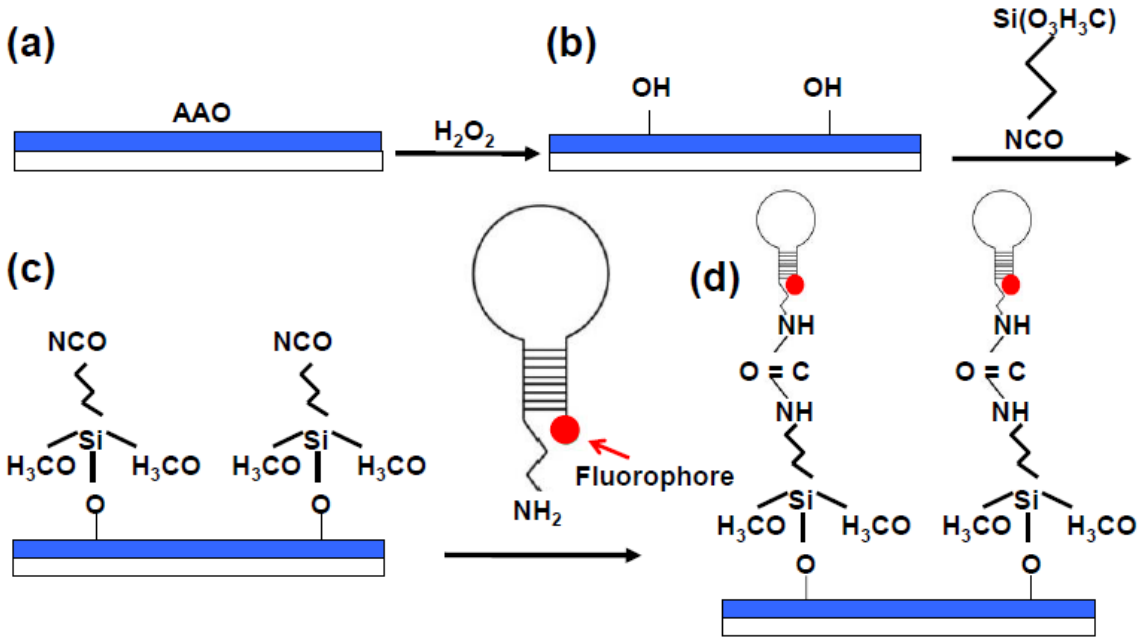

Figure 4.2 *Schematic of the protocol for immobilizing the hairpin DNA on the AAO surface: (a-b) AAO surface is dipped into H2O2 solution for 20 minutes; (c) Then AAO surface is dipped into 3-(Triethoxysilyl)propylisocyanate solution for 20-30 minutes; (d) a drop of H1 DNA is applied and incubated for 20 minutes to immobilize H1 DNA, followed by rinsing with hot water to remove the unbound H1 DNA, and then adding Buffer PE to keep the AAO surface in wet condition, thereafter ready for applying target DNA*

4.3 Results and discussion

The optical micrograph of the AAO gear-micropatterns and the SEM image of the AAO are given in **Figure 4.3(a-b)**. As shown, the nanoscale-domain of the AAO is clearly visible, resulting from the nanoscale grains of the Al in a thin film. The nanopores inside each domain are also clearly visible. These micropatterns on the glass substrate are used as MB biosensors.

www.manaraa.com

As shown in **Figure 4.3(c)**, the fluorescent signals of H1 DNA of a concentration of 1 μM on the AAO gear-micropatterns are much larger than those on the glass substrate due to the significant fluorescent enhancement by the AAO surface, which are two to three orders of magnitude large over that on the glass substrate. It should be noted that the H1 DNA attached to glass also emits fluorescent signals, but the fluorescent signals appear much lower than those on AAO micropatterns.

However, as shown in **Figure 4.3(d)**, the fluorescent signals decrease dramatically after the T1 DNA of a concentration of 1 μM, with significant parts of a complementary sequence to H1 DNA, is applied on the sample in ten minutes, indicating the hybridization between H1 DNA and T1 DNA. The loop of H1 DNA is thus forced to open. The fluorophores attached to the end of the H1 DNA move away from the AAO surface. As a result, the enhancement due to the AAO surface is exponentially reduced, and consequently, the fluorescent signals from AAO micropatterns drop dramatically.

In order to determine the detection limit of the AAO-based fluorescent MB sensor, different concentrations of T1 DNA have been applied on the same AAO-based sensor (prior to applying T1 DNA, a drop of H1 DNA solution of a concentration of 1 μM has been immobilized on AAO surface), and the corresponding fluorescent intensity has been measured as shown in **Figure 4.3(e-f)**. It has been found that the fluorescent intensity decreases with the increasing concentration of T1 DNA, suggesting that the increased amount of H1 DNA is bound with T1 DNA. Therefore, the increased amount of H1 DNA is forced to open their loop. As a result, the increased amounts of fluorophores are moved away from the AAO surface, thus the fluorescent intensity also further decreases. Herein, the detection limit is defined as the change of the fluorescent intensity before and after applying T1 DNA is at least 30%. As shown in **Figure 4.3(f)**, the DL is 10 nM, which is

www.manaraa.com

comparable to the previously reported MB sensor based on the Au-coated or Ag-coated surface (Du et al., 2003; Peng et al., 2009).

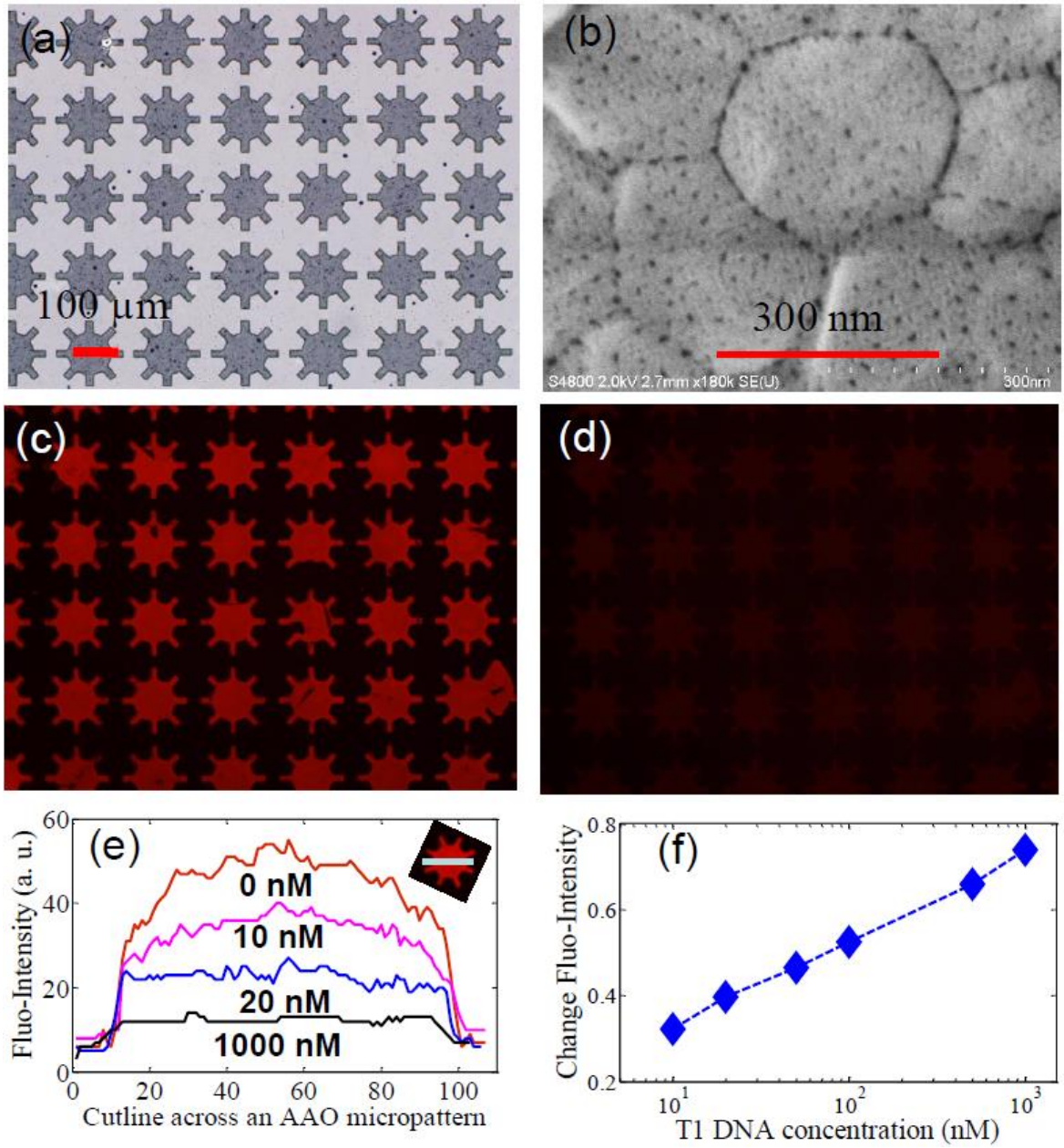

Figure 4.3 *(a) Optical micrograph showing the fabricated AAO gear-micropatterns; (b) SEM image showing the surface of the AAO gear-micropatterns; (c) Fluorescent images of the AAO surface immobilized with hairpin DNA; (d) Fluorescent images after T1 DNA applied on the AAO surface in (c); (e) Fluorescence intensity along a cutline across an AAO micropattern with different concentrations of the applied target DNA (T1 DNA). Insert showing the cutline across an AAO micropattern; (f) Fluorescence intensity change for different concentrations of the applied target DNA (T1 DNA).*

www.manaraa.com

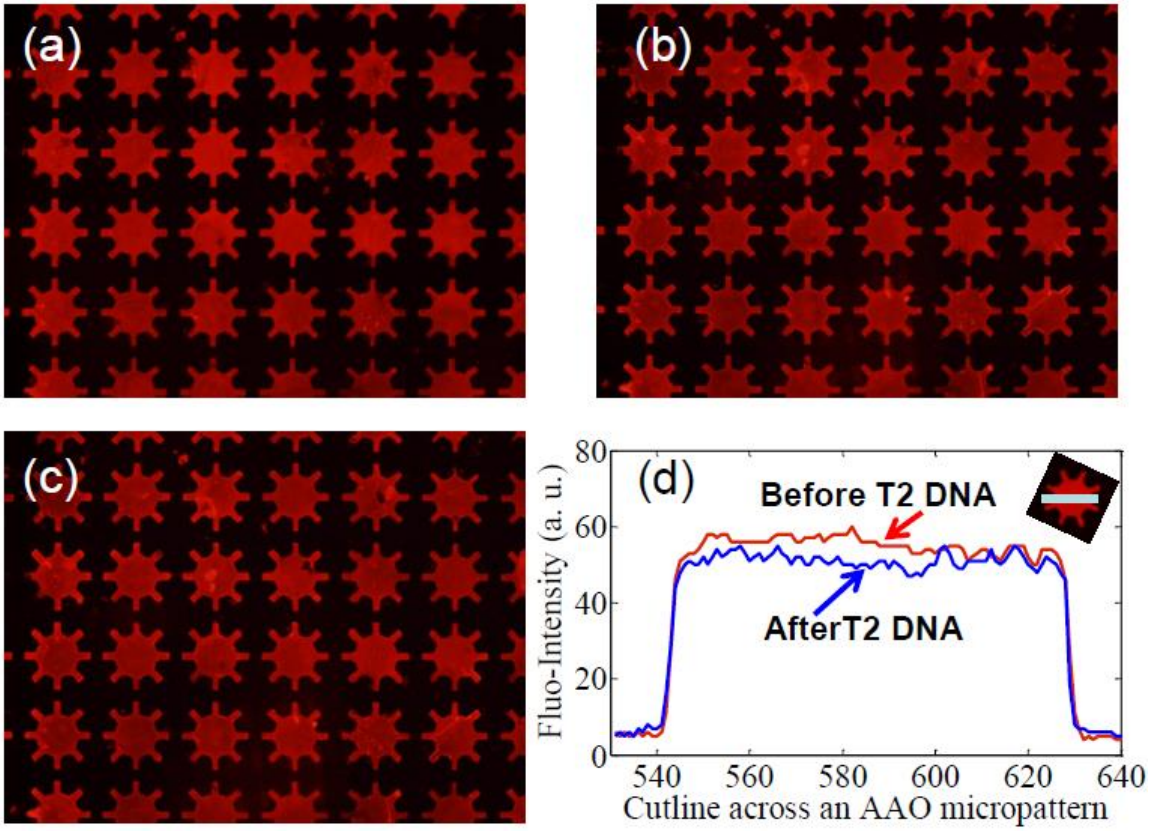

Figure 4.4 *Specificity and selectivity experiments: (a) Fluorescence image after applying hairpin DNA; (b) Fluorescence image after applying 0.5 µM T2 DNA for 2 hours; (c) Fluorescence image after applying 1µM T2 DNA for 2 hours; (d) Fluorescence intensity along a cutline across an AAO micropattern before and after appling 1 µM T2 DNA for 2 hours.*

For a diagnostic device or biosensor, besides its sensitivity, another critical property is the binding specificity such as DNA sequence selectivity. To this end, the control experiments have been carried out to demonstrate the specificity and selectivity of the bioassay. In these experiments, T2 DNA (salmon sperm DNA) is used. Its sequence is not complementary to that of H1 DNA. In this case, the incubation time after applying T2 DNA at concentrations of 0.5 µM and then 1 µM in sequence is over 2 hours, respectively. The fluorescent images have been taken before and after rinsing the samples rigorously. The fluorescent images show very small changes as shown in **Figure 4.4 (a-c)** for both concentrations. The fluorescent intensities before and after applying T2 DNA are given in **Figure 4.4(d)**. The average change in fluorescent intensity is typically only

www.manaraa.com

~6%. In contrast, as shown in **Figure 4.3**, for the concentration of 1 μM of T1 DNA, the decrease of the fluorescent intensity is closed to 80%. These measurements suggest that T1 DNA immobilized on the AAO surface has its ability to bind complementary DNA sequence selectively. The slight changes (~6%) in the fluorescent signals in the control experiments may result from somewhat binding between the H1 DNA with the T2 DNA (Du et al., 2003; BLAST, 2015). All these experiments confirm the excellent specificity and selectivity between H1 DNA and T1 DNA of this type of MB biosensor.

4.4 Conclusions

In summary, based on the fluorescence enhancement by the AAO surface, we have demonstrated that fluorophore-tagged hairpin DNA attached to the AAO surface can function as highly sensitive and selective sensors for detecting oligonucleotides. Specifically, for a hairpin DNA sequence (H1 DNA), the binding with a complementary DNA sequence (T1 DNA) results in the decrease in fluorescent signals close to 80%. In contrast, for the nonspecific sequence (T2 DNA), the average change in fluorescent signals is only about 6%. Currently, the detection limit (LD) of the DNA sensors is about 10 nM. The DL could be further lowered down by optimizing the optical properties (e.g., fluorescence enhancement) of the AAO surface. Recent experiments in our lab have found the fluorescent enhancement can be improved by tuning the nanopore size among other dimensions. Experiments have also demonstrated the high specificity and selectivity between the hairpin DNA and target DNA used in the biodetection, suggesting the great promise for the detection of DNA biomarkers at trace levels in biofluids. Finally, due to the simplicity and cost-effectiveness for fabricating hundreds and thousands of arrayed AAO micropatterns on a single chip, this microarray format platform offers great potential for highly multiplexed and sensitive biodetection for the diagnosis of various diseases.

www.manaraa.com

References

[1] BLAST 2015: http://blast.ncbi.nlm.nih.gov/Blast.cgi.

[2] Dorfman, A., Kumar, N., Hahm, J., 2006. Langmuir, 22 (11), 4890-4895.

[3] Drummond, T., Hill, M., Barton, J., 2003. Nature Biotechnology, 21(10), 1193-1199.

[4] Du, H., Disney, D., Miller, B., Krauss, T., 2003. J. Am. Chem. Soc. 125, 4012-4013.

[5] Fan, A., Lau, C., Lu, J., 2005. Anal. Chem. 77, 3238-3242.

[6] Fang, X., Liu, X., Schuster, S., Tan, W., 1999. J. Am. Chem. Soc. 121, 2921-2922.

[7] Fujii, T., Gao, Y., Sharma, R., Hu, E., DenBaars, S., Nakamura, S., 2004. Appl. Phys. Lett. 84 (6), 855-857.

[8] Ganesh, N., Zhang, W., Mathias, P., Chow, E., Soares, J., Malyarchuk, V., Smith, A., Cunningham, B., 2007. Nat. Nanotechnol. 2 (8), 515-520.

[9] Gu, C., Huang, J., Ni, N., Li, M., Liu, J., 2008. J. Phys. D: Appl. Phys. 41 (17), 175103.

[10] He, Y., Li, X., Que, L., 2014. Journal of Biomedical Nanotechnology, 10 (5), 767-774.

[11] Jones, P., Baylin, S., 2002. Nat. Rev. Genet. 3, 415-428.

[12] Kouassi, G., Irudayaraj, J., 2006. Anal. Chem. 78, 3234-3241.

[13] Li, X., Nanostructured aluminum oxide: Enhanced fluorescence imaging and sensing. PhD Dissertation, 2014.

[14] Li, X., He, Y., Zhang, T., Que, L., 2012. Optics Express, 20 (19), 21272-21277.

[15] Li, X., He, Y., Que, L., 2013. Langmuir, 29 (7), 2439-2445.

[16] Li, X., Que, L., 2014. Reviews in Nanoscience and Nanotechnology, 3 (3), 161-176.

[17] Liu, X., Tan, W., 1999. Anal. Chem. 71, 5054-5059.

[18] Lockhart, D., Winzeler, E., 2000. Nature, 405, 827-836.

[19] Nelson, B., Grimsrud, E., Liles, M., Goodman, R., Com, R., 2001. Anal. Chem. 73, 1-7.

[20] Peng, H., Strohsahl, C., Leach, K., Krauss, T., Miller, B., 2009. ACS NANO, 3(8), 2265-2273.

[21] Sun, Y., Fan, X., 2011. Analytical and Bioanalytical Chemistry, 339 (1), 205-211.

www.manaraa.com

[22] Sun, Y., Fan, X., 2012. Angew. Chem. Int. Ed. 51, 1236-1239.

[23] Wang, D., Tang, W., Wu, X., Wang, X., Chen, G., Chen, Q., Li, N., Liu, F., 2012, Anal. Chem. 84, 7008-7014.

[24] Xiao, Y., Lubin, A., Baker, B., Plaxco, K., Heeger, A., 2006. Proceedings of the National Academy of Sciences of the United States of America 103(45), 16677-16680.

[25] Yin, H., Li, X., Que, L., 2014. Microelectronic Engineering, 128 (5), 66–70.

[26] Zhang, T., Gong, Z., Giorno, R., Que, L., 2010. Opt. Express, 18 (19), 20282-20288.

[27] Zhang, T., Pathak, P., Karandikar, S., Giorno, R., Que, L., 2011. Biosensors and Bioelectronics, 30, 128-132.

[28] Zhang, T., He, Y., Wei, J., Que, L., 2012. Biosensors and Bioelectronics, 38, 382-388.

[29] Zhang, Z., Zheng, H., Dong, J., Yan, X., Sun, Y., Xu, H., 2012. Sci China-Phys Mech Astron. 55 (5), 767–771.

[30] Zhao, J., Wu, L., Zhi, J., 2008. J. Mater. Chem. 18 (21), 2459-2465.

www.manaraa.com

CHAPTER 5. ON-CHIP MONITORING OF GROWTH FACTOR SECRETION BY PANCREATIC CANCER AND STELLATE CELLS BASED ON NANOSTRUCTURED ALUMINUM OXIDE

Modified from a conference paper published to *IEEE NANO Conference 2017*

Xiangchen Che, Jacob Nuhn, Ian Schneider, and Long Que

Abstract

A nanoporous anodic aluminum (Nano-AAO) thin film-enabled fluorescence chip to monitor the cell secretion is reported in this paper. The Nano-AAO thin film, which can dramatically enhance the fluorescence signals compared to coverslip glass, serves as the fluorescence sensor. It has been found that concentrations as low as 10ng/ml transforming growth factor β1 (TGF-β1) can be readily detected in buffer. TGF-β1 has also been detected successfully in conditioned cell media. Specifically, TGF-β1 secreted directly by pancreatic stellate (iTAF) cells only and by co-cultures of pancreatic cancer (capan-1) and pancreatic stellate (iTAF) cells have also been detected by the Nano-AAO thin film sensors using a sandwich assay. It has been found that the concertation of TGF- β1 in media conditioned by iTAF cells alone for 48 hrs. is ~17.6 ng/ml. No significant concentration of TGF- β1 was found in media conditioned by capan-1 alone. However, when in co-culture iTAF and Capan-1 cells generated media concentrations of ~321.2 ng/ml, verifying that pancreatic cancer and stellate cells communicate resulting in increased secretion by iTAFs under co-culture conditions.

5.1 Introduction

Secreted extracellular cues allow cells to communicate. This communication drives differentiation, proliferation, and migration, and results in organization of unique biological

www.manaraa.com

systems with physiological functions (Lander, 2013; Stastna and Van Eyk, 2012). Secreted molecules carry information in the ligand-receptor interactions they stimulate as well as in their spatiotemporal concentration distributions. Diffusion, binding and turnover of the secreted molecules can confine their presence within a local area. Furthermore, the responding cells can be of various distances away from signaling cells and can spatially express receptors, resulting in unique responses. Hence, it is critical to creating a technical platform to sense cellular communication at the subcellular level. Many secreted proteins are important direct functional mediators of intracellular signaling and act by initiating signaling through cell surface receptors (Gnecchi et al., 2008). Other secreted proteins work indirectly by altering the extracellular matrix (ECM) which affects various cellular processes (Bonnans et al., 2014; Mouw et al., 2014). Cell communication through secretion is important in several situations such as during cancer metastasis. Cancer and stromal cells communicate by secreting growth factors or ECM modifying proteins. Growth factors often enhance migration by activating intracellular signaling related to motility, and ECM modifying proteins alter the ECM structure or stiffness, both of which result in cancer invasion and metastasis (Guo and Giancotti, 2004; Gupta and Massagué, 2006). For instance, transforming growth factor-β1 (TGF-β1) is thought to be secreted by pancreatic cancer cells, particularly those that are exposed to normal cells found in the tumor microenvironment including pancreatic stellate cells resulting in alterations in the extracellular matrix leading to pancreatic cancer fibrosis and tumor progression (Wehr, A.Y., et al., 2011; Laklai, H., et al., 2016).

In the past years, quite a few methods have been reported to monitor the biomolecules including growth factors secreted by cells (Domaille et al., 2008; Gee et al., 2002; Luchansky and Bailey, 2010; Shirasaki et al., 2014; Son et al., 2017; Wang et al., 2011; Han Q et al., 2010; Lu Y et al, 2013;). For instance, an integrated microsystem, composed of a microfluidic device and a

www.manaraa.com

fluorescent microbead-based assay for detecting the hepatocyte growth factor (HGF) and the transforming growth factor (TGF-β1) secreted by primary hepatocytes, has been demonstrated (Son et al., 2017). Another assay platform for real-time imaging of protein secretion at single-cell resolution enabled by total internal reflection fluorescence (TIRF) microscopy has been reported (Shirasaki et al., 2014). Real-time secretion imaging allows the successful detection of the heterogeneous onset time of nonclassical IL-1b secretion from monocytes after external stimulation. An *in-situ* immunoassay based on optical enhancement of a nano-plasmonic-resonator array has been reported (Wang et al., 2011). This technology can achieve submicrometer resolution quantitative mapping of endogenous cytokine secretion.

Herein, a new enhanced-fluorescence sensing platform, enabled by the nanostructured aluminum oxide (Nano-AAO) thin film, for detecting the transforming growth factor is reported. The platform offers a new avenue for in situ high-resolution extracellular sensing to monitor transforming growth factor β1 (TGF-β1) secreted by pancreatic cancer (capan-1) and stellate cells (iTAF) in both mono- and co-cultures.

The schematic of the sensor chip is shown in **Figure 5.1a**. Inside the chip, there are a number of nanostructured aluminum oxide or nanoporous anodic aluminum oxide (Nano-AAO) thin film micropatterns (Nano-AAO micropatterns) surrounded by a polydimethylsiloxane (PDMS) well. The nano-AAO micropatterns, due to their large fluorescence enhancement capability (Che et al. 2018, Li et al. 2013, Che et al. 2015) in comparison with coverslip glass, are used as fluorescence sensors. The surface of the sensor is functionalized with TGF-β1 capture antibody (**Figure 5.1a**). When TGF-β1 is secreted by iTAF cells, it binds to its capture antibody. A biotinylated detection antibody along with a fluorescently labeled streptavidin binds TGF-β1, resulting in fluorescence signals that can be detected.

www.manaraa.com

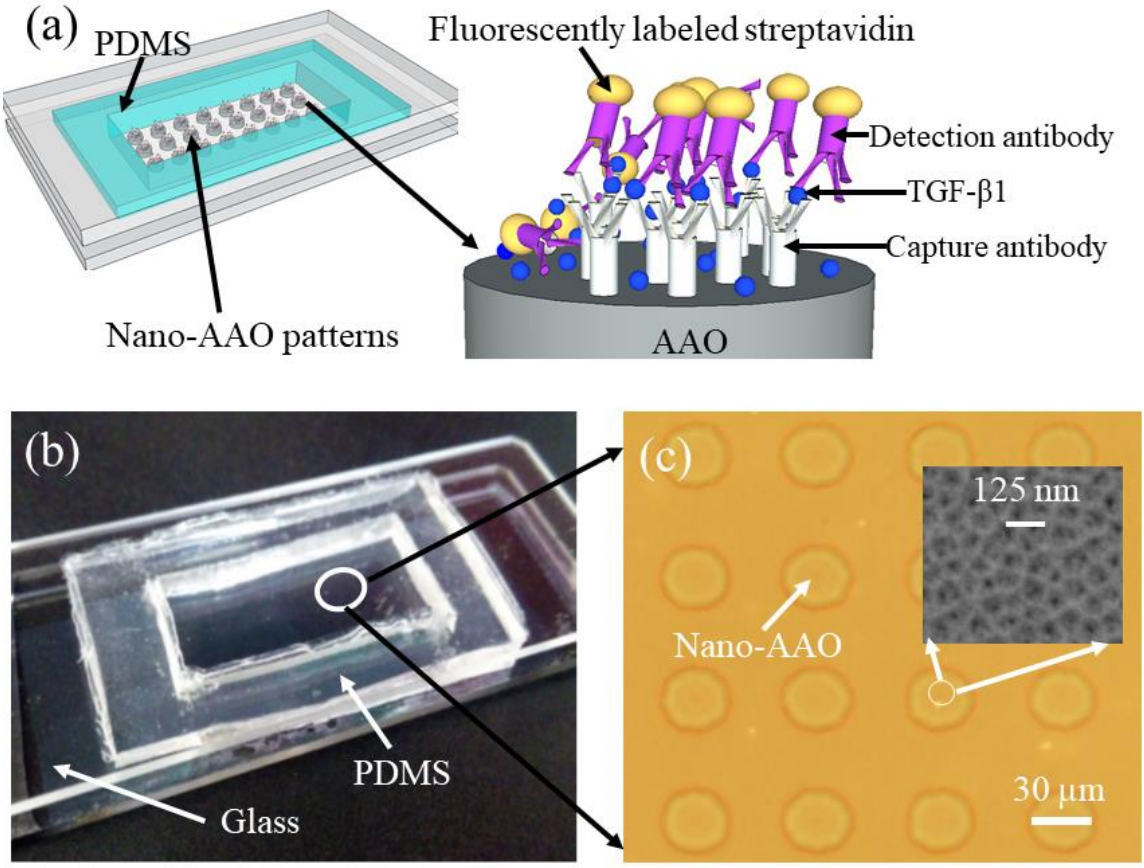

Figure 5.1 *(a) Sketch showing fluorescence sensor chip with arrayed Nano-AAO micropatterns inside a PDMS well, and the surface functionalized with chemicals as an sandwich assay for detecting TGF-β1; (b) Optical photo of a fabricated sensor chip; (b) Close-up showing the Nano-AAO micropatterns; Inset is the SEM image of the nanopore thin film.*

5.2 Materials and methods

Chemicals and materials:

3-aminopropyltriethoxysilane (APTES) and glutaraldehyde (Grade I, 70 wt% in H2O) are purchased from Sigma-Aldrich. Monoclonal Antibody (eBio16TFB), purified TGF-β1 and fluorescently labeled streptavidin are all purchased from ThermoFisher Scientific. LEAF™ Purified anti-human/mouse TGF-β1 Antibody is purchased from Biolegend. Cell tracker Red CMTPX dye purchased from ThermoFisher Scientific and Calcein AM purchased from Sigma-

www.manaraa.com

Aldrich are used to monitor the cell viability. Fluorescein sodium salt (FSS) purchased from Sigma-Aldrich is used to compare the fluorescence sensitivity on coverslip glass and nano-AAO thin film.

Procedure for secretion of TGF-β1 from cells:

Conditioned media is prepared by growing pancreatic cancer (capan-1) or stellate (iTAF) cells in mono- or co-cultures to 60% confluency. The total cell number in co-cultures is equal to that of mono-cultures. After cultures were grown to 60% confluency, the media was removed, and 2 ml of fresh Dulbecco's Modified Eagles Medium (DMEM) (Sigma Aldrich, St. Louis, MO, USA) with 10% fetal bovine serum (FBS) (Gibco, Grand Island, NY, USA), 2% glutamax (Gibco) and 1% penicillin/streptomycin (Gibco) was added, and culture was placed back into a 37°C incubator. After 48 hours the media is removed, placed in a 15 ml conical tube, and clarified at 3000 × g for five minutes to remove cellular debris. The media is transferred 1.5 ml Eppendorf tubes and flash frozen with liquid nitrogen and stored in a -4°C freezer until ready for use.

Fabrication of the sensor chip:

(1) Nano-AAO thin film fabrication process: a layer of Al with high purity (99.99%) is deposited by e-beam evaporation on a rigorously cleaned glass substrate. Then a standard anodization process (He et al., 2014) is used to convert Al thin film into Nano-AAO thin film.

(2) Sensor chip fabrication process: The development of the sensors starts with fabricating Nano-AAO micropatterns on glass substrate. The process flow is the same as that reported before (Yin et al., 2014). Briefly, a layer of Al with high purity (99.99%) is deposited on a rigorously

www.manaraa.com

cleaned glass substrate, followed by an anodization process to convert Al into Nano-AAO. Then the Nano-AAO micropatterns are fabricated by optical lithography and time-controlled wet etching process (Yin et al., 2014). Next, a 2-inch (Length) × 0.8-inch (Width) × 0.4-inch (Height) polydimethylsiloxane (PDMS) film with a hole of 1.5-inch × 0.5-inch is cut and bonded on the chip surface after oxygen plasma treatment. A PDMS well with a size of 1.5-inch × 0.5-inch, as shown in **Figure 5.1b-c**, contains hundreds of Nano-AAO micropatterns with a size of 30 um or 50 μm. An SEM image of the nanopores in the Nano-AAO micropatterns is shown in the inset of **Figure 5.1c**.

Sensor surface functionalization and detection process:

Surface functionalization steps are summarized as the following (**Figure 5.2**). The sensor surface is cleaned by an air plasma cleaner (PDC-32G-HARRICK PLASMA) under high power for 5 mins. Then, 70% hydrogen peroxide solution is applied on the sensor surface at room temperature for 2 hours to obtain the active hydroxyl groups. Next, 1% Aminopropyltriethoxy silane (APTES) in 1mM acetic acid solution is applied and reacts with hydroxyl groups on the surface of Nano-AAO thin film at room temperature for 2 hours. After an oven heat treatment at 100 °C for 1h, the silane binds through all three esters, achieving a stable bond. Glutaraldehyde solution (6% in PBS) is a bifunctional aldehyde that attacks the amine group forming a Schiff base, the reaction occurs at room temperature for 2 hours followed by deionized (DI) water rinse three times. The exposed aldehyde through the same reaction can tether the capture antibody to the Nano-AAO surface. Capture antibody (monoclonal antibody-eBio16TFB), purified TGF-β1 or conditioned media (may or may not contain TGF-β1), and biotinylated detection antibody (LEAF^{TM} Purified TGF-β1 Antibody) are applied in order as a sandwich structure on the functioned sensor surface. Each step is allowed for 1-hour reaction under room temperature. The TGF-β1 binds to the capture antibody,

www.manaraa.com

and the detection antibody binds to the TGF-β1, similar to the process during ELISAs. The presence of TGF-β1 is then detected by fluorescence signal from labeled streptavidin (10 μg/ml at room temperature for 1 hour) that binds to the biotinylated detection antibody. Note that triple rigorous rinse is carried out after each step to remove unbounded chemicals.

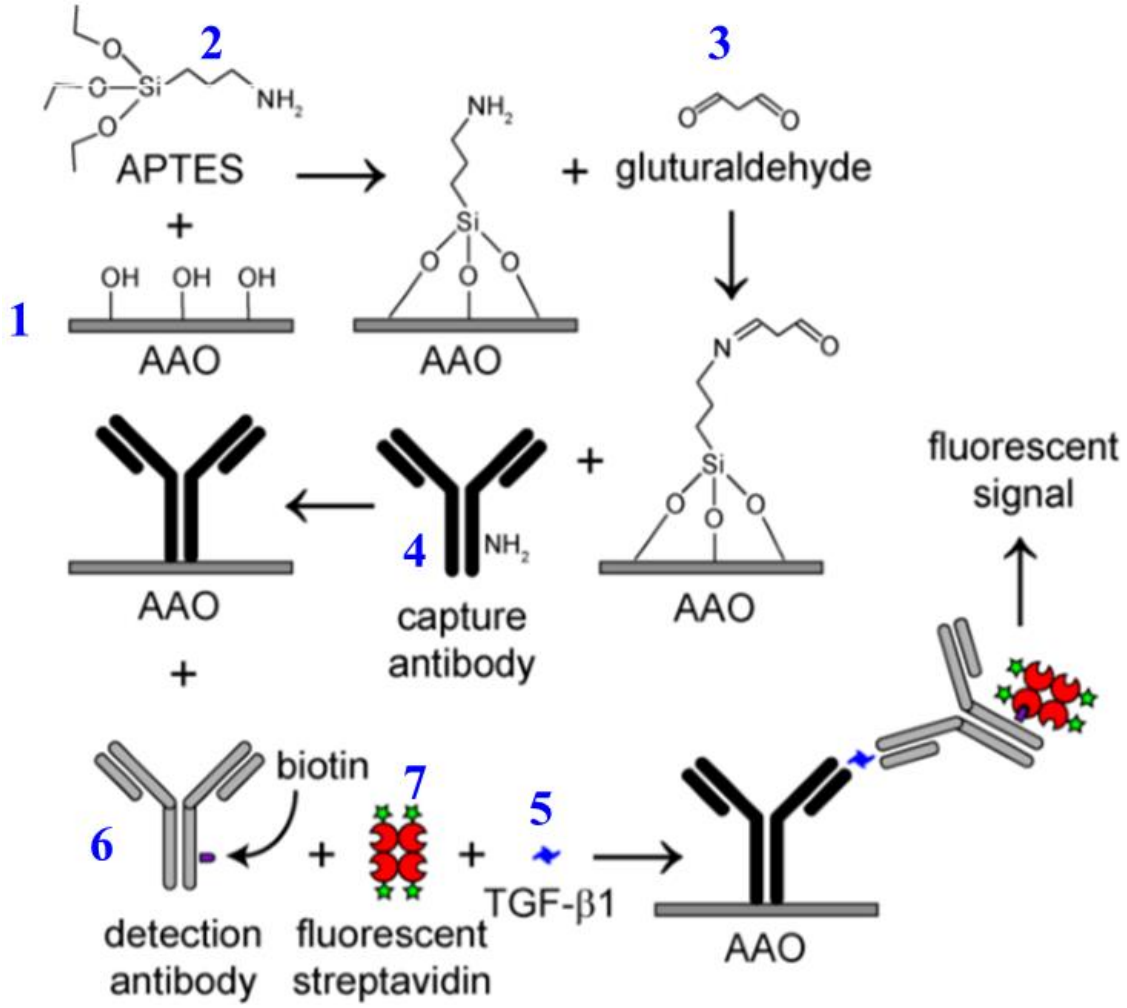

Figure 5.2 *Illustration of the detailed surface functionalization steps for detecting TGF-β1. (1) Nano-AAO surfaces are cleaned by air plasma and H_2O_2 solution, which places hydroxyls on the surface of the Nano-AAO. (2) Aminopropyltrimethoxysilane (APTES) reacts with the hydroxyls. The primary amine reacts with (3) glutaraldehyde resulting in an aldehyde group that can react with amines on the (4) capture antibody. The capture antibody binds to (5) TGF-β1. A (6) detection antibody containing a biotin label reacts with bound TGF-β1. (7) Fluorescently labeled streptavidin binds to the biotin on the detection antibody. The relative sizes of structures of 4-6 in the schematic correspond to actual relative sizes.*

www.manaraa.com

Fluorescence imaging and experimental data acquisition:

All the fluorescent images have been taken using an inverted fluorescence microscope equipped with a mercury arc lamp source (Olympus, Inc.) and a high-resolution camera (DP74-Olympus, Inc.), which has the following filter sets: FITC (excitation filter: 460-495 nm; barrier filter: 500-540 nm); and TRITC (excitation filter: 545-565 nm; barrier filter: 580-620 nm). Specially, FITC filter is used for imaging the cells labeled by calcein AM dye, FSS, and the fluorescently labeled streptavidin; TRITC filter is used for imaging the cells colored by cell tracker red CMTPX dye.

The fluorescence enhancement is calculated by analyzing the fluorescence images using the Imaging Processing toolbox in Matlab (Li et al., 2012). A Matlab program has been written to read the files of fluorescence images, which are then converted to grayscale images from the color images. A horizontal cutline is obtained through the fluorescence image, and the corresponding intensity is then plotted. In order to obtain accurate results, the fluorescence images of bare coverslip glass and bare Nano-AAO thin film have been measured and used as references. All results have been corrected by subtracting the fluorescence images of the bare glass/Nano-AAO substrates.

5.3 Results and discussion

Fluorescence sensitivity on coverslip glass and Nano-AAO thin film:

Fluorescence sodium salt (FSS) is diluted in DI water to obtain a series of concentrations including 10 μg/ml, 1 μg/ml, 100 ng/ml, respectively. The control sample of 0 ng/ml of FSS is simply DI water. The FSS solution is uniformly applied on coverslip glass and Nano-AAO thin film. All the fluorescence images are taken with an excitation light energy of 20% and an exposure time of 300 ms. As shown from **Figure 5.3(a-1)** to **Figure 5.3(a-4)**, the brightness of fluorescence images decreases with the decreasing concentrations of FSS for Nano-AAO thin film. The

www.manaraa.com

corresponding cutline-plots of the fluorescence intensity are shown in **Figure 5.3(c-1)**. The measured fluorescence images of glass coverslip are shown in **Figure 5.3(b-1)** to **Figure 5.3(b-4)**. Similarly, the corresponding cutline-plots of the fluorescence intensity are shown in **Figure 5.3(c-2).**

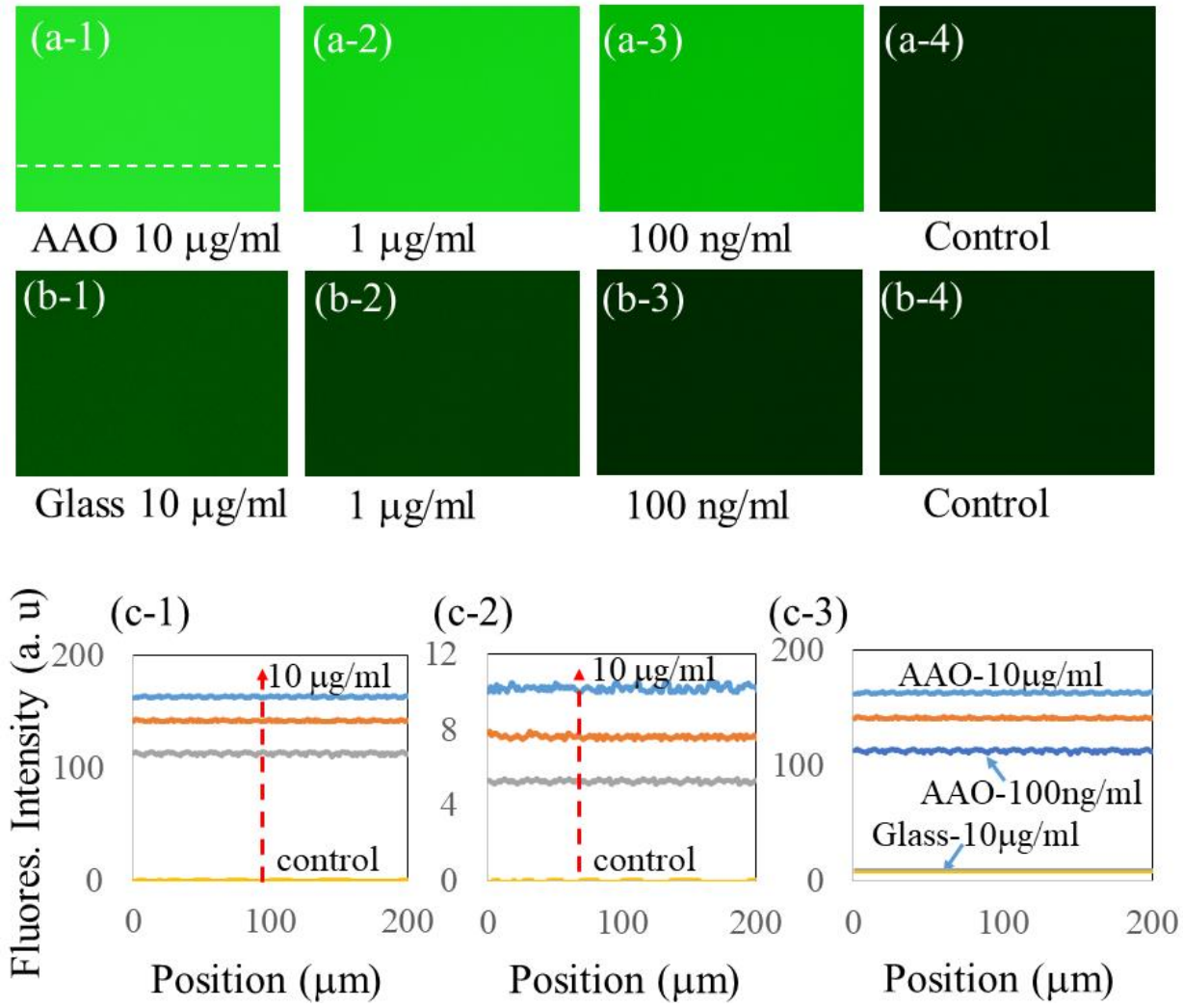

Figure 5.3 *(a-1) to (a-4) fluorescence images to detect FSS at concentrations of 10 µg/ml, 1 µg/ml, 100 ng/ml, and 0 ng/ml (control) using Nano-AAO thin film sensors, respectively; (b-1) to (b-4) fluorescence images to detect FSS at concentrations of 10 µg/ml, 1 µg/ml, 100 ng/ml, and 0 ng/ml (control) using glass coverslips, respectively; (c-1) corresponding cutline plots of the fluorescence intensities for fluorescence images from (a-1) to (a-4); (c-2) corresponding cutline plots of the fluorescence intensities for fluorescence images from (b-1) to (b-4); (c-3) cutline plots of the fluorescence intensities of 100 ng/ml FSS applied on Nano-AAO thin film and 10 µg/ml FSS on glass coverslip. All the fluorescence images are taken with a light power of 20% and an exposure time of 300 ms.*

www.manaraa.com

In order to compare the fluorescence intensity from Nano-AAO thin film samples and glass coverslip samples, several cutline-plots are shown in **Figure 5.3(c-3)**. As shown, it has been found that the fluorescence intensity of Nano-AAO thin film, when applied with FSS at a concentration of 100 ng/ml, is much larger than that of glass coverslip when applied with FSS at a concentration of 10 μg/ml. This indicates at the same fluorescence intensity, the concentration of the FSS applied on the Nano-AAO thin film is at least ~100× lower than that applied on glass coverslip. Hence, a much smaller amount of FSS is needed in the experiments for Nano-AAO thin film than glass coverslip. In the following experiments, Nano-AAO thin film sensors are used to detect the purified TGF-β1 and the TGF-β1 in the conditioned medium.

Detection of the purified TGF-β1 in buffer and control experiments:

A series of concentrations of purified TGF-β1 have been prepared by diluting in PBS buffer, resulting in 10 μg/ml, 1 μg/ml, 100 ng/ml, 10 ng/ml, and 1ng/ml, respectively. For control samples, no TGF-β1 is added to the buffer. Each sample is uniformly applied on an individual sensor surface, strictly following the protocol described in **Figure 5.2**. Note that for the control experiments, the experimental procedure is the same as the protocol in **Figure 5.2** with the exception that the control samples are applied without TGF-β1. The control experiments allow us to determine the contribution, due to the nonspecific binding between the fluorescent streptavidin to the sensor surface, to the background fluorescence signals.

The measured fluorescence images for applying these concentrations of samples are shown in **Figure 5.4(a-e),** while the measured fluorescence image for applying the control sample is shown in **Figure 5.4(f)**. The fluorescence images are taken with excitation light power of 20 % and fixed exposure time of 200 ms. Clearly the higher concentration of TGF-β1, the brighter the fluorescence

www.manaraa.com

images. The fluorescence intensities along the cutline across the Nano-AAO micropatterns are plotted in **Figure 5.4(g)**. As can be shown, the intensity for 1 ng/ml and control experiment is quite similar, while the intensity for 10 ng/ml is significantly larger than that of the control experiment. Hence it is anticipated that the limit of detection (LOD) of the sensor is at least10 ng/ml. We are continuing improving the quality of our AAO to further improve the LOD of our sensor.

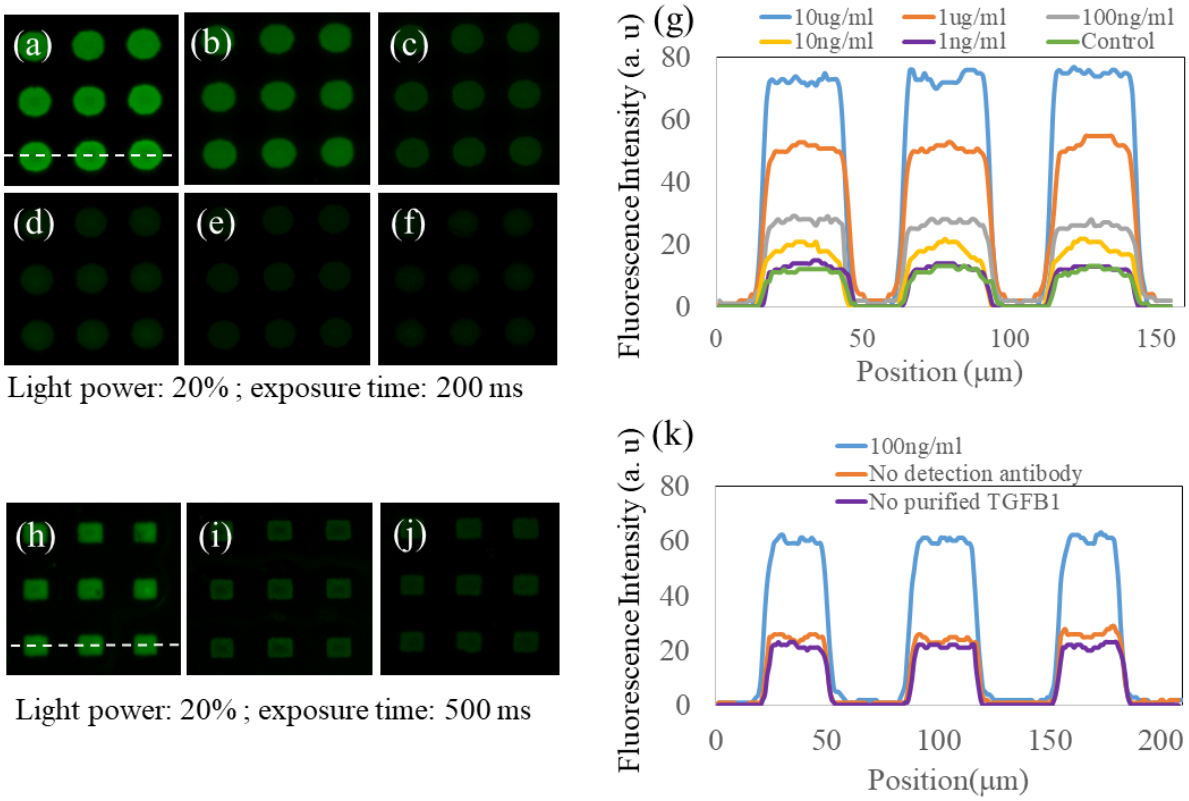

Figure 5.4 *(a-g) Fluorescence images and corresponding cutline plots of the fluorescence intensities to detect TGF-β1 at concentrations of (a)10 μg/ml, (b) 1 μg/ml, (c) 100 ng/ml, (d) 10 ng/ml, (e) 1 ng/ml and (f) 0 ng/ml (control) using Nano-AAO thin film sensor chip, respectively. All the fluorescence images are taken with a light power of 20% and an exposure time of 200 ms. (g) corresponding cutline plots of (a-f); Fluorescence images to detect TGF-β1 (h) at a concentration of 100 ng/ml, (i) without applying detection antibody, (j) without applying TGF-β1, and (k) corresponding cutline plots of (h-j). All the fluorescence images are taken with a light power of 20% and an exposure time of 500 ms.*

In order to further verify that the fluorescence signal is due to the binding of the TGF-β1, some additional control experiments have been carried out. In **Figure 5.4(h)**, 100 ng/ml purified TGF-β1 is applied on a functionalized Nano-AAO sensor surface, followed by the standard detection

www.manaraa.com

process. In **Figure 5.4(i)**, the detection antibody is not applied after the purified TGF-β1 (100 ng/ml) is applied. In **Figure 5.4(j)**, no purified TGF-β1 is applied. Hence, the sandwich assay cannot be realized for detection. Hence, no detection antibody should bind. The fluorescence images are taken with an excitation light power of 20 % and fixed exposure time of 500 ms. The fluorescence intensities for the three experiments are shown in **Figure 5.4(k)**. As shown, only the Nano-AAO sensor following the standard detection procedure (**Figure 5.4(h)**) with 100 ng/ml purified TGF-β1 has a strong fluorescence signal. The other two experiments that lack one component of the sandwich assay shows obvious low fluorescence intensity. All these experiments indicate this assay has very high specificity. Hence this sensor chip can be used to detect TGF-β1 in a complex medium such as the conditioned medium.

Cell culture to determine the cell viability on Nano-AAO substrates:

Normally, pancreatic stellate cells (iTAFs) in a quiescent state do not secrete, but when activated they do (Kitani et al., 2003; Lee et al., 2018; Manzur et al., 2017). Pancreatic cancer cells (capan-1) on the other hand do not normally secrete TGF-β1. However, they can active pancreatic stellate cells. Consequently, we examined the secretion characteristics of both mono- and co-cultures of capan-1 and iTAF cells using the Nano-AAO to detect TGF-β1.

The long-term goal of the Nano-AAO sensor is to detect single cell secretion of growth factors or other proteins. Consequently, we wanted to examine whether we could distinguish capan-1 cells from iTAF cells on the Nano-AAO sensor as well as if these cells spread and were viable on the sensor. First, we verified that we could distinguish cells in co-culture and that the cells could spread and were viable on Nano-AAO substrates. Cell tracker Red CMTPX dye is used to labeling the iTAF cells allowing us to distinguish the iTAF cells from the capan-1 cells. Capan-1 cells were

www.manaraa.com

unlabeled. The mixed cells sample is subsequently seeded inside the sensor chip. Furthermore, calcein AM dye is used to label live cells, and thus the cell viability can be monitored during detection of TGF-β1. Both mono-and co-culture conditions for capan-1 and iTAF cells used a total cell of 200,000 cells/ml. In the future work, we are going to collect more data for different cell concentrations and different ratio of capan-1 and iTAF.

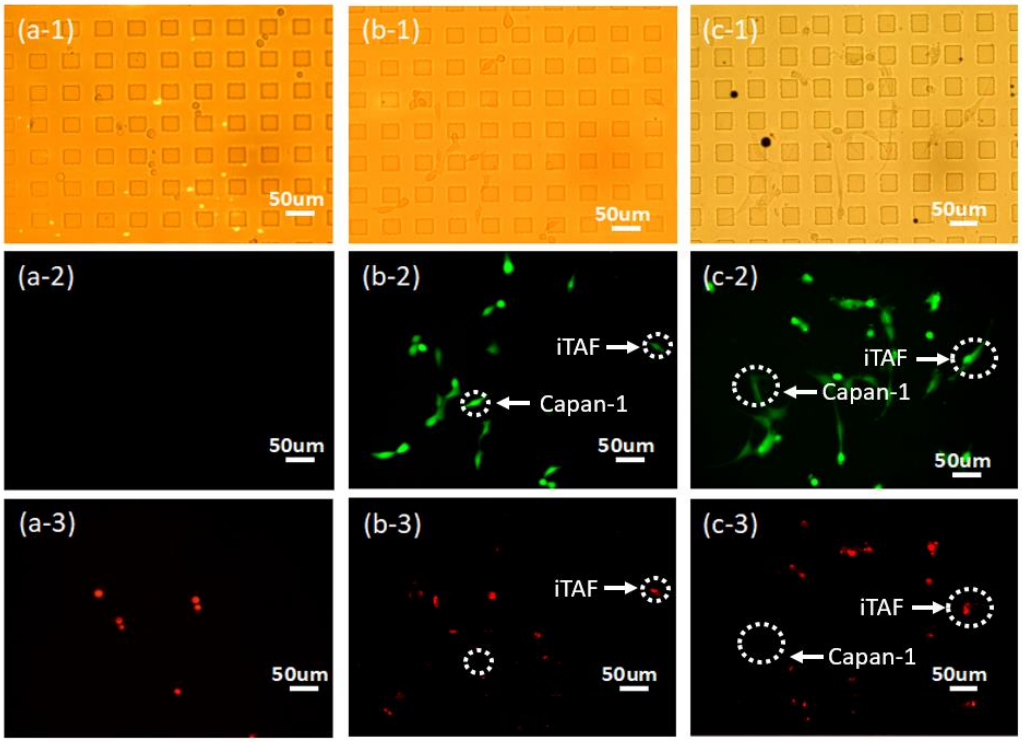

Figure 5.5 *(a-1) Optical micrograph showing the mixture of iTAF cells and capan-1 cells immediately after they are seeded in the Nano-AAO sensor chip; (b-2) to (b-3) The corresponding fluorescence images of the iTAF cells among all the cells; (b-1) Optical micrograph showing the mixture of iTAF cells and capan-1 cells after 24-hour culture; The corresponding fluorescence images of (a-2) all cells and (a-3) iTAF cells among all the cells; (c-1) Optical micrograph showing the mixture of iTAF cells and capan-1 cells after 48-hour culture; (a-2) to (a-3) The corresponding fluorescence images of (c-2) all cells and (c-3) the iTAF cells among all the cells*

An optical image immediately after seeding the cells is shown in **Figure 5.5a-1.** Its corresponding fluorescence images using TRITC filter and FITC filter are shown in **Figure 5.5a-2** and **Figure 5.5a-3**, respectively. As expected, only the labeled iTAF cells appear in red in **Figure 5.5a-3,** while the **Figure 5.5a-2** shows no signal. After 24-hr incubation, the chip is taken out from

www.manaraa.com

the incubator, and calcein AM with a concentration of 1 μM is applied to color all living cells. An optical image of the cells in the chip is shown in **Figure 5.5b-1**. As shown in the corresponding fluorescence image in **Figure 5.5b-2**, essentially all the cells in **Figure 5.5b-1** are alive. The iTAF cells among those cells can be distinguished by their red color fluorescence in **Figure 5.5b-3**. Similar optical and fluorescence images are obtained after 48 hr incubation. As shown in **Figure 5.5c-1** to **Figure 5.5c-3**, higher cell density is seen at 48 hr, indicating that the cells can proliferate on the chip with high viability.

Detection of the secreted TGF-β1 in the conditioned medium:

To test whether we could detect TGF-β1 in media, we conditioned media in both mono- and co-culture containing a total of 10^6 cells/ml. Three types of conditioned media have been used for the measurements (capan-1, iTAF, and capan-1/iTAF). Conditioned media was assayed either undiluted or diluted with unconditioned media (10% and 1%) and TGF-β1 was detected in these samples.

As shown in **Figure 5.6(a)**, the undiluted co-culture media sample shows the brightest fluorescence images, and the fluorescence images becomes dimmer after 10% (**Figure 5.6(b)**) and 1% (**Figure 5.6(c)**) dilution of the original sample. In **Figure 5. 6(d)**, the measured fluorescence image is for the media sample from mono-culture of iTAF cells. In **Figure 5.6(e)**, the measured fluorescence image is for the media sample from the mono-culture of capan-1 cells. In **Figure 5.6(f)**, the measured fluorescence image is for a control experiment containing no cells. Again all the fluorescence images are taken with excitation light power of 20% and fixed exposure time of 200 ms. The corresponding fluorescence intensities along the cutline shown in **Figure 5.6(a)** are shown in **Figure 5.6(g)**. Dilution results in lower signals for all culture conditions (**Figure 5.6(g)**).

www.manaraa.com

Furthermore, the co-culture condition (capan-1/iTAF) showed much larger fluorescence than either the mono-culture of capan-1 cells or the mono-culture of iTAF cells. The mono-culture of capan-1 cells seems to generate a fluorescence that was the same as that for the control media that did not include cells, indicating that capan-1 cells do not secrete TGF-β1. The conditioned media from the 10 % diluted co-culture resulted in a higher fluorescence signal than the undiluted mono-culture of iTAFs, suggesting that activated iTAFs, secrete more than 10-fold more TGF-β1 than quiescent iTAFs in mon-culture.

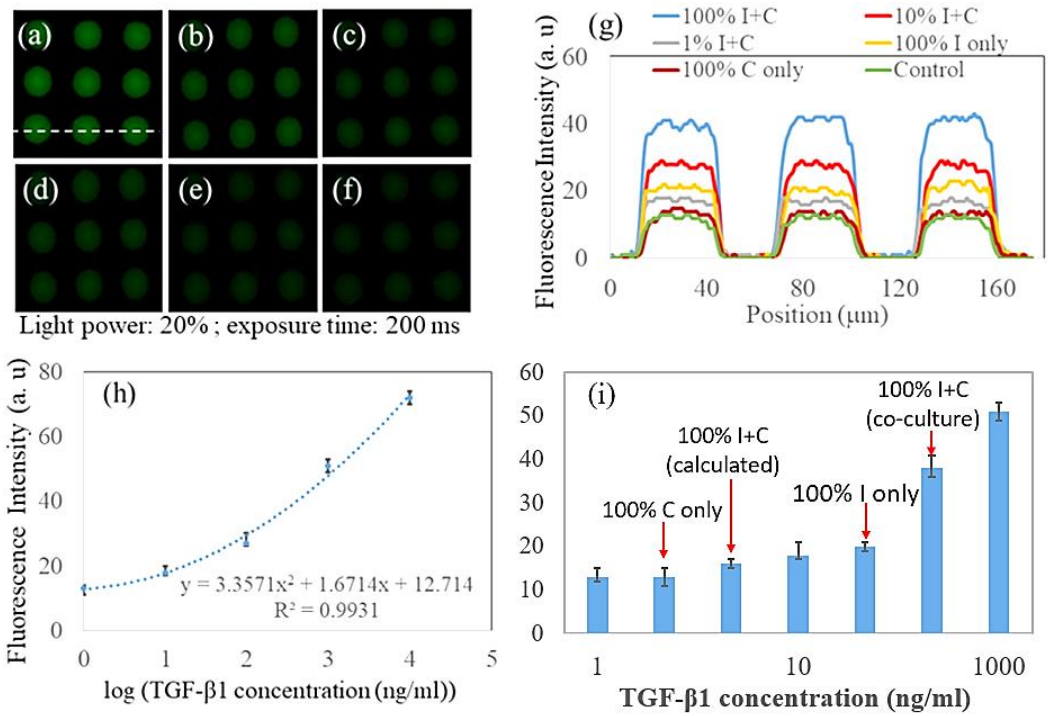

Figure 5.6 *Measured fluorescence images for TGF-β1 at concentrations of (a) original conditioned medium for co-culturing iTAF cells and capan-1 cells (100% I+C); (b) 10% diluted original conditioned medium (10% I+C); (c) 1% diluted original conditioned medium (1% I+C); (d) original conditioned medium for culturing iTAF cells only (100% I only); (e) original conditioned medium for culturing capan-1 cells only (100% C only); (f) control experiments; (g) the corresponding cutline plots of the fluorescence intensities of (a-f); (h) The measured fluorescence intensities of samples: (100% I+C) and (100% I only), along with the measured fluorescence intensities of samples with known concentrations of TGF-β1*

www.manaraa.com

Estimation of the unknown TGF-β1 concentration in the original conditioned medium:

Two additional experiments have been conducted to repeat the experiments in section 3.4 for detecting the purified TGF-β1. The averaged fluorescence intensity for each concentration of TGF-β1 is plotted in **Figure 5.6h**. Note that all the fluorescence images are taken with excitation light power of 20% and fixed exposure time of 200 ms, which is the same as that for experiments detecting TGF-β1 in the conditioned medium. As expected, the averaged fluorescence intensity increases with the increased concentration of TGF-β1. The fluorescence intensity at a concentration of 0 ng/ml of TGF-β1, which is the control sample is not significantly different from 1ng/ml of TGF-β1, demonstrating the sensitivity of the detection. The fluorescence intensity at a concentration of 10 ng/ml of TGF-β1 is ~64% higher than that of the control sample, again verifying the detection limit is at least 10 ng/ml of TGF-β1 for this sensor. The unknown TGF-β1 concentration in the conditioned medium can be estimated by comparing the measured fluorescence intensity of the sample with those measured from the known concentrations of the purified TGF-β1 (**Figure 5.6i**). Based on the measured fluorescence intensities in **Figure 5.6g**, the TGF-β1 concentration in the conditioned medium of culturing iTAF cells (100% I only) is ~17.6 ng/ml. And the TGF-β1 concentration in the conditioned medium of co-culturing iTAF cells and capan-1 cells (100% I+C) is ~321.2 ng/ml.

5.4 Conclusions

The detection of the transforming growth factor TGF-β1 secreted by pancreatic stellate cells (iTAF) in buffer and conditioned medium using a Nano-AAO thin film enabled fluorescence sensor has been demonstrated. Using a sandwich assay, purified TGF-β1 in buffer has been detected successfully. It has been found that as low as 10 ng/ml TGF-β1 in buffer can be readily detected. The high specificity of the sandwich assay as demonstrated in the control experiments

www.manaraa.com

suggests that this type of sensor is suitable for detecting the TGF-β1 in complex media. Using this sensor, TGF-β1 secreted by ITAF cells alone or in co-culture with capan-1 cells in culture media have been detected successfully. The concentration of TGF-β1 in the conditioned medium from culturing iTAF cells only for 48 hrs is found to be ~17.6 ng/ml, and from co-culturing iTAF cells and capan-1 cells is found to be ~321.2 ng/ml. Next step, the possibility of real-time monitoring of the cell secretion, especially at the single cell level, using this fluorescence sensing platform will be studied.

References

[1] Bonnans, C., J. Chou, and Z. Werb. 2014. Remodelling the extracellular matrix in development and disease. Nature reviews Molecular cell biology. 15:786.

[2] Che, X., P. Deng, J. Song, and L. Que. 2018. Studies of mechanisms and characteristics of the fluorescence enhancement on anodic aluminum oxide thin film. Applied Nanoscience:1-8.

[3] Che, X., Y. He, H. Yin, and L. Que. 2015. A molecular beacon biosensor based on the nanostructured aluminum oxide surface. Biosensors and Bioelectronics. 72:255-260.

[4] Domaille, D.W., E.L. Que, and C.J. Chang. 2008. Synthetic fluorescent sensors for studying the cell biology of metals. Nature chemical biology. 4:168.

[5] Gee, K.R., Z.-L. Zhou, W.-J. Qian, and R. Kennedy. 2002. Detection and imaging of zinc secretion from pancreatic β-cells using a new fluorescent zinc indicator. Journal of the American Chemical Society. 124:776-778.

[6] Gnecchi, M., Z. Zhang, A. Ni, and V.J. Dzau. 2008. Paracrine mechanisms in adult stem cell signaling and therapy. Circulation research. 103:1204-1219.

[7] Guo, W., and F.G. Giancotti. 2004. Integrin signalling during tumour progression. Nature reviews Molecular cell biology. 5:816.

[8] Gupta, G.P., and J. Massagué. 2006. Cancer metastasis: building a framework. Cell. 127:679-695.

[9] He, Y., X. Li, and L. Que. 2014. A transparent nanostructured optical biosensor. Journal of biomedical nanotechnology. 10:767-774.

www.manaraa.com

[10] Han, Q., Bradshaw, E., Nilsson, B., Hafler, D. and Love, J. (2010). Multidimensional analysis of the frequencies and rates of cytokine secretion from single cells by quantitative microengraving. Lab on a Chip, 10(11), p.1391.

[11] Kitani, A., I. Fuss, K. Nakamura, F. Kumaki, T. Usui, and W. Strober. 2003. Transforming growth factor (TGF)-β1–producing regulatory T cells induce Smad-mediated interleukin 10 secretion that facilitates coordinated immunoregulatory activity and amelioration of TGF-β1–mediated fibrosis. Journal of Experimental Medicine. 198:1179-1188.

[12] Lander, A.D. 2013. How cells know where they are. Science. 339:923-927.

[13] Laklai, H., et al., Genotype tunes pancreatic ductal adenocarcinoma tissue tension to induce matricellular fibrosis and tumor progression. Nature Medicine, 2016. 22(5): p. 497-505.)

[14] Lee, J.-H., S.-K. Kim, I.A. Khawar, S.-Y. Jeong, S. Chung, and H.-J. Kuh. 2018. Microfluidic co-culture of pancreatic tumor spheroids with stellate cells as a novel 3D model for investigation of stroma-mediated cell motility and drug resistance. Journal of Experimental & Clinical Cancer Research. 37:4.

[15] Lu, Y., Chen, J., Mu, L., Xue, Q., Wu, Y., Wu, P., Li, J., Vortmeyer, A., Miller-Jensen, K., Wirtz, D. and Fan, R. (2013). High-Throughput Secretomic Analysis of Single Cells to Assess Functional Cellular Heterogeneity. Analytical Chemistry, 85(4), pp.2548-2556.

[16] Li, X., Y. He, and L. Que. 2013. Fluorescence detection and imaging of biomolecules using the micropatterned nanostructured aluminum oxide. Langmuir. 29:2439-2445.

[17] Li, X., Y. He, T. Zhang, and L. Que. 2012. Aluminum oxide nanostructure-based substrates for fluorescence enhancement. Optics express. 20:21272-21277.

[18] Luchansky, M.S., and R.C. Bailey. 2010. Silicon photonic microring resonators for quantitative cytokine detection and T-cell secretion analysis. Analytical chemistry. 82:1975-1981.

[19] Manzur, A., A. Oluwasanmi, D. Moss, A. Curtis, and C. Hoskins. 2017. Nanotechnologies in Pancreatic Cancer Therapy. Pharmaceutics. 9:39.

[20] Mouw, J.K., G. Ou, and V.M. Weaver. 2014. Extracellular matrix assembly: a multiscale deconstruction. Nature reviews Molecular cell biology. 15:771.

[21] Shirasaki, Y., M. Yamagishi, N. Suzuki, K. Izawa, A. Nakahara, J. Mizuno, S. Shoji, T. Heike, Y. Harada, and R. Nishikomori. 2014. Real-time single-cell imaging of protein secretion. Scientific reports. 4:4736.

[22] Son, K.J., P. Gheibi, G. Stybayeva, A. Rahimian, and A. Revzin. 2017. Detecting cell-secreted growth factors in microfluidic devices using bead-based biosensors. Microsystems & Nanoengineering. 3:17025.

www.manaraa.com

[23] Stastna, M., and J.E. Van Eyk. 2012. Secreted proteins as a fundamental source for biomarker discovery. Proteomics. 12:722-735.

[24] Wang, S., S. Ota, B. Guo, J. Ryu, C. Rhodes, Y. Xiong, S. Kalim, L. Zeng, Y. Chen, and M.A. Teitell. 2011. Subcellular resolution mapping of endogenous cytokine secretion by nano-plasmonic-resonator sensor array. Nano letters. 11:3431-3434.

[25] Wehr, A.Y., et al., Analysis of the Human Pancreatic Stellate Cell Secreted Proteome. Pancreas, 2011. 40(4): p. 557-566.

[26] Yin, H., X. Li, and L. Que. 2014. Fabrication and characterization of aluminum oxide thin film micropatterns on the glass substrate. Microelectronic Engineering. 128:66-70.

www.manaraa.com

CHAPTER 6. ON-CHIP STUDIES OF MAGNETIC STIMULATION EFFECT ON SINGLE NEURAL CELL VIABILITY AND PROLIFERATION ON GLASS AND NANOPOROUS SURFACES

Modified from a journal paper submitted to *ACS Applied Materials & Interfaces (under revision)*

Xiangchen Che, Joseph Boldrey, Xiaojing Zhong, Ian Schneider, David Jiles, and Long Que

Abstract

Transcranial magnetic stimulation (TMS) is a non-invasive neuromodulation technique, an FDA-approved treatment method for various neurological disorders such as depressive disorder, Parkinson's disease, post-traumatic stress disorder, and migraine. However, information concerning the molecular/cellular-level mechanisms of neurons under magnetic stimulation (MS), particularly at the single neural cell level, is still lacking, resulting in very little knowledge of the effects of MS on neural cells. In this paper, the effects of MS on the behaviors of neural cell N27 at the single-cell level on coverslip glass substrate and anodic aluminum oxide (AAO) nanoporous substrate are reported for the first time. First, it has been found that the MS has a negligible cytotoxic effect on N27 cells. Second, the effect of MS on N27 cells can be clearly observed over 24 hours—the duration of one cell cycle—after MS is applied to the cells. The size of cells under MS was found to be statistically smaller than that of cells without MS after one cell cycle. Furthermore, directly monitoring cell division process in the microholders on a chip revealed that the cells under MS generated statistically more daughter cells in one cell cycle than those without MS. All these results indicate that MS can affect the behavior of N27 cells, promoting their proliferation and regeneration.

6.1 Introduction

Transcranial magnetic stimulation (TMS) is a non-invasive neuromodulation technique that uses time-varying short pulses of magnetic fields to induce an electric field in the conductive tissues of

www.manaraa.com

the brain, thus modulating the synaptic transmission of neurons. This neuromodulation technique can be used to excite or inhibit the firing rate of neurons as a treatment for various neurological disorders such as major depressive disorder, Parkinson's disease, post-traumatic stress disorder, and migraine [1, 2]. Information concerning the molecular/cellular mechanisms of neurons under MS, particularly at the single neural cell level, is still lacking. The effects of MS on single neural cells need to be thoroughly understood in order for experts to make the greatest use of MS as a neuromodulation tool for treating neurological disorders, especially those originating from the subcortical regions of the brain.

In order to study the behaviors of single neural cells *in vitro*, a solid substrate or scaffold is usually needed for the cell's proper adhesion, spread, and growth [3]. It is particularly desirable to create a substrate or scaffold mimicking the native extracellular environment that can interface with individual neural cells within living tissues and in the culture. As previous studies have demonstrated, substrates or scaffolds with nanoscale features (i.e. nanostructured bio-interfaces) have greatly improved specificity and accuracy for many neural-engineering applications [4-6], including neural probes for Parkinson's patients and guidance scaffolds for axonal regeneration in patients with traumatic nerve injuries [7, 8], just to name a few.

Hence, nanostructured bio-interfaces have become a rapidly emerging area of study. For instance, over the past decades, which have witnessed the development of nanotechnology and nanomaterial that is safe for biological applications, interfaces between a variety of nanomaterials or nanostructures with biomolecules have been studied [9]. Examples of nano-bio-interfaces include the interface of the nanoparticle-lipid bilayer [10], the interface of carbon nanotubes (CNTs)-biomolecules [11], and the interface of graphene-biomolecules [12]. The studies of nano–bio-interfaces primarily aim to understand the dynamic physicochemical interactions, kinetics, and

www.manaraa.com

thermodynamic exchanges between nanomaterial surfaces and the surfaces of biological components, which include, for example, proteins, membranes, phospholipids, endocytic vesicles, organelles, DNA, and biological fluids. One widely used nanostructured material is anodic aluminum oxide (AAO). The unique properties of nanoporous AAO thin film have greatly contributed to the development of a variety of novel biomedical and medical applications, ranging from biofiltration membranes, lipid bilayer support structures, biosensing devices, and implant coatings to drug delivery systems with AAO capsules and scaffolds for tissue engineering [13-19]. Additionally, nanoporous AAO membranes have generated increasing interest and shown great promise as cell-interface substrates for manifold cell types [19].

In this paper, an AAO nanoporous surface is used as one of the substrates to study the behaviors of neural cell N27. More specifically, the effects of MS on the behaviors of neural cell N27 at the single-cell level on a glass surface and an AAO nanoporous surface are reported for the first time.

6.2 Materials and methods

6.2.1 Materials

(1) The experiments use neural cell N27 (*Millipore Sigma*), which stands for immortalized rat mesencephalic cells (1RB3AN27). The following chemicals are used for culturing the N27 neural cell: RPMI-1640 medium (*Sigma-Aldrich*) supplemented with 10% fetal bovine serum (*Sigma-Aldrich*); 1% L-glutamine (*Sigma-Aldrich*); penicillin with a concentration of 100 U/ml (*Sigma-Aldrich*); and streptomycin in 100 U/ml (*Sigma-Aldrich*). (2) Fluorophores, calcein AM (*Sigma-Aldrich*), and propidium iodide (*Sigma-Aldrich*) are used for monitoring cell viability using a fluorescence microscope (Olympus, Inc.). (3) Scanning Electron Microscopy (SEM) is used to image the neuron cell growth on different substrates. Standard PBS (*Sigma-Aldrich*), 4%

www.manaraa.com

paraformaldehyde in a 0.1 M PO4 buffer (*Sigma-Aldrich*), Ethanol >99% (*Sigma-Aldrich*), and Hexamethyldisilazane (HMDS) >99% (*Sigma-Aldrich*) are used for sample pretreatment before SEM imaging. (4) Aluminum pellets with a purity of 99.999% (*Iamaterials, Inc.*), Titanium pellets with a purity of 99.995% (*Iamaterials, Inc.*), and SU-8 3025 (*Microchem, Inc.*) are used to fabricate microholder chips.

6.2.2 Substrates for the studies of viability and behaviors of neuron cells N27

Different surfaces/substrates were prepared for studying neuron cell growth: standard coverslip glass (*Thermo Fisher Scientific, Inc.*), AAO substrates fabricated by a one-step anodization process, and AAO substrates fabricated by a two-step anodization process. The procedure for preparing the AAO substrates is described in detail in our previous work [20]. Briefly, after a layer of Al is deposited on a glass substrate, a *one-step* anodization process is carried out to convert the Al into a nanoporous AAO thin film. An SEM image of the AAO substrates fabricated by the one-step anodization process is shown in **Figure 6.1a**. The two-step anodization process begins with 10 minutes of anodizing the A1 layer in 0.3 M oxalic acid. Then the samples are etched with a mixture of phosphoric acid (0.4 M) and chromic acid (0.2 M) at 65 °C for 30 minutes, followed by a 40-minute step-two anodization in 0.3 M oxalic acid with the same experimental condition as the step-one anodization. An SEM image of the AAO substrates fabricated by the two-step anodization process is shown in **Figure 6.1b**. The average nanopore diameter of the one-step AAO substrates (*AAO-substrate1*) is ~20nm, and its average porosity is 6.6%. The two-step AAO substrates (*AAO-substrate2*) have an average diameter of ~80 nm and an average porosity of 84.11%. As shown, the nanopore size and porosity of the *AAO-substrate2* are larger and more uniform than those of *AAO-substrate1*. The two AAO substrates therefore have differently nanostructured topological surfaces.

www.manaraa.com

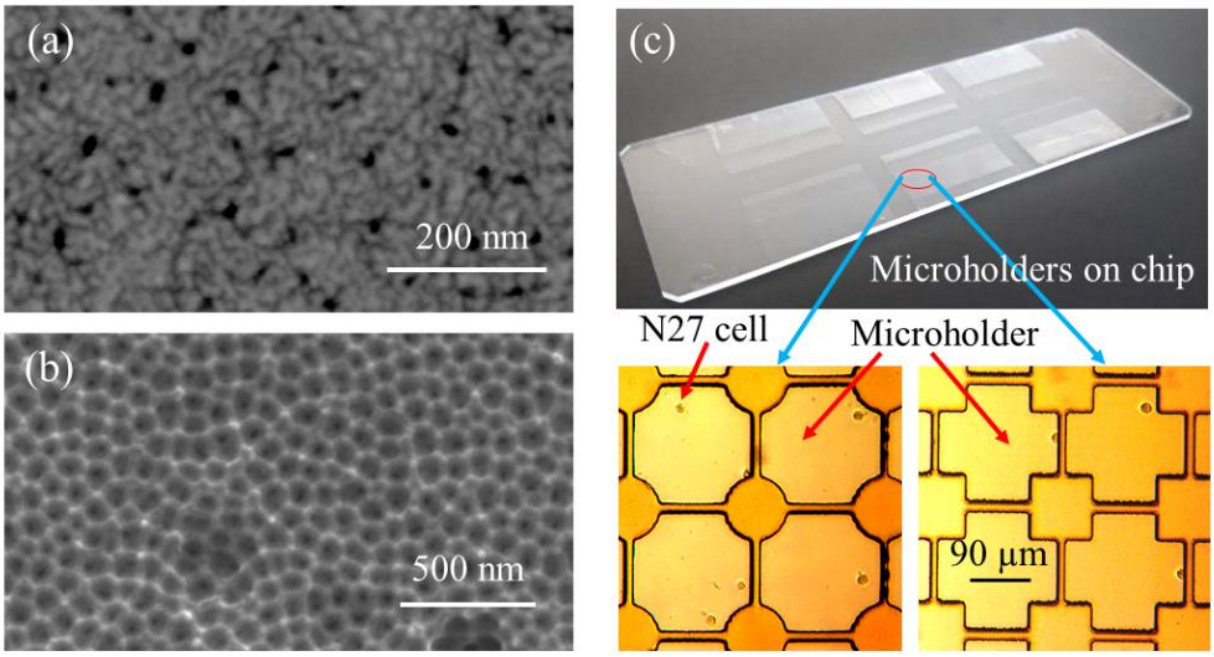

Figure 6.1 *SEM images of (a) AAO-substrate1: nanopore diameter=20nm, porosity=6.6%; (b) AAO-substrate2: nanopore diameter=100nm, porosity=84.11%; (c) A photo of microholders on-chip and the close-up optical micrographs of arrayed SU8 microholders and the captured single neural cell N27.*

6.2.3 Arrayed SU8 microholder chip for studying the viability and growth of single neural cell N27

Two types of SU8 microholder chips have been designed and fabricated. One type consists of arrayed microholders embedded with glass surfaces; the other type consists of arrayed microholders embedded with nanoporous AAO surfaces. The fabrication processes flow for the SU8 microholder chip with an AAO nanoporous surface (*AAO microchip*) and for the SU8 microholder chip with a glass surface (*glass microchip*) are described in the supplementary document. **Figure 6.1c** shows a photo of an SU8 microholder chip and the close-up optical micrographs of the microholders.

6.2.4 Substrate cleaning, cell synchronization, cell seeding, and SEM imaging

Disinfection: Both AAO nanoporous substrates and glass substrates are cleaned for 5 minutes with DI water using the ultra-sonicator (*BRANSON 1510-Fisher Scientific*), and disinfection of these

www.manaraa.com

substrates is achieved by cleaning them with Acetone and Methanol with the ultra-sonicator for 5 minutes in sequence. The substrates are then cleaned with DI water by ultra-sonicating for 5 minutes and dried by a nitrogen gun, followed by air plasma cleaning (*Harrick plasma-PCD 32G*) for 3 minutes. Finally, they are baked for 5 minutes on a hot plate at 150°C before use.

Cell synchronization: In general, the cells in a culture will grow at different stages within the cell cycle. The bio-specific differences of each cell make it difficult to keep all the cells in the same phase without any pretreatment [21]. In order to obtain statistically accurate results of the effect of MS on the cell division process for a large number of cells, cell synchronization, a process that brings cells at different stages of the cell cycle to the same phase, must be implemented. To this end, a simple serum deprivation method is used by changing the percentage of fetal bovine serum from 10% to 1% in the cell culture medium [21, 22]. Specifically, the medium of 10% fetal bovine serum is replaced with 1% fetal bovine serum 9 hours before the cells are seeded into the microholders. A 9-hour serum deprivation time was chosen for this study for a number of reasons. First, cell mortality was taken into account. Since the serum constitutes the nutrition essential for cell growth, the cells' death risk increases with the serum deprivation time. Based on our experiments, 9-hour serum deprivation is a safe period to avoid cell death. Moreover, a 9-hour synchronization period is required to ensure that most of the cells have been synchronized to the G1 phase, the first of four phases of the cell cycle that takes place in eukaryotic cell division [22].

Cell seeding: Trypsin is used to detach the cells from the bottom of the flask before the cells are seeded on different substrates. After 2 or 3 minutes, we pipette a normal medium with 10% fetal bovine serum to the flask. Then the cells are ready to be seeded to the microholder devices.

Cell labeling with fluorophores and fluorescence imaging: In order to carry out the live/dead assay and monitor cell viability, we label the cells with fluorophores calcein-AM and propidium

www.manaraa.com

iodide, using a concentration of 2 μM. Fluorescence images are captured with a fluorescence microscope (Olympus, Inc.).

SEM imaging: The following steps are taken to obtain SEM images of the cells' growth on the glass and AAO surfaces. First, after 3 days of growth, the samples are rinsed with PBS. Then the neuron cells are fixed in 4% paraformaldehyde resolved in a 0.1 M phosphate (PO_4) buffer with a pH of 7.4 for 20 minutes at room temperature. Second, the samples are rinsed 5 times with PBS at room temperature and then with a DI water rinse for 10 minutes. Third, dehydration is achieved by immersing the samples into solutions of 25%, 50%, 70%, 80%, 85%, 90%, 95%, and 100% ethanol for 10 minutes each, followed by an additional two rinses with 100% ethanol. Last, the samples are rinsed with three mixtures of ethanol and HMDS, with volume ratios of 3:1, 1:1, and 1:3, for 10 minutes each. Then the samples are rinsed twice with pure HMDS for 10 minutes and left in the HMDS until completely dry. The samples are then ready for SEM imaging.

6.2.5 Experimental setup for applying MS to N27 neural cells

The Magstim 2002 monophasic stimulator with an '8'-shaped coil (*Magstim D702 double 70 mm*) is used to apply MS to the cells, as shown in **Fig. S1a** (see supplementary document). The magnetic fields are generated in opposite directions through the two windings and are perpendicular to the surface of the '8'-shaped coil so as to be perpendicular to the chip holder on both sides. As shown in **Fig. S1b**, an upward magnetic field (MF) is generated from the left side of the coil, and a downward MF is introduced from the right. The power level is set to 100% and the MF strength for the coil is shown in **Fig. S1c**. The upward peak MF strength is ~1.5MA/m and the downward peak MF is ~1.25 MA/m.

www.manaraa.com

6.2.6 Statistical analysis

The study focuses on cell growth under two different experimental conditions. First, the cell morphology (i.e. area) of each single N27 cell on different substrates after a 48-hour incubation period has been measured. Second, hundreds of single N27 cells have been captured inside each SU8 microholder, and the division process of each cell has been monitored by counting cell numbers in each SU8 microholder after a 48-hour incubation period. For each case, several trials have been conducted to collect sufficient data for statistical analysis. The experimental conditions and parameters are summarized in **Table 6.1**.

Table 6.1 *Summary: experimental conditions and parameters*

Experiments	Substrate/microchip	When MS is applied	NT (# of trail)	NC (# of cells)
Cell morphology (cell size/area measurement)	AAO-substrate1	24 hrs	3	370
	AAO-substrate2	24 hrs	3	429
	Glass substrate	24 hrs	3	196
Cell division (cell count)	Glass microchip	24 hrs	5	880
	AAO microchip	24 hrs	5	2073

Specifically, for the morphometric analysis of N27 cells, experiments with N27 cells on three substrates (AAO-substrate1, AAO-substrate2, and glass substrate) have been carried out. For all experiments, MS is applied when the cells have been seeded and grow on the substrates 24 hours later. In other words, the cells settle on the substrates' surface and are allowed one day of growth before the application of MS. Three independent trials (NT=number of trial) have been performed for each substrate. For each trial, at least 65 cells (NC=number of cell) are selected for cell area measurement. More details can be found in **Table 6.S1 (**see supplementary document).

In order to analyze the N27 cell division process, experiments on two types of microchip (glass and AAO) are performed. On both microchips, only microholders with single N27 cell captured

www.manaraa.com

in each are monitored in order to track cell division accurately. For both glass and AAO microchips, MS is only applied after one-day (24-hour) growth of the captured cells. Five independent trials are performed for each substrate. For each trial, at least 150 single N27 cells are captured in 150 microholders. More details can be found in **Table 6.S2** (see supplementary document).

SPSS statistical analysis is used to analyze the experimental data. Tests of normality, outliers, and homogeneity variance are performed for each group of data before a one-way analysis of variance (ANOVA) [23]. The statistical significance is reported with $p < 0.05$ and $p < 0.005$ for each group of data. The one-way ANOVA test results are shown in the following section, and more detailed information about the statistical analysis can be found in the supplementary material.

6.3 Results and discussion

6.3.1 Growth of N27 cells on different substrates

The N27 cells are seeded on an AAO nanoporous surface (**Figure 6.2a-b**) and a coverslip glass surface (**Figure 6.2f-g**). Cells are then cultured in an RPMI medium supplemented with 10% fetal bovine serum, 1% L -glutamine, penicillin (100 U/ml), and streptomycin (100 U/ml). Petri dishes are used as the container, and all the samples are kept in an incubator (*NUAIRE-5700*) at 37°C in a humidified atmosphere of 5% CO_2 during the cell culture process. It should be noted that both the coverslip glass surface and the AAO nanopore surface shown in **Figure 6.2** are bare surfaces used directly after the cleaning process without any further surface treatment.

As shown in **Figure 6.2a-b**, cells spread out clearly on the AAO nanoporous surface over the course of 24 hours of growth and 3 days of growth alike. By contrast, “ball-shaped” cells are observed after one day of growth on coverslip glass (**Figure 6.2f**). After three days of growth, over 50% of these cells still grow in clusters (**Figure 6.2g**), indicating that they have a relatively slower

www.manaraa.com

migration than those on the AAO substrate [24]. AFM images of the AAO substrate and glass substrate are shown in **Figure 6.2c** and **Figure 6.2h,** respectively. As indicated, the surface roughness of the AAO substrate is significantly greater than that of the coverslip glass. Clearly, the nanoporous surface of the AAO substrate is much preferred for cells' adhesion and spread. Thus, their cell morphology has been obviously improved compared to that of the cells on coverslip glass [25]. The corresponding SEM images of a single N27 neural cell's growth on the AAO surface and on the glass surface are shown in **Figure 6.2d-e** and **Figure 6.2i-j**, respectively.

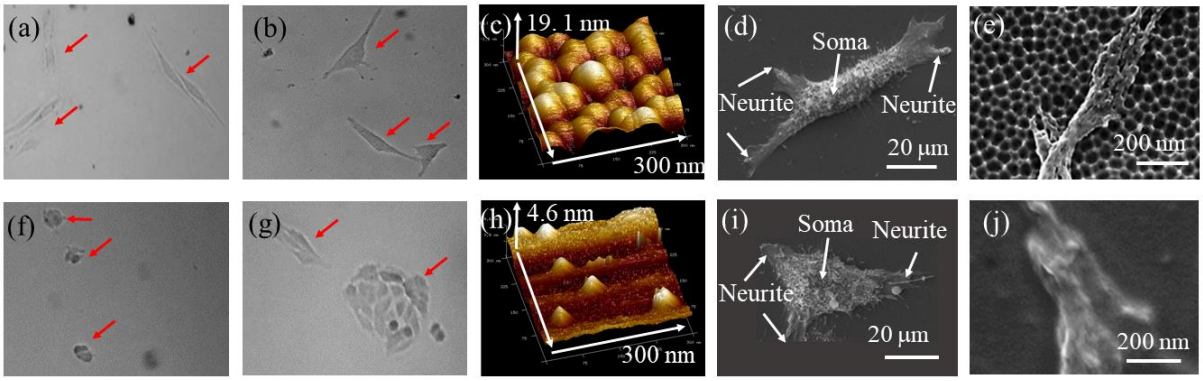

Figure 6.2 *N27 neural cell growth on nanoporous substrate (a-e) vs glass coverslip substrate (f-j): (a) and (f) after one-day growth; (b) and (g) after three-day growth (cells are indicated with red arrows); (c) and (h) AFM images of AAO surface and glass surface, respectively; (d-e) and (i-j) SEM images for a single N27 neural cell growing on AAO surface and glass surface, respectively.*

6.3.2 Viability of N27 cells on different substrates under MS

In order to assess the viability of N27 cells under MS, cellular viability tests by calcein AM and propidium iodide (PI)-based live/dead assay have been performed [26]. In these experiments, four substrates have been used, including coverslip glass, AAO substrate, glass microchip, and AAO microchip. All the surfaces of these substrates are coated with poly-D-lysine. MS is applied after the cells grow on these substrates for 24 hours (i.e. one cell cycle). As expected [27], the cell

www.manaraa.com

morphology on the poly-D-lysine-coated coverslip glass in **Figure 6.3a, c** is superior to that on bare coverslip glass in **Figure 6.2f, g**, equivalent to that on bare AAO substrate in **Figure 6.2a, b** and poly-D-lysine-coated AAO substrate in **Figure 6.3b, d**. As evident from the fluorescence images (**Figure 6.3a-d**) and viability quantification of the cells (**Figure 6.3e**) on the four substrates, MS has a negligible cytotoxic effect on cells. Furthermore, as shown in **Figure 6.3c-d**, the cell division can also be observed clearly. For example, in the image from the glass microchip in **Figure 6.3c**, a single N27 cell is captured and divided into two daughter cells 24 hours (one cycle) later. At this point, MS is applied, and the two daughter cells grow and are divided into five live cells 24 hours later (another cell cycle). Similarly, on the AAO microchip seen in **Figure 6.3d**, a single N27 cell is divided into two daughter cells 24 hours later without MS. At this point, MS is applied, and the two daughter cells grow and are divided into six daughter cells after another 24 hours.

6.3.3 MS effects on N27 neural cell growth

(1) MS effects on morphology (area) of N27 cells on glass and AAO substrates

In these experiments, both poly-D-lysine-coated glass and poly-D-lysine-coated AAO substrates are used. Representative images show the area size of the N27 cells, measured by an accessory imaging analysis software from Fluorescence Microscope (*Olympus, Inc.*), are given in **Figure 6.4a**.

First, statistical comparisons are conducted of cell morphology (area) on the glass substrate, AAO-substrate1, and AAO-substrate2, all without the administration of MS. In other words, these comparisons only measure the effect of each substrate's topological surface on cell morphology. After 48 hours of incubation, the area of each single neuron cell is measured, shown in **Figure 6.4b (1)**. The area of the cell on AAO-substrate1 (538.67 μm^2) is smaller than that on AAO-substrate2 (551.36 μm^2). By contrast, the cell area on the glass substrate (582.12 μm^2) is larger

www.manaraa.com

than those on AAO-substrate1 and AAO-substrate2. Detailed statistical analysis can be found in the supplementary document. In short, the N27 cell morphology on both AAO substrates is statistically different from that on the glass substrate. However, there is no statistically significant difference in the N27 cell morphology on AAO-substrate1 in comparison to that on the AAO-substrate2, suggesting that differences in nanopore size and porosity among AAO substrates have no clear effect on cell growth.

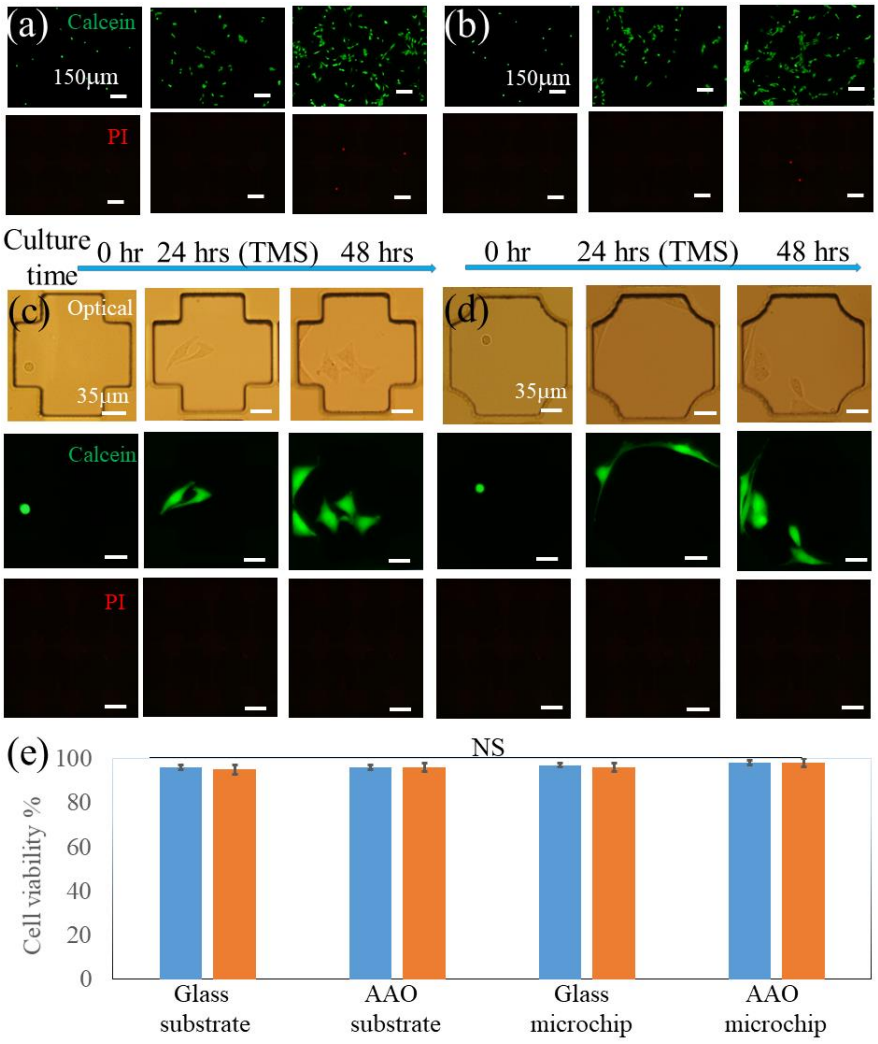

Figure 6.3 *Effect of MS on N27 cell viability. Live/dead assay on N27 cells cultured on (a) coverslip glass, (b) AAO substrate, (c) glass microchip, (d) AAO microchip. Green (calcein AM) and red (propidium iodide: PI) denote live cell and dead cell, respectively. MS is applied at 24 hrs; (e) % viability of N27 cells cultured on four substrates for 24 hrs (blue) and 48 hrs (orange), respectively. NS denotes no statistically significant difference.*

www.manaraa.com

Second, the cell areas on the three substrates (AAO-substrate1, AAO-substrate2, and glass) with and without MS are shown in **Figure 6.4b (2)-(4)**. The area of the cell without MS on AAO-substrate1 (~538.67 μm^2) is larger than that (520.52 μm^2) with MS. Similarly, on AAO-substrate2, the cell area without MS (~551.36 μm^2) is larger than that with MS (537.04 μm^2). In terms of the glass substrates, the cell area without MS (~582.123 μm^2) is also larger than that with MS (~519.153 μm^2). Detailed statistical analysis can be found in the supplementary document. All the results indicate that MS indeed affects cell growth. Specifically, for all three substrates, the area of the cells that received MS is statistically smaller than that of the ones that did not receive MS. It is important to note that MS is applied to the cells after 24 hours of growth, or one cell cycle, and that the measurements are taken 24 hours later.

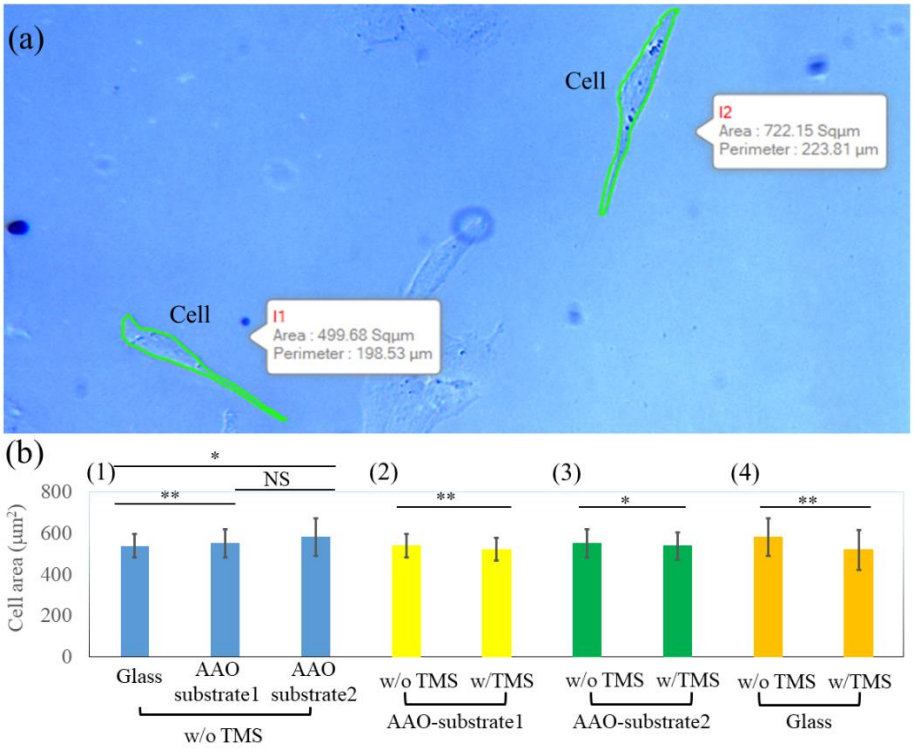

Figure 6.4 *(a) Representative images showing N27 cells grown on a nanoporous AAO substrate; their sizes (areas) are measured by an imaging analysis software; (b) quantification of cell size of N27 cells cultured on three different substrates without or with MS at 24 hrs. Asterisks * and ** denote statistically significant differences with $p < 0.05$ and $p < 0.005$, respectively. NS denotes no statistically significant difference*

www.manaraa.com

(3) Effects of MS on single N27 neural cell on microchip

In order to assess the effect of MS on cells more efficiently, arrayed microholder chips have been used to monitor the division process of single cells subject to MS. First, cell synchronization is needed to ensure the cells are at the same stage of the cell cycle, which can be achieved using the serum deprivation method described in Section II [21, 22]. Second, in order to monitor the cell division process accurately, one single N27 cell is captured in each microholder, enabling its division process to be tracked over the following days. To this end, several steps are required to maximize the capture of the single cell into each microholder: (1) After cells are detached from the bottom of the cell culture flask, they are pipetted into a sterile culture tube (*Corning*) that is put on a vortex mixer *(VX200-Labnet*) with a rotation speed of 500 rpm. This step ensures that the cells are uniformly distributed in the tube and that there are no aggregated cells. (2) The concentration of cells is controlled close to 0.1 million/ml. Based on our experiments, 0.1 million/ml is the optimum cell concentration to maximize the number of microholders on-chip to capture a single cell when the cell solution is delivered to the chip by pipette. (3) The chip is given several gentle rinses with the culture medium (10% fetal bovine serum) to achieve optimum single cell capture.

Accordingly, single cell division in a microholder is monitored by taking optical images at 0 hours, 24 hours, and 48 hours, as shown in **Figure 6.5**. When MS is not administered, a cell typically divides into two daughter cells after one cell cycle (~24 hours) and into four cells after another cell cycle (~48 hours in total). However, when MS is applied at the 24-hour mark, the two cells divide into more than six cells after another cell cycle (~48 hours in total), as shown in **Figure 6.5b**. As a result of MS, two more new daughter cells manifest within the same period of time compared to the chip with cells that do not receive MS (**Figure 6.5a**). Clearly, the microholder chip provides a

www.manaraa.com

straightforward technical platform to conduct an accurate analysis of the effect of MS on cell division.

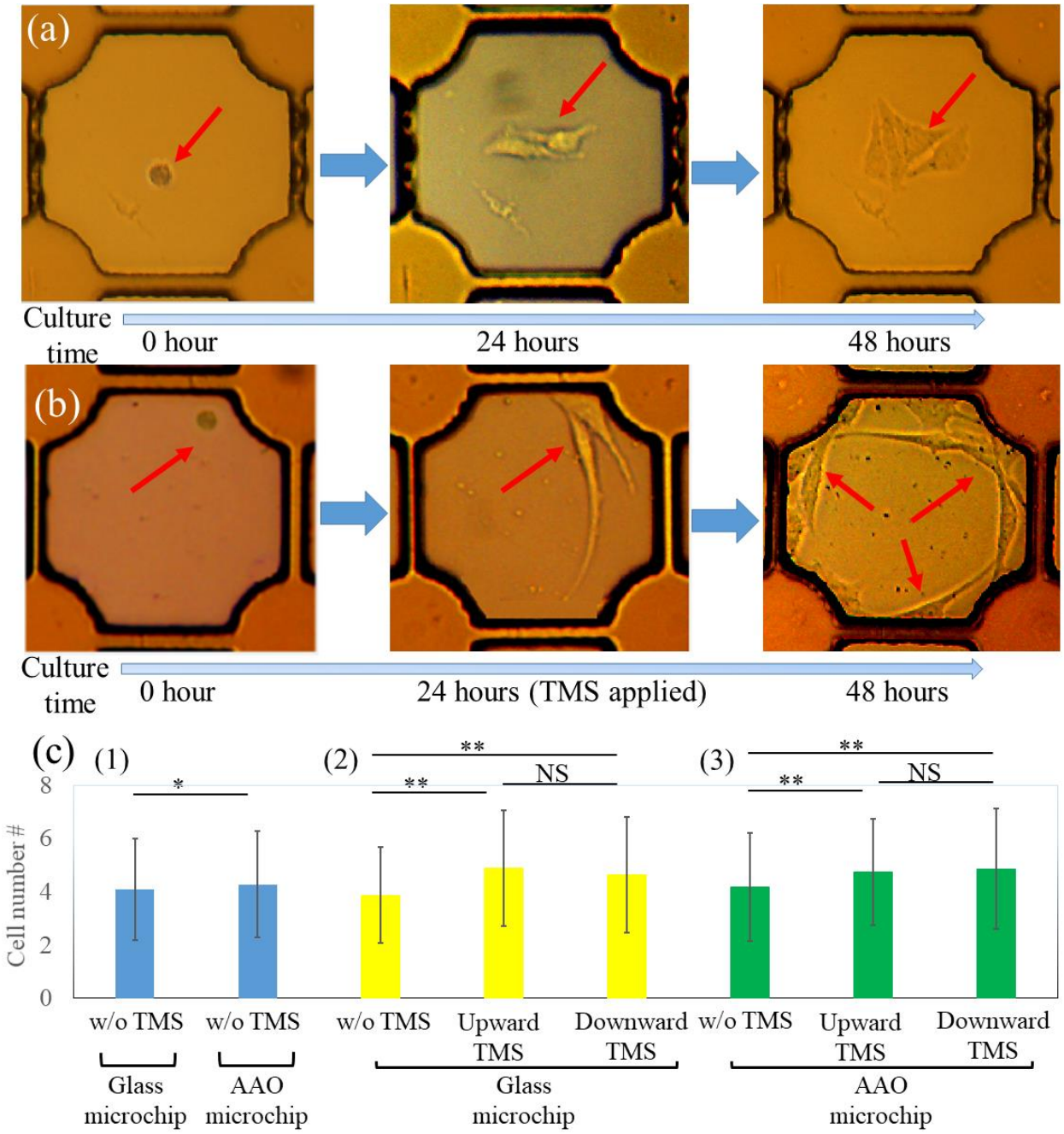

Figure 6.5 *Representative images are showing (a) the division of a single neuron cell in a microholder without MS, (b) the division of a single cell with MS. The cells are indicated with red arrows. (c) Quantification of cell number at 48 hrs in glass microchip and AAO microchip without or with MS at 24 hrs. Asterisks * and ** denote statistically significant differences, with $p < 0.05$ and $p < 0.005$, respectively. NS denotes no statistically significant difference.*

www.manaraa.com

Several trials have been done to study the MS effect. For each trial, three microchips with captured cells are immersed in cell media in three Petri dishes and are stored in an incubator (*NUAIRE-5700*) at all times save for when the MS is applied. Upward MS and downward MS are applied on two microchips, respectively, the third microchip serving as a control without any MS. The experimental details and analysis are summarized in **Table 6.S3** (see supplementary document).

First, statistical comparisons of cell division are conducted on the glass microchip and the AAO microchip without applying MS. Since no MS is applied to these cells, any differences in outcome are due solely to the surface properties of the glass and AAO surfaces. As shown in **Figure 6.5c (1)**, the average number of cells (~4.08) on the glass microchip is smaller than that (~4.28) on the AAO microchip, a statistically significant difference. Detailed statistical analysis can be found in the supplementary document. In short, the nanoporous surface of the AAO microchip affects N27 cell growth, promoting the cell division process in comparison with the flat surface of the glass microchip.

Second, when upward-MS is applied to cells on a glass microchip after 24 hours of growth, as shown in **Figure 6.5c (2)**, the average cell number after a further 24 hours (~4.87) is greater than the cell number of the control group that received no MS (~3.87). Similarly, when downward-MS is administered to cells on a glass microchip, the average cell number at the 48-hour mark (~4.64) is larger than that of the control. Detailed statistical analysis can be found in the supplementary document. Clearly, the average cell number without applying MS is statistically smaller than that with MS. This result indicates that MS can promote cell division. However, no statistical difference has been found between upward-MS and downward-MS, suggesting that the direction of MS has no effect on the cell division process in these contexts.

www.manaraa.com

Third, when MS is applied to cells on an AAO microchip after a 24-hour period of growth, as shown in **Figure 6.5c (3)**, the average cell number at the 48-hour mark is ~4.73 with upward-MS and ~4.85 with downward-MS. By contrast, the average cell number of the control group receiving no MS is ~4.18. These constitute similar results to those observed on the glass microchip. In both cases, the average number of cells is increased when MS is administered after 24 hours (i.e. one cell cycle) of growth, indicating that the proliferation of N27 cells can be expedited by MS. The MS direction does not affect cell division.

Several important elements in the experiments should be noted. First, if the MS is applied immediately after the cells are seeded on the substrates or microchips, the experimental results are not consistent, and the viability of the cells is unstable. Allowing the cells to attach to the substrate and allowing them to grow for one day before applying MS are crucial steps to ensure consistent experimental results. Hence, we only focus on the experiments in which MS is applied to cells after cells have been given one full cycle of growth (24 hours) on the substrate. Second, the effect of MS on cells can be clearly and immediately observed in one cell cycle (i.e. 24 hours); hence we mainly focus on monitoring cells' behaviors during a 24-hour period after administration of MS. Notably, experiments that have monitored cell growth 72 hours and longer after MS have consistently shown increased cell numbers in comparison with control groups.

6.4 Conclusions

This study constitutes the first investigation into the effect of MS on the viability, proliferation, and growth of N27 at the single-cell level on different substrates. N27 cells have been found to have a clear preference for growing on the *bare* nanostructured AAO surface as opposed to the *bare* coverslip glass surface. The nanostructures on the AAO surface allow the N27 cells to attach, spread,

www.manaraa.com

and migrate easily, thereby benefiting their growth. A poly-D-lysine coating on either of these surfaces leads to no discernible difference in the growth of the cells. A live/dead assay has shown negligible cytotoxic effects of MS on cell viability. Additionally, the study has evaluated the effect of MS on the proliferation and growth of single N27 cells by measuring cell sizes and monitoring the cell division process in the microholders on a chip. MS has been found to have a statistically significant effect on both cell morphology and cell division/proliferation. Specifically, MS can expedite the division of N27 cells regardless of the direction in which it is applied. As a result, more N27 cells can be generated with MS than without. These results indicate that MS may help the proliferation and regeneration of neural cells; more largely, the results enhance current understandings of the potential for MS to be used in the treatment of neurological disorders.

6.5 Supplementary information

(1) The fabrication process flow for SU8 microholder chip with AAO nanoporous surface (*AAO microchip*) is described in **Figure 6.S1**. For SU8 microholder chip with glass surface (*glass microchip*), the fabrication process flow is similar to that on **Figure 6.S1(a)**, requiring only from step 4 to step 5 to fabricate SU8 microholders on glass substrate.

(2) The Magstim 2002 monophasic stimulator with '8' shape coil (Magstim D702 double 70 mm) is used to apply MS on cells as shown in **Figure 6.S2a**. The directions of generated magnetic fields are opposite in the two windings and perpendicular to the surface of the '8' shape coil so as perpendicular to the chip holder on both sides. As shown is **Figure 6.S2b**, upward magnetic field (MF) is generated from the left side of the coil, and downward MF is introduced from the right side coil. The power level is set to 100% which is the maximum power level of the stimulator, and the measured MF strength for the '8' shape coil is shown in **Figure 6.S2c**. The

www.manaraa.com

upward peak MF strength is ~1.5MA/m and the downward peak MF is ~1.25 MA/m for the '8' shape coil, respectively.

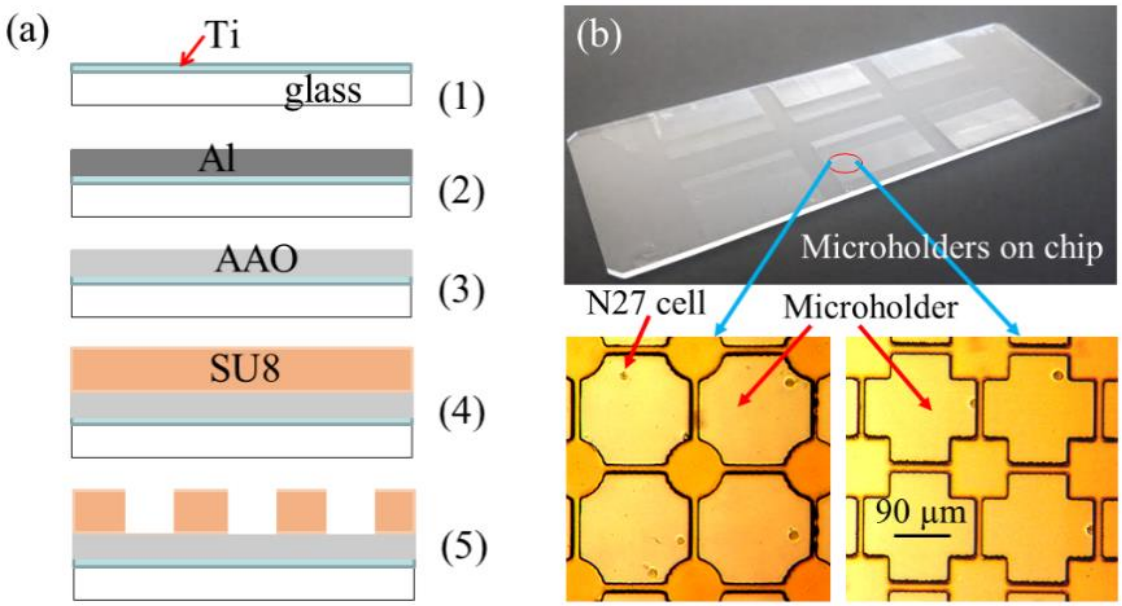

Figure 6.S1 *Arrayed SU8 microholder chip for studying the single N27 cell behaviors. (a) Fabrication process flow for AAO microholder chip. (b) A photo of microholders on-chip and the close-up optical micrographs of arrayed SU8 microholders and the captured single neural cell N27.*

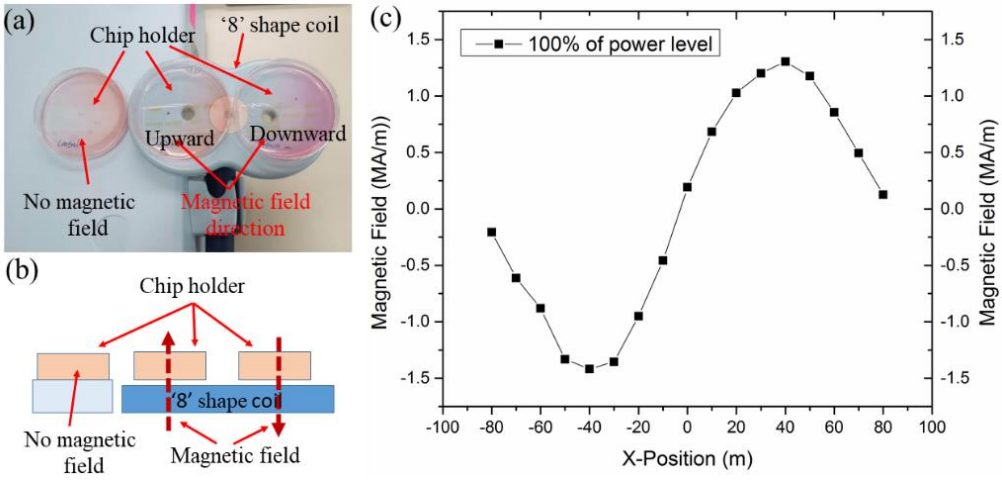

Figure 6.S2 *(a) Experimental setup for applying MS on cells inside microholder chips, the chips are kept in petri dish holders filled with cell media; the magnetic field direction is perpendicular to the chip surface, one is upward, the other is downward. No magnetic field is applied on the chip for the control experiment; (b) Sketch of the cross-section of the experimental setup; (c) The measured magnetic field strength and distribution generated by the MS generator ('8' shape coil).*

www.manaraa.com

(3) The morphometric analysis of N27 cells, experiments of N27 cells on three substrates (AAO-substrate1, AAO-substrate2, and glass substrate) is summarized in **Table 6.S1.**

Table 6.S1 Statistical analyzed results of MS effect on cell morphology on different *substrates.*

Substrate & MS treatment	**Cell numbers**	**Mean cell size (area: μm^2)**	**SD (area: μm^2)**	**SD error (area: μm^2)**	**P-value**
AAO-substrate1 (no MS)	199	538.67	56.25	3.99	0.002
AAO-substrate1 (with MS)	171	520.52	55.48	4.24	
AAO-substrate2 (no MS)	252	551.36	68.94	4.34	0.032
AAO-substrate2 (with MS)	177	537.04	66.41	4.99	
Coverslip glass (no MS)	100	582.12	90.92	9.09	0
Coverslip glass (with MS)	96	519.15	97.26	9.93	

The cell area without MS applied on AAO-substrate1 (n=199, mean=538.67, SD=56.247) is smaller than the one with MS applied (n=171, mean=520.52, SD=55.484). Similarly, on AAO-substrate2, the cell area without MS applied (n=252, mean=551.36, SD=68.944) is smaller than the one with MS applied (n=177, mean=537.04, SD=66.405). For glass substrate, the cell area without MS applied (n=100, mean=582.123, SD=90.922) is also smaller than those with MS applied (n=96, mean=97.261, SD=9.926). The Histogram plot of cell area measured on AAO-substrate1, AAO-substrate2 and glass are shown in **Figure 6.S3**. Test of Normality is conducted to check each group's normality assumption. In **Figure 6.S4**, the normal QQ-plot is generated to test the normality assumption for all the three groups, the shape of each QQ-plot is normally distributed. The outlier assumption is checked by plotting boxplot in **Figure 6.S5**. There is no

www.manaraa.com

outlier for each group so that the assumption is met. Accordingly, one-way ANOVA is suitable to study the statistical difference for all the three groups.

The first one-way ANOVA is conducted to evaluate whether the cell area with MS applied group is statistically different as the one without MS applied on AAO-substrate1. As shown in **Figure 6.S5 (a)**, there are no outliers in the boxplot. The assumption of homogeneity of variances is met as the equality of variance from the Levene statistic test is in a reasonable range ($p=0.609 > 0.05$). As shown in **Table 6.S1**, the cell area without MS apply AAO-substrate1 is statistically different as the one with MS apply (ANOVA $F(1, 368) = 9.68$, $p = 0.002 < 0.05$).

Another ANOVA is conducted to check the statistical difference of cell area between MS applied sample and without MS applied sample on AAO-substrate2. As shown in **Figure 6.S5(b)**, there is no outlier in the boxplot. The assumption of homogeneity is met, as the equality of variance from the Levene statistic test is met ($p=0.201 > 0.05$). From the **Table 6.S1**, the result of cell area without MS apply on two-step AAO is statistically different as the one with MS apply (ANOVA $F(1, 427) = 4.624$, $p =0.032 < 0.05$).

The third one-way ANOVA is conducted to check the statistical difference of cell area between MS applied sample and without MS applied sample on glass substrate. As shown in **Figure 6.S5(c)**, there is no outlier in the boxplot. The assumption of homogeneity is met, as the equality of variance from Levene statistic test is met ($p=0.680 > 0.05$). From the **Table 6.S1**, the result of cell area without MS apply on glass is statistically different as the one with MS apply (ANOVA $F(1, 194) = 21.943$, $p =0.0 < 0.05$).

Next, in order to study the cell morphology (area) on different substrate, a statistical analysis is conducted among AAO-substrate1, AAO-substrate2 and glass substrate. In this case, there is no MS applied on each group which means the study only focus on material property effects. After

www.manaraa.com

48 hours of incubation, the cell area is measured for each single neuron cell. The cell area on AAO-substrate1 (n=199, mean=538.67, SD=56.247) is smaller than the cell area on AAO-substrate2 (n=252, mean=551.36, SD=68.944), and there is a further increase observed from AAO-substrate2 to glass substrate (n=100, mean=582.123, SD=90.922). Test of Normality for each group can be seen from **Figure 6.S4**. The outlier assumption is checked by plotting boxplot in **Figure 6.S5(d)**. There is no outlier for each group so that the assumption is met. Next, the assumption of homogeneity of variances is checked, as the equality of variance from Levene statistic test was not in a reasonable range ($p=0.000 < 0.05$), homogeneity of variances violates the assumption. The Games-Howell's mean difference is appropriate when homogeneity of variance does not meet for multiple group data comparison [28]. As a result, a decrease of 12.692 (95% CI, -26.556 to 1.172) from AAO-substrate1 to AAO-substrate2 is not statistically significant ($p =0.081 > 0.05$); A decrease of 43.459 (95% CI, -66.981 to -19.937) from AAO-substrate1 to glass is statistically significant ($p = 0.000 < 0.05$); a decrease of 30.767 (95% CI, -54.625 to -6.908) from AAO-substrate2 to glass is statistically significant ($p = 0.008 < 0.05$).

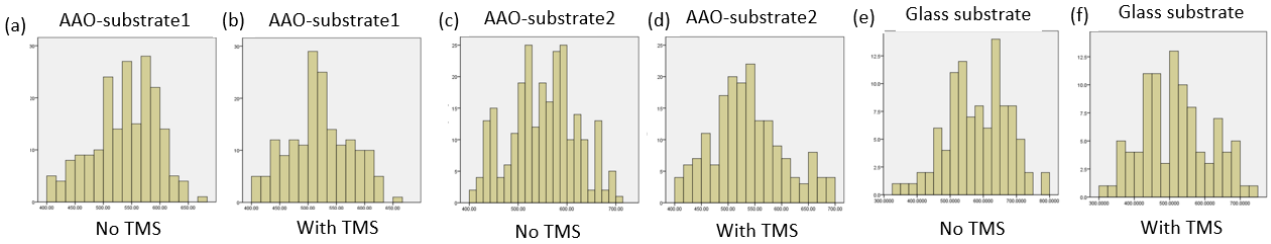

Figure 6.S3 *Histogram plot of cell area measurement on (a,b) AAO-substrate1, (c-d) AAO-substrate2 and (e-f) glass substrate.*

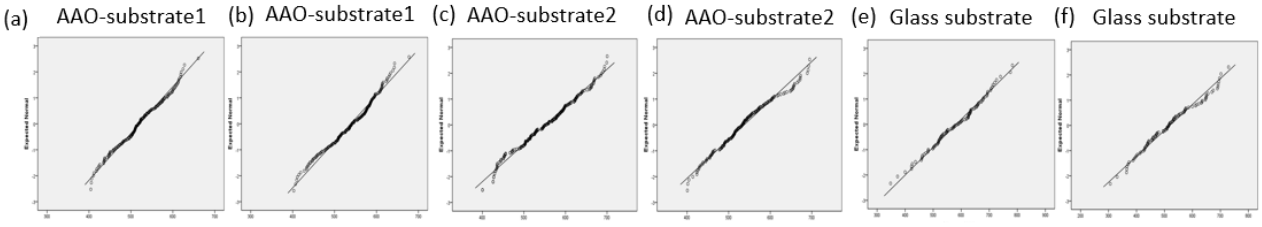

Figure 6.S4 *Normal QQ-plot of cell area measurement on (a,b) AAO-substrate1, (c-d) AAO-substrate2 and (e-f) glass substrate.*

www.manaraa.com

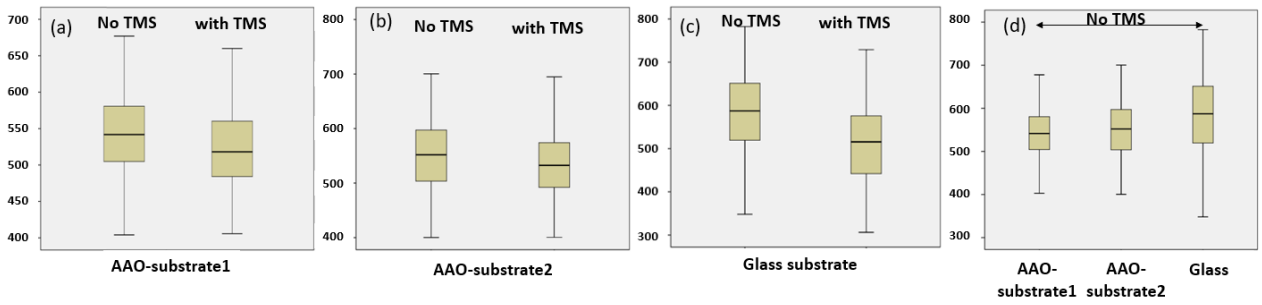

Figure 6.S5 *Boxplot of cell area measurement on (a)AAO-substrate1, (b) AAO-substrate2, (c)glass substrate, and (d)*

(4) For cell division process analysis of N27 cells, experiments on two microchips (glass microchip and AAO microchip) have been performed and summarized in **Table 6.S2**.

Table 6.S2 *Statistical analyzed results of MS effect on cell division in microchip*

Microchip & MS treatment	**Cell numbers**	**Mean cell numbers in *each* microholder after 48 hrs** (only *one* cell in each microholder at 0 hr)	**SD (cell numbers)**	**SD err (cell numbers)**	**P-value**
a). Glass microchip w/o MS	348	3.87	1.79	0.10	(a,b)=0.002 (a,c)=0.000 (b,c)=0.432
b). Glass microchip w/ upward-MS at 24 hrs	285	4.87	2.17	0.13	
c). Glass microchip w/ downward-MS at 24 hrs	247	4.64	2.18	0.14	
e). AAO microchip w/o MS	625	4.18	2.03	0.08	(e,f)=0.000 (e,g)=0.000 (f,g)=0.514
f). AAO microchip w/ upward-MS at 24 hrs	728	4.73	1.99	0.07	
g). AAO microchip w/ downward-MS at 24 hrs	720	4.85	2.26	0.08	

www.manaraa.com

(a) Glass microchip

The averaged cell number measured at 48-hour of the control group (n=348, mean=3.87, SD=1.795) is smaller than the samples with upfield MS applied (n=285, mean=4.87, SD=2.17), and the downfield MS applied group (n=247, mean=4.64, SD=2.18) is higher than the control group but lower than the upfield MS applied group. The Histogram and normal QQ-plot of cell numbers count at 48-hour on glass microholder devices are plotted in **Figure 6.S6**. None of the three groups is normally distributed. Then, the descriptive skewness and kurtosis are checked for each group. For instance, skewness and kurtosis values are 0.678 and 0.399 for control group; 1.134 and 1.258 for up field MS applied group; 0.999 and 1.289 for down field MS applied group. Since all skewness and kurtosis values are fit in an acceptable limit of (-2, +2), one-way ANOVA is considered a robust test against none-normal data with a small skewed or kurtotic distributed shape, statistical significance can be tested by conducting one-way ANOVA test [29,30,31,32]. The outlier assumption is checked by plotting boxplot in **Figure 6.S6**. There are no significant outliers for each group so that the assumption is met. All standard outliers are kept as they all generated from the standard experiments, and those data improve our result to be more accurate and reasonable. The assumption of homogeneity of variances is checked. As the equality of variance from Levene statistic test is not in a reasonable range ($p=0.002 < 0.05$), homogeneity of variances violates the assumption. The Games-Howell's mean difference is appropriate when homogeneity of variance does not match for multiple group data comparison [28]. As a result, a decrease of -1.006 (95% CI, -1.38 to -0.63) from control group to up field MS applied group is statistically significant ($p =0.000 < 0.05$); A decrease of -0.772 (95% CI, -1.17 to -0.37) from control group to down field MS applied group is statistically significant ($p = 0.000 < 0.05$); an increase of 0.234 (95% CI, -0.21to 0.68) from up field MS applied group to down field MS applied

www.manaraa.com

group is not statistically significant (p = 0.432 > 0.05). which means there i no obvious effect of MS direction on cell number.

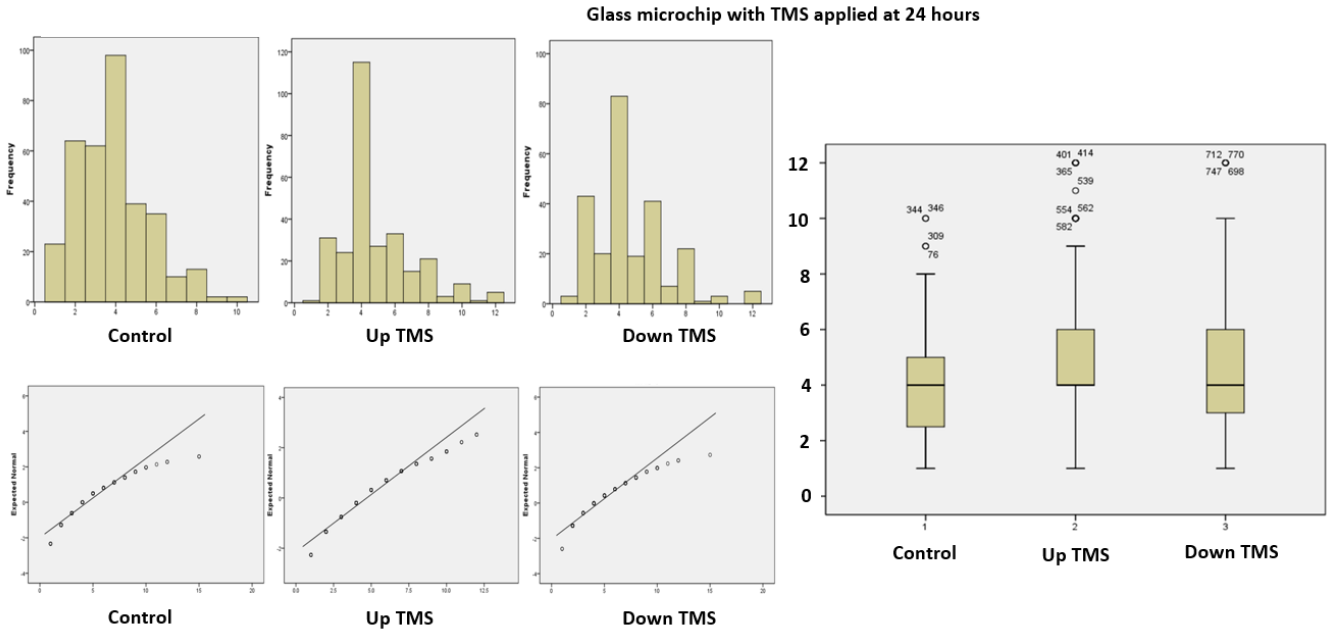

Figure 6.S6 *Histogram, normal QQ plot and boxplot of cell number count at 48 hours on glass microchip device. Up and down field MS were applied at 24 hours, and a MS free group was set as a control group.*

(b) AAO microchip

The averaged cell number measured at 48-hour of the control group (n=625, mean=4.18, SD=2.028) is smaller than the samples with upfield MS applied (n=728, mean=4.73, SD=1.997), and a further increase on downfield MS applied group (n=720, mean=4.85, SD=2.259). The Histogram and normal QQ-plot of cell numbers count at 48-hour on AAO microholder devices are plotted in **Figure 6.S7**. None of the three groups are normally distributed. Next, the descriptive skewness and kurtosis are checked for each group. For instance, skewness and kurtosis values are 0.739 and 0.256 for control group; 0.659 and 0.348 for up field MS applied group; 0.979 and 1.058 for down field MS applied group. Hence, one-way ANOVA is an appropriate method to study the statistical significant for all groups since each group's skewness and kurtosis are fit in an acceptable limit of -2 to 2. The outlier assumption is checked by plotting boxplot in **Figure 6.S7**.

www.manaraa.com

There are no significant outliers for each group so that the assumption is met. The assumption of homogeneity of variances is checked. As the equality of variance from Levene statistic test is not in a reasonable range ($p=0.008 < 0.05$), homogeneity of variances violated the assumption. The Games-Howell's mean difference is appropriate when homogeneity of variance does not match for multiple group data comparison [28]. A decrease of -0.552 (95% CI, -0.81 to -0.29) from control group to up field MS applied group is statistically significant ($p =0.000 < 0.05$); A decrease of -0.675 (95% CI, -0.95 to -0.40) from control group to down field MS applied group is statistically significant ($p = 0.000 < 0.05$); A decrease of 0.123 (95% CI, -0.39 to 0.14) from up field MS applied group to down field MS applied group is not statistically significant ($p = 0.514 > 0.05$).

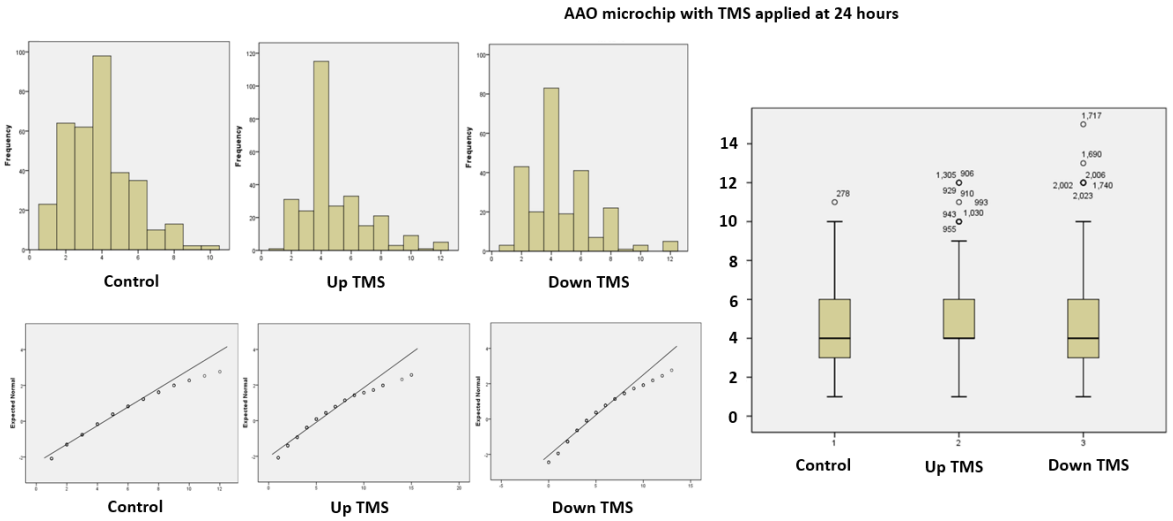

Figure 6.S7 *Histogram, normal QQ plot and boxplot of cell number count at 48 hours on AAO microchip device. Up and down field MS were applied at 24 hours, and a MS free group was set as a control group.*

In order to study the cell division (number) on different substrate, a statistical analysis is conducted between glass microholder group and AAO microholder group. In this case, there is no MS applied on each group which means the study only focus on material property effects. The cell number on glass microholder (n=650, mean=4.08, SD=1.901) is smaller than the cell number on

www.manaraa.com

AAO microholder (n=974, mean=4.28, SD=1.995). The Histogram and normal QQ plot are shown in **Figure 6.S8**. The assumptions of normality are violated for both groups. Next, skewness and kurtosis values are checked for each group. The values are (0.802, 0.501) for glass microholder group and (0.693, 0.342) for AAO microholder group. One-way ANOVA is still a robust method to check the significant difference among the three groups because the skewness and kurtosis values of each group was in an acceptable limit of (-2, +2). The outlier assumption is checked by plotting boxplot in **Figure 6.S8**. There are no extreme outliers for each group so that the assumption matched. Next, the assumption of homogeneity of variances is checked. As the equality of variance from Levene statistic test is not in a reasonable range ($p=0.032 < 0.05$), homogeneity of variances violates the assumption. The Welch's F is appropriate when homogeneity of variance is not met for comparison between two groups [33-35]. The result of Welch's F test shows the cell numbers account at 48-hour on glass microholder and AAO mircroholder are statistically significant ($p = 0.040 < 0.05$). Namely, the cell number after 48 hours grow on glass microholder (mean mean=4.08, SD=1.901) is significantly smaller than the cell number grow on AAO microholder (mean=4.28, SD=1.995).

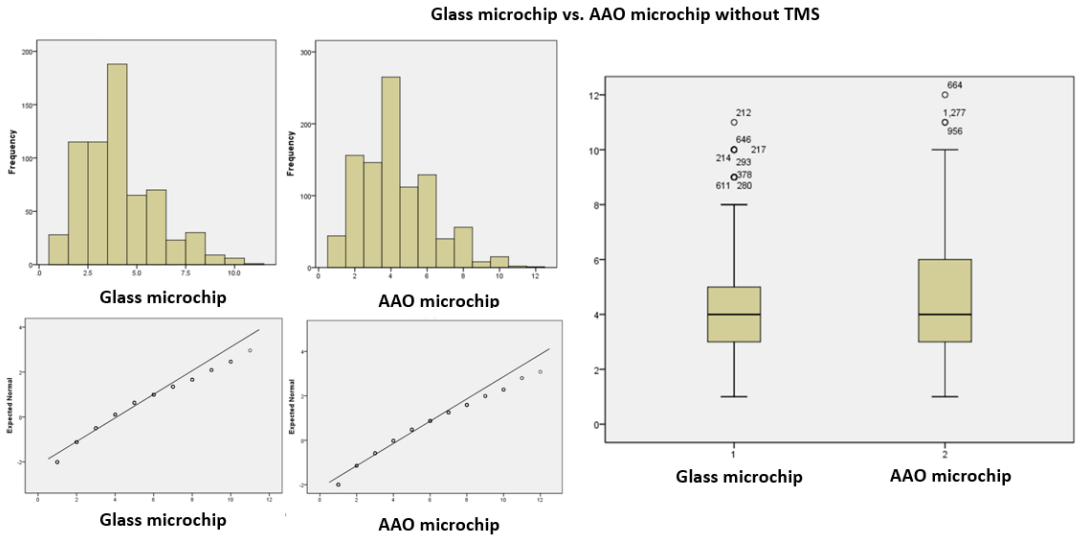

Figure 6.S8 *Histogram, normal QQ plot and boxplot of cell number count at 48 hours on Glass and AAO microchip device without MS.*

www.manaraa.com

References

[1] O'Reardon, J.P., et al., Efficacy and safety of transcranial magnetic stimulation in the acute treatment of major depression: a multisite randomized controlled trial. Biological psychiatry, 2007. 62(11): pp. 1208-1216.

[2] Fregni, F., et al., Repetitive transcranial magnetic stimulation is as effective as fluoxetine in the treatment of depression in patients with Parkinson's disease. Journal of Neurology, Neurosurgery & Psychiatry, 2004. 75(8): pp. 1171-1174.

[3] Seidlits, S., Lee, J. and Schmidt, C. (2008). Nanostructured scaffolds for neural applications. Nanomedicine, 3(2), pp.183-199.

[4] Ranella, A., et al., Tuning cell adhesion by controlling the roughness and wettability of 3D micro/nano silicon structures. Acta biomaterialia, 2010. 6(7): pp. 2711-2720.

[5] Bucaro, M.A., et al., Fine-tuning the degree of stem cell polarization and alignment on ordered arrays of high-aspect-ratio nanopillars. ACS nano, 2012. 6(7): pp. 6222-6230.

[6] Zhu, W., et al., 3D nano/microfabrication techniques and nanobiomaterials for neural tissue regeneration. Nanomedicine, 2014. 9(6): pp. 859-875.

[7] Tran, P.A., L. Zhang, and T.J. Webster, Carbon nanofibers and carbon nanotubes in regenerative medicine. Advanced drug delivery reviews, 2009. 61(12): pp. 1097-1114.

[8] Yang, K., et al., Nanotopographical manipulation of focal adhesion formation for enhanced differentiation of human neural stem cells. ACS applied materials & interfaces, 2013. 5(21): pp. 10529-10540.

[9] Nel, A.E., et al., Understanding biophysicochemical interactions at the nano–bio interface. Nature materials, 2009. 8(7): pp. 543-557.

[10] Baca, H.K., et al., Cell-directed assembly of lipid-silica nanostructures providing extended cell viability. Science, 2006. 313(5785): pp. 337-341.

[11] Katz, E. and I. Willner, Biomolecule-Functionalized Carbon Nanotubes: Applications in Nanobioelectronics. ChemPhysChem, 2004. 5(8): pp. 1084-1104.

[12] Alava, T., et al., Control of the graphene–protein interface is required to preserve adsorbed protein function. Analytical chemistry, 2013. 85(5): pp. 2754-2759.

[13] Majd, S., et al., Applications of biological pores in nanomedicine, sensing, and nanoelectronics. Current Opinion in Biotechnology, 2010. 21(4): pp. 439-476.

[14] Movileanu, L., Interrogating single proteins through nanopores: challenges and opportunities. Trends in Biotechnology, 2009. 27(6): pp. 333-341.

www.manaraa.com

[15] Gu, L.-Q. and J.W. Shim, Single molecule sensing by nanopores and nanopore devices. Analyst, 2010. 135(3): pp. 441-451.

[16] He, Y., X. Li, and L. Que, A transparent nanostructured optical biosensor. Journal of biomedical nanotechnology, 2014. 10(5): pp. 767-774.

[17] Jani, A.M.M., D. Losic, and N.H. Voelcker, Nanoporous anodic aluminium oxide: advances in surface engineering and emerging applications. Progress in Materials Science, 2013. 58(5): pp. 636-704.

[18] Li, X., Y. He, and L. Que, Fluorescence detection and imaging of biomolecules using the micropatterned nanostructured aluminum oxide. Langmuir, 2013. 29(7): pp. 2439-2445.

[19] Brüggemann, D. (2013). Nanoporous Aluminium Oxide Membranes as Cell Interfaces. Journal of Nanomaterials, 2013, pp.1-18.

[20] Che, X., et al., A molecular beacon biosensor based on the nanostructured aluminum oxide surface. Biosensors and Bioelectronics, 2015. 72: pp. 255-260.

[21] Davis, P.K., A. Ho, and S.F. Dowdy, Biological methods for cell-cycle synchronization of mammalian cells. Biotechniques, 2001. 30(6): pp. 1322-1331.

[22] Foster, D.A., et al., Regulation of G1 cell cycle progression: distinguishing the restriction point from a nutrient-sensing cell growth checkpoint (s). Genes & cancer, 2010. 1(11): pp. 1124-1131.

[23] Coakes, S.J. and L. Steed, SPSS: Analysis Without Anguish Using Spss Version 14.0 for Windows. 2009: John Wiley \& Sons, Inc. 282.

[24] Hou, Y., et al., Collagen attachment to the substrate controls cell clustering through migration. Physical biology, 2014. 11(5): pp. 056007.

[25] Gentile, F., et al., Differential cell adhesion on mesoporous silicon substrates. ACS applied materials & interfaces, 2012. 4(6): pp. 2903-2911.

[26] Pathak, P., et al., Real-time monitoring of cell viability using direct electrical measurement with a patch-clamp microchip. Biomedical microdevices, 2011. 13(5): pp. 949-953.

[27] Kim, Y.H., et al., Enhancement of neuronal cell adhesion by covalent binding of poly-d-lysine. Journal of neuroscience methods, 2011. 202(1): pp. 38-44.

[28] Games, P., Keselman, H. and Clinch, J. (1979). Tests for homogeneity of variance in factorial designs. Psychological Bulletin, 86(5), pp.978-984.

[29] Trochim, W. M., & Donnelly, J. P. (2006). The research methods knowledge base (3rd ed.). Cincinnati, OH:Atomic Dog.

www.manaraa.com

[30] Gravetter, F., & Wallnau, L. (2014). Essentials of statistics for the behavioral sciences (8th ed.). Belmont, CA: Wadsworth.

[31] Field, A. (2000). Discovering statistics using spss for windows. London-Thousand Oaks- New Delhi: Sage publications.

[32] Field, A. (2009). Discovering statistics using SPSS. London: SAGE.

[33] Brown, M. and Forsythe, A. (1974). The Small Sample Behavior of Some Statistics Which Test the Equality of Several Means. Technometrics, 16(1), p.129.

[34] Field, A. (2009). Discovering statistics using SPSS. Sage publications.

[35] Tomarken, A. and Serlin, R. (1986). Comparison of ANOVA alternatives under variance heterogeneity and specific noncentrality structures. Psychological Bulletin, 99(1), pp.90-99.

www.manaraa.com

CHAPTER 7. CONCLUSIONS AND FUTURE WORK

7.1 Conclusions

In this dissertation, the mechanism and characteristics of AAO thin film-enabled fluorescence enhancement have been studied. Based on AAO fluorescence enhancement, two kinds of optical biosensors have been developed. AAO has also been used as a nanostructure substrate to study the MS effect on single neuron cell. All these studies make AAO as a great potential material which can be practically used in biosensing, bio-detection, and biocompatible platform for studying cell behavior.

First, for the mechanism of AAO fluorescence enhancement, it has been found that fluorescence enhancement is probably mainly attributed by the Al NPs embedded in the AAO thin film. Both E-field calculation from an FEA based simulation and experimental results of <111> Al existed in half anodized AAO have further supported this hypothesis. The characteristics of fluorescence enhancement enabled by AAO thin film have also been studied.

We found AAO fluorescence enhancement is gap-dependent, and it also different in excitation wavelengths. Blue light excitation (475 nm) for FSS is larger than that of green light excitation (550 nm) for PI.

Second, a new class of molecular beacon biosensors based on the nanostructured aluminum oxide or anodic aluminum oxide (AAO) surface is developed. We have demonstrated that fluorophore-tagged hairpin DNA attached to AAO surface can function as highly sensitive and selective sensors for detecting oligonucleotides. Specifically, for a hairpin DNA sequence (H1 DNA), the binding with a complementary DNA sequence (T1 DNA) results in the decrease in fluorescent signals close to 80%. In contrast, for the nonspecific sequence (T2 DNA), the average change in fluorescent signals is only about 6%. Currently, the limit of detection limit (LOD) of the

www.manaraa.com

DNA sensors is about 10 nM. Due to the simplicity and cost-effectiveness for fabricating hundreds and thousands of arrayed AAO micropatterns on a single chip, this microarray format platform offers great potential for highly multiplexed and sensitive biodetection for the diagnosis of various diseases.

Third, the detection of the transforming growth factor TGF-β1 secreted by pancreatic stellate cells (iTAF) in buffer and conditioned medium using a nano-AAO thin film sensor has been demonstrated. Purified TGF-β1 in buffer has been detected successfully, and our current limit of detection is as low as 10 ng/ml in buffer solution. Using this sensor, TGF-β1 in culture media secreted by ITAF cells only and by iTAF cells in co-culture with capan-1 cells has been detected, respectively. The concentration of TGF-β1 in the conditioned medium from culturing iTAF cells only for 48 hrs is found to be ~17.6 ng/ml, and from co-culturing iTAF cells and capan-1 cells is found to be ~321.2 ng/ml.

Finally, we have investigated the effect of MS on N27 cell viability, proliferation, and growth at the single-cell level. Glass and nanopore structured AAO have been used as the substrates for cell growth. It has been found that N27 cells prefer to grow on the bare AAO surface than the bare glass surface. For both substrates, MS showed negligible cytotoxic effects on cell viability. Furthermore, MS has been found to have a statistically significant effect on both cell morphology and cell division/proliferation. MS can expedite the division of N27 cells regardless of the direction in which it is applied. These results indicate that MS may help the proliferation and regeneration of neural cells; more largely, the results enhance current understandings of the potential for MS to be used in the treatment of neurological disorders.

www.manaraa.com

7.2 Future work

The AAO fluorescence enhancement mechanism has been studied and two biosensors have been developed based on the AAO fluorescence enhancement effect. AAO also demonstrated good biocompatibility for N27 cell growth, and cell proliferation on AAO is also better than on glass under the same condition of applied MS. However, there are still some recommendations for further improvements and applications which I would like to mention in the following paragraphs.

Micropatterned AAO based molecular beacon biosensors: our current limit of detection (LOD) is 10 nM. However, it can be further improved by changing the dimension of AAO. Based on our study in Chapter.3, AAO pore size, porosity, film thickness present effects on the final fluorescence enhance factor. Although it is not the main reason for hundreds or even thousands of the enhance factor, it can still improve the DOT maybe 10 times. In the following works, more data need to be collected by using different dimensions of AAO micropatterns. It can help to finalize a best dimension which can help to improve the LOD of this biosensor.

Micropatterned AAO based growth factor biosensor: We have successfully developed this sensor for testing purified TGF-β1, and TGF-β1 in co-cultured medium. However, it is still hard to monitor the TGF-β1 secretion in real time. It may due to several reasons. First, cell cultured in micropatterned AAO chip did not grow very well with high concentration of 1 million cells/mL which is the same concentration as the co-culture cell cultured in standard cell culture flask. The cell health condition limited the TGF-β1 secretion rate. In order to keep secreted TGF-β1 concentration as high as possible in AAO microchip, we did not change or add fresh medium within 48 hours. Also, we kept the microchip as a closed system to prevent evaporation problem. All these operations may be the reason for secreted TGF-β1 concentration was much lower than it cultured in traditional cell culture flask. Additionally, there are some other concerns which may

www.manaraa.com

lead to the unsuccessfully real-time detection. For example, trypsin is a chemical used to detach spread cells from the substrate. It may damage the sandwich bonding during the cell release process. When cell released from the surface, the release force may also break down the bond of TGF-β1, or TGF-β1 can be removed away by the released cells. It is because the TGF-β1 is bonded by molecular affinity which is a relatively low force rather than has a chemical bond force. Because of this, the amount of TGF-β1 in AAO microchip after 48 hours incubation was too low to be detected. To overcome these problems, a new design of device is required. A schematic plot of possible design is shown in **Figure 7.1**. In this design, ITAF and Capain-1 cells are co-cultured in region-1 where is the area of glass functioned with collagen for improving cell adhesion and growth. AAO micropatterns are fabricated at region-2 where is also the sensing region. A biofilter is set inside the chip between region-1 and region-2. PDMS is bonded on this chip to make it as a closed system while input-1, input-2 and one output are made on this PDMS. After cell are seeded on the region-1, the inlet-1 can be used to flow fresh medium and also drive a fluidic force from region-1 to region-2. Cautions are required when flow fresh medium. The flow rate of needs to be controlled in a very slow speed because we want to keep secreted TGF-β1 stay long enough to ensure its bonding with the functioned AAO micropattern before it is rinsed away. The whole device can be incubated in a standard incubator for 48/72/96 hours or even longer, then taking the corresponding fluorescence images. During the incubation, input-2 is opened to get air exchange between the inside system and surrounding atmosphere in the incubator. After incubation, the microchip will be taken out and final two chemicals can be added through input-2 on region-2. Then after dry, the device is ready for fluorescence intensity measurement. This design can overcome many issues we had, such as air exchange problem, the possibility of trypsin damage and nutrition problem.

www.manaraa.com

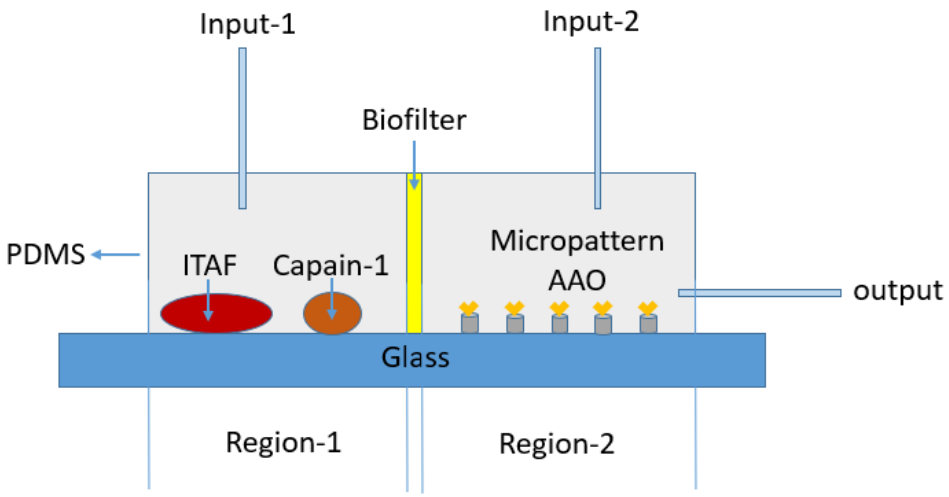

Figure 7.1 *Schematic of proposed design*

MS effect on single neuron cells (N27) project: we have discovered MS can improve N27 cell proliferation, and time to apply MS is an important factor. However, we have not understood the reason behind those results. In the future, more biological experiments need to be conducted to get the information during cell growth when those cells treated under MS. For example, some types of proteins or enzymes may increase after MS treatment. With the increased amount of these proteins or enzymes, cell speed up its proliferation process. Fluorescence labeling technique can be used to reveal if there are some types of proteins or enzymes are stimulated under MS. Based on the previous study, AAO can be used as a test sensor for this work since it has also demonstrated noticeable biocompatibility for N27.

www.manaraa.com